

An investigation into the interaction between waves and ice

Jean Rabault

July 31, 2018

Thesis submitted for the degree of Philosophiæ Doctor

Contents

Preface	1
Acknowledgments	3
1 Introduction	5
1.1 Polar regions: key areas under rapid evolution	5
1.2 Sea ice and waves: a brief overview of the literature	7
1.2.1 Fieldwork and experiments of wave-ice interaction	9
1.2.2 Theoretical understanding	11
1.3 Main axis of the PhD work	17
1.3.1 Fieldwork investigation of waves in ice	17
1.3.2 Laboratory investigation of the interaction between sea ice and waves	20
1.4 Unsuccessful directions, future work and a few personal thoughts .	24
1.5 Conclusion	27
1.6 Appendix: some technical aspects: an overview of the open source tools released in the course of the project	28
 Bibliography	29
2 Selected publications	37
2.1 Publication 1: Observations of wave dispersion and attenuation in landfast ice	40
2.2 Publication 2: Measurements of wave damping by a grease ice slick in Svalbard using off-the-shelf sensors and open-source elec- tronics	55

2.3	Publication 3: A Method to Estimate Reflection and Directional Spread Using Rotary Spectra from Accelerometers on Large Ice Floes	66
2.4	Publication 4: Field observations and preliminary investigations of a wave event in solid drift ice in the Barents Sea	80
2.5	Publication 5: PTV investigation of the mean drift currents under water waves	93
2.6	Publication 6: The attenuation of monochromatic surface waves due to the presence of an inextensible cover	102
2.7	Work 7: Experiments on wave propagation in grease ice: combined wave gauges and PIV measurements	112

Preface

This thesis is submitted in the partial fulfillment of the requirements for the degree of Doctor of Philosophy at the University of Oslo. It represents work that has been carried out between 2015 and 2018, under the supervision of Pr. Atle Jensen, Dr. Graig Sutherland, and Dr. Kai H. Christensen, in collaboration with Pr. Aleksey Marchenko and Pr. Brian Ward. The work presented was carried at the University of Oslo and the University Center in Svalbard. Financial support for the work was provided by the Norwegian Research Council under the Petromaks 2 scheme, through the project WOICE (Experiments on Waves in Oil and Ice), NFR Grant number 233901.

The thesis consists of an introduction, and a selection of 7 publications. The introduction presents the scientific context in which the work was undertaken, the methodology used, the results obtained, as well as some personal thoughts about unsuccessful directions encountered during the project and possible future work. I certify that this dissertation is mine and that the results presented are the result of the work of our research group, to which I brought significant contribution.

Oslo, March 2018

Jean Rabault

Acknowledgements

I want to express my deepest gratitude towards my PhD advisors, Pr. Atle Jensen, Dr. Graig Sutherland, and Dr. Kai H. Christensen. Their help and guidance have been critical to the work accomplished. In addition, I have received precious help from a number of people in the course of the project. Pr. Aleksey Marchenko has been a key player for this project both during fieldwork and laboratory experiments on Svalbard. The participation of Pr. Brian Ward was critical for collection of the data obtained during the first field measurements. Finally, MSc. Trygve Halsne has paved the way for several of the laboratory experiments performed at the University of Oslo through his Master Thesis. Moreover, none of this work would have been possible without the help of our Laboratory Engineer, MSc. Olav Gundersen, whose help, technical competence, and good spirit is key to all the successes achieved throughout this project. In the same spirit, I want to express special thanks to Dr. Jostein Kolaas, who is at the origin of much of the software and scripts used when performing PIV. I also want to thank Terje Kvernes and Lucy Karpen, for their kind help, and interesting discussions covering a broad range of computer network, hardware, and other computer science related topics.

Finally, I want to thank all the people I have met either during or alongside work in the last 4 years, who have made my life in Norway a nice moment, as well as my family for their continuous support.

Chapter 1

Introduction

1.1 Polar regions: key areas under rapid evolution

Sea ice is a major feature of the polar environments, both in the Arctic and Antarctic. Sea ice extent reaches an annual maximum of about 14 million square kilometers in the Arctic, and 18 million square kilometers in the Antarctic (see Fig. 1.1). In average throughout the year, sea ice covers a total of 25 millions square kilometers, which is about 7 % of the world's oceans surface (Parkinson, 1997; Council et al., 2007). Sea ice is both a central element of the polar ecosystems and a key to the global climate and ocean circulation.

In the last couple of decades, significant decline in the Arctic sea ice extent has been observed (Feltham, 2015). While accurately predicting the pace at which sea ice decline will occur remains challenging (Overland and Wang, 2013), the reduction of sea ice extent in the Arctic cannot be denied. Predicting the evolution of sea ice extent is made challenging by the number of contributing feedback mechanisms, and the complex physics involved. Some feedback mechanisms involved in sea ice decline have been well known for a long time, such as the Albedo difference between open sea and sea ice: while ocean surface without sea ice reflects about 6 to 7 % of the incoming solar energy flux, sea ice covered by new snow can reflect as much as 85 % of the incoming energy (Shao and Ke, 2015). Other feedback mechanisms have been discovered more recently, and may also play an important role in particular in the Arctic. One such mechanism is the consequence of ice breaking by surface gravity waves. It has been shown from satellite data that reduced sea-ice extent, by increasing the fetch available for wave development, has lead to higher wave activity and wave amplitude in the Arctic basin, which in turn increases ice breakup and melting (Thomson and Rogers, 2014; Kohout

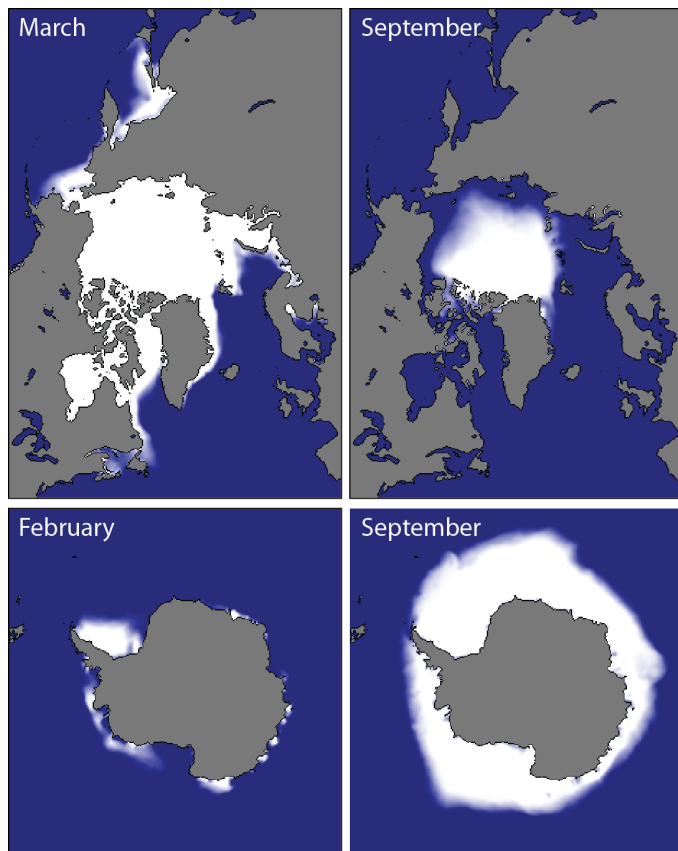


Figure 1.1: Average Arctic and Antarctic sea ice extent from the period 1981-2010 based on microwave satellite data, at the approximate seasonal maximum and minimum levels for each of the polar regions. Reproduced from information released by the National Snow and Ice Data Center (NSIDC), University of Colorado, Boulder.

et al., 2014).

While sea ice is important for the global climate, it is also critical to human activities in the polar regions. Changes in the climate alongside technological developments are creating new opportunities for human activities in the Arctic, including sustainable development of resource-based industries, fishing, tourism, and faster shipping routes between Europe and Asia. Improved scientific understanding of the Arctic environment, especially sea ice dynamics that are largely influenced by the incoming wave field, are necessary to help produce increased value in polar regions, while doing so in a safer and more environmental-friendly way (Christensen and Broström, 2008; Pfirman et al., 1995; Rigor and Colony, 1997).

Therefore, there is motivation to develop a better understanding of sea ice and its interaction with waves, both for improving our understanding of the global climate system, protecting the local ecosystems, and enabling larger scale human activities in the polar regions.

1.2 Sea ice and waves: a brief overview of the literature

The study of sea ice is made complex by the great variety of ice conditions that are observed in nature. Ice comes in a great variety of shapes, thicknesses and mechanical properties, from grease ice (behaving similarly to a floating layer of highly viscous fluid) to land-fast ice (behaving as a thin elastic plate), through pack ice, large floes, and icebergs (Squire et al., 1995; Newyear and Martin, 1997; Squire, 2007; Christensen and Broström, 2008; Sutherland and Rabault, 2016). This is illustrated by images taken throughout the course of the project (Fig. 1.2). Each kind of ice exhibits different physical properties, including density, mechanical resistance, brittleness, Young modulus, and the amount of trapped air, salt and brine. The combination of these different types of ice is important for the existence of a large Arctic ice pack. For example, grease ice and broken ice floes present in the Marginal Ice Zone (MIZ, the first ice infested area encountered from the open ocean) play an important role in damping high frequency waves, that would otherwise lead to fast breaking of the inner, continuous sea ice.

The following sections present a brief overview of the current understanding of wave-ice interaction that is available through both experimental data and theoretical analysis published in the literature.

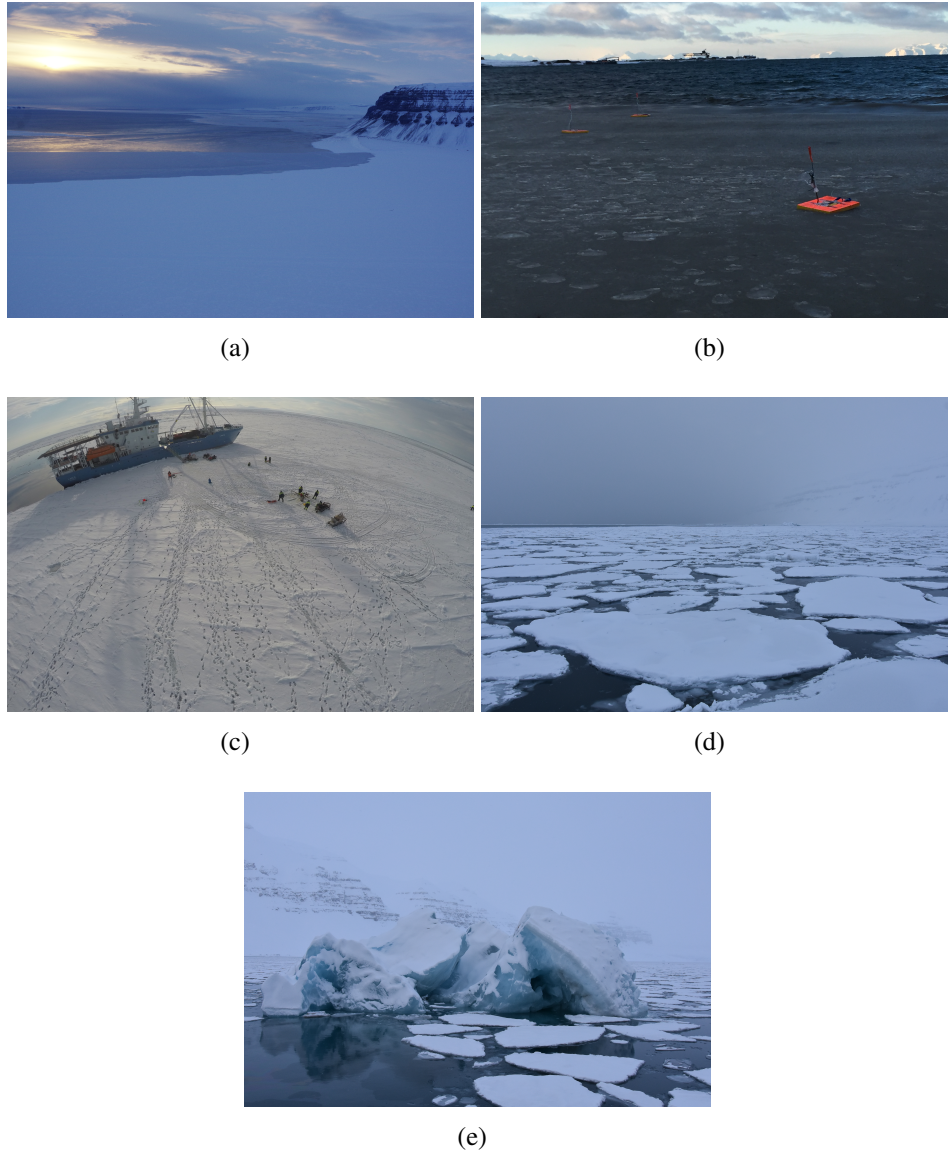


Figure 1.2: Illustration of the diversity of ice conditions encountered during the course of the WOICE project. Credits: WOICE members (Atle Jensen and Jean Rabault, UiO; Aleksey Marchenko, UNIS; Graig Sutherland, MET), and Sebastian Sikora (UNIS logistics). (a): landfast ice and newly formed ice fringes (Tempelfjorden, 2015), (b): grease ice slick close to the shore (Adventfjorden, 2016), (c): large ice floe in the Barents sea (East of Svalbard, 2016), (d): broken floes (Tempelfjorden, 2017), (e): iceberg released from glacier calving (Tempelfjorden, 2017). Each of those forms of ice have different physical properties that influence wave propagation and damping, in addition to providing a variety of opportunities for the local species, as well as challenges for human activities.

1.2.1 Fieldwork and experiments of wave-ice interaction

Despite a long tradition of studying waves in ice (Greenhill, 1886; Ewing and Crary, 1934), field measurements are still relatively sparse when considering the large area and diversity of the polar regions. This can in part be explained by the dangerous conditions in which waves in ice should be measured, challenges in the deployment of sensors, and the costs associated with the development of instruments that can work in the polar conditions (Squire, 2007).

When considering wave-ice interaction, a number of quantities should ideally be measured. The most important of these include the wave dispersion relation, wave spectrum, wave directional spectrum (which, by contrast to wave spectrum, contains not only information about the energy content at each frequency, but also information about the direction of propagation and angular spread), ice quality and thickness, wave damping, and water eddy viscosity. Measuring the wave dispersion relation is important from a theoretical perspective, and has also been suggested as a way to indirectly estimate the ice quality and thickness (Marsan et al., 2012). Indeed, ice thickness influences the dispersion relation (Greenhill, 1886) and one can, therefore, obtain an estimation of the ice thickness from measurements of wave propagation. Similarly, the wave spectrum contains important information about the incoming wave energy, and measurements at different locations can be used to compute the wave damping as a function of frequency. This, in turn, provides important information for the calibration of wave in ice models. Finally, measuring the wave directional spectrum allows for the gathering of additional information about wave propagation. In particular, it has been suggested that the wave directional spectrum can be a way of discriminating which mechanism is dominating the wave attenuation, either non-conservative dissipation or conservative directional redistribution (Ardhuin et al., 2016).

In the literature, two main categories of methods are presented for performing measurements of the propagation of waves in ice. The first category relies on instruments that need to be physically present at the location of measurement, either on or under the ice. These instruments can rely on a variety of sensors such as seismometers (Marsan et al., 2012), pressure sensors (Marchenko et al., 2013), shear probes (McPhee and Martinson, 1994), accelerometers, Inertial Motion Units (IMUs) (Kohout et al., 2015; Meylan et al., 2014), Acoustic Doppler velocimeters (ADVs), and Acoustic Doppler current profiler (ADCPs) (Hayes et al., 2005). Such sensors allow a direct measurement of the ice or water motion, and the data must be stored locally and retrieved physically at the location of

the instrument. Alternatively, it may be sent through Iridium or another satellite communication means owing to the remoteness of the polar regions. Using such instruments makes it relatively easy to compute simple quantities such as wave spectrum, wave damping and the water eddy viscosity (McPhee and Martinson, 1994; Meylan et al., 2014; Doble et al., 2015). In addition, one can retrieve the wave number and, therefore, the dispersion relation from a correlation analysis between adjacent instruments (Fox and Haskell, 2001), even though such measurements remain sparse (Squire, 2007).

By contrast, another category of measurements relies on instruments that do not need to be physically present on the ice, in particular Synthetic Aperture Radars (SARs, Liu et al. (1991); Shen et al. (2018)) and lasers (LIDAR, Wadhams (1975); Sutherland and Gascard (2016)). These methods have been deployed from both planes and satellites, and offer several advantages, the most obvious one being that they do not require physical access to the ice, which can be both difficult and dangerous. SAR images obtained from satellites such as the two Sentinel 1 are especially convenient, as these follow a polar orbit. As a consequence, the polar regions are very well covered and large datasets are freely available. After processing, SAR images allow the computation of important quantities such as the quality of the ice cover (Dierking, 2013), or the wave 2D spatial spectrum (Shen et al., 2018). However, some limitations are also present when using SAR satellite images. In particular, usually SAR images do not include time resolved information, making it challenging to retrieve the frequency data necessary for the computation of the dispersion relation (Shen et al., 2018).

In parallel to field measurements, laboratory experiments have been performed at least since the early 1980s. These include both small scale measurements in wave tanks typically a few meters long and half a meter deep kept in a cold room (Martin and Kauffman, 1981; Newyear and Martin, 1997), and measurements in large scale environmental wave flumes (Wang and Shen, 2010a; Zhao and Shen, 2015). Most commonly, the waves are measured using pressure sensors located on the wall of the tank (Newyear and Martin, 1997; Wang and Shen, 2010a), a few tens of centimeters under the surface of the water. This presents some challenges, as pressure is a quantity that can be difficult to measure accurately (since the pressure variations due to waves can often be small compared to the mean pressure value at a given measurement depth), and the pressure disturbance created by the waves is exponentially attenuated with depth. In addition, performing measurements on the side wall of the wavetank may induce some systematic bias if the wave field is 3D. All those inconveniences can be avoided using ultrasonic

gauges, but these have not been commonly used in the past. Measurements of wave elevation can be used to obtain the wave damping, as well as the wavelength (and, therefore, dispersion relation). Wavelength is obtained through a correlation analysis granted that several measurements are performed within a distance of typically one half wave length. Therefore, by performing measurements for a series of monochromatic waves of varying frequency, one can explore all aspects of wave propagation in the laboratory.

Unfortunately, while wave propagation has been investigated in several wave-tank experiments, very little data have been collected regarding the motion of the water, such as mean currents and eddy viscosity. This is the consequence of the higher cost, complexity, and operational challenges implied by instruments that can perform such measurements. To the knowledge of the author, only the study of Martin and Kauffman (1981) has discussed such aspects, qualitatively and based on visual observations.

1.2.2 Theoretical understanding

One of the aims of experimental data is to provide a basis for the development and calibration of models describing the propagation of waves in ice. The ability to understand and model both wave damping and wavelength is important for a number of practical applications. For example, predictions of the wave-field in the polar regions, which is critical for safety of operations in the arctic, weather forecasts, and sea ice forecasts, requires an estimate of the spatial damping of waves (Christensen and Broström, 2008).

When studying the propagation of waves in ice infested regions, one usually considers a single 2D harmonic wave mode having a frequency $f = \omega/(2\pi)$, wave number $k = 2\pi/\lambda$, and surface elevation $\eta(x, t) = a \cos(kx - \omega t)$, where a is the wave amplitude, t the time and x the direction of wave propagation. Owing to the superposition principle, any wave state can be reconstructed from a combination of such harmonic modes, at least as far as linear effects are the dominant mechanism so that different wave modes do not interfere with each other and can be considered individually.

The first theoretical description of wave propagation in ice-covered sea was presented by Greenhill (1886), and describes the propagation of waves under a continuous, solid ice cover behaving as a thin elastic plate. Such description of wave propagation under a continuous solid ice cover has proven successful and was further refined by a number of authors (Squire, 1993; Wadhams, 1973; Liu

and Mollo-Christensen, 1988; Squire et al., 1995), to include for example the effect of compression stress of the ice cover. The main idea of the model consists in conducting the classical derivation for water waves relying on the potential flow theory, while changing the boundary condition at the water surface to take into account the elastic effect of the ice. This model describes the effect of the ice on the dispersion relation, but does not consider energy dissipation and damping. Stream function models can also be used to describe the propagation of waves in ice, but are generally encountered for models that aim at describing wave damping. Considering a 2D monochromatic wave traveling in the positive x direction, with the vertical direction z pointing upwards, $z = 0$ being the mean water surface (covered by ice), $z = -H$ the water bottom, one gets the following system of equations in the frame of potential flow theory:

- Equations for velocity components:

$$u_x = \frac{\partial \phi}{\partial x}, \quad u_z = \frac{\partial \phi}{\partial z} \quad (1.1)$$

- 2D continuity equation in the water occupied volume:

$$\frac{\partial^2 \phi}{\partial x^2} + \frac{\partial^2 \phi}{\partial z^2} = 0 \quad (1.2)$$

- Free slip boundary condition at the water bottom, $z = -H$, in the case of potential flow:

$$\frac{\partial \phi}{\partial z} = 0 \quad (1.3)$$

- Kinematic equation for the water / ice interface, $z = \eta(x, t)$:

$$\frac{\partial \eta}{\partial t} + \mathbf{u} \cdot \nabla \eta = \frac{\partial \phi}{\partial z} \quad (1.4)$$

- Pressure balance at the water / ice interface, $z = \eta(x, t)$:

$$-\rho_w \left(\frac{\partial \phi}{\partial t} + g\eta \right) = \left(\frac{Eh^3}{12(1-\nu^2)} \frac{\partial^4}{\partial x^4} + hP \frac{\partial^2}{\partial x^2} + h\rho_i \frac{\partial^2}{\partial t^2} \right) \eta(x, t) \quad (1.5)$$

where $\mathbf{u}(x, z) = (u_x(x, z), u_z(x, z))$ is the 2D wave velocity field, $\phi(x, z)$ the associated velocity potential, g the acceleration of gravity, ρ_i the volumetric mass

density of the ice, ρ_w the volumetric mass density of the water, h the thickness of the elastic ice cover, E its elastic modulus, ν its Poisson coefficient, and P the compression stress. The left hand side of Eqn. (1.5) is the pressure in the water as described from the Bernoulli equation, while its right hand side comes from the application of thin plate theory to the elastic ice cover.

Linearizing Eqns. (1.4) and (1.5) around the state of rest, and keeping only first order terms, results in a system of equations that can be solved in a way similar to the usual linear water waves. The dispersion relation obtained is then of the form:

$$\omega^2 = \frac{gk + Bk^5 - Qk^3}{\coth(kH) + kM}, \quad (1.6)$$

where the following reduced parameters were used:

$$B = \frac{Eh^3}{12\rho_w(1-\nu^2)}, \quad Q = \frac{Ph}{\rho_w}, \quad M = \frac{\rho_i h}{\rho_w}. \quad (1.7)$$

The dispersion relation Eqn. (1.6) and the phase and group velocities, $c_p = \omega/k$ and $c_g = \partial\omega/\partial k$, can then be obtained numerically. The predictions for wavelength compares well with data from solid, continuous ice cover, even if relatively few such studies are available in the literature (Squire, 1984).

A few observations can be made using Eqns. (1.6, 1.7). First, in the case without ice cover ($B = Q = M = 0$), the usual water waves dispersion relation is obtained: $\omega^2 = gk \tanh(kh)$. In the case that there are no compression and flexural effects (for example, because many cracks are present in the ice cover), the simpler mass loading model is recovered. One should note that the ice thickness has a very drastic effect on the dispersion relation, as $B \propto h^3$, and flexural rigidity appears in the dispersion relation through a term in the form Bk^5 .

While theory is relatively successful at describing wave propagation under a continuous ice cover, the problems of describing wave attenuation in all types of ice and wave propagation in complex ice conditions are more arduous. In the case of a continuous solid ice cover, attenuation can take place either in the ice itself, due to inelastic deformation of the ice cover, brine migration, creep, plasticity, and other complex mechanisms (Collins III et al., 2016; Marchenko and Lishman, 2017; Wang and Shen, 2010b), or in the water under the ice due to the effect of viscosity on the shear generated by the no-slip boundary condition at the ice interface (Lamb, 1932; Weber, 1987). The first category of phenomena, i.e. dissipation in the continuous ice itself, is difficult to describe and predict in details

as the properties of the ice are very dependent on a number of parameters such as ice age, brine content, and temperature. The second category of phenomena is also challenging to predict due to the influence of parameters such as the roughness of the interface between the water and the ice sheet, and the influence of the eddy viscosity level in the water on dissipation (De Carolis and Desiderio, 2002). The situation is even more complicated when complex ice such as ridged inhomogeneous pack ice, pancake ice or broken ice floes are present: in this case, the geometry and spatial variability of the ice add complexity to the formulation of the problem and new phenomena, such as wave diffraction and reflection, become important.

When studying wave damping by sea ice due to viscous effects, one generally considers that the wave amplitude is exponentially damped across the direction of propagation:

$$\frac{\partial a}{\partial x} = -\alpha a, \quad (1.8)$$

where x the distance into the ice-covered region, a the wave amplitude, and α the spatial decay coefficient that describes wave attenuation. It should be noted that one can easily convert between spatial and temporal damping using the relation from Gaster (1962):

$$\frac{\beta}{\alpha} = c_g, \quad (1.9)$$

where β is the temporal attenuation rate, and c_g the group velocity. In the following, I will prefer to refer to spatial damping coefficients.

The first theoretical model describing wave attenuation by grease ice is the one by Weber (1987). In this model, the ice is considered so viscous that it does not allow appreciable shear, and the balance between friction and pressure results in a “creeping motion” of the ice. This imposes a no-slip boundary condition under the ice, and all the dissipation occurs in the underlying water. This is similar to the solution found by Lamb (1932) (Equation 304.xiii), and the resulting damping can be written as:

$$\alpha = \frac{1}{2} \nu \gamma k / c_g, \quad (1.10)$$

where ν is the effective viscosity, and $\gamma = \sqrt{\omega/2\nu}$ is the inverse boundary layer thickness.

An effective eddy viscosity much higher than the molecular viscosity of water is required in the water layer for the model to be consistent with observations and laboratory experiments. While a crude simplification of reality, this simple model provides good agreement with both laboratory and field data when an empirical fit value for the effective viscosity of the water is used (Newyear and Martin, 1997; Rabault et al., 2017). The use of a high effective viscosity is usually justified by the need to describe the existence of a large range of eddies under the ice that enhance mixing (De Carolis and Desiderio, 2002; Doble et al., 2015), but in addition it could include some of the effects of the highly viscous grease ice layer that may not be described correctly by the model.

Next, Newyear and Martin (1997) introduced another one-layer model to compare with experimental results in grease ice in a small wave tank facility. By contrast with the model of Weber (1987), the model of Newyear and Martin (1997) assumes that, since most of the wave motion is usually concentrated near the free surface, most of the wave motion takes place into the grease ice and, therefore, attenuation can be calculated considering an infinitely deep grease ice layer. This solution is similar to the calculation of Lamb (1932) for waves propagating in a viscous fluid (Equation 301.9), which can be expressed as:

$$\alpha_{ns} = 2\nu k^2 / c_g, \quad (1.11)$$

where there also ν is taken as a fitting parameter, which this time models grease ice viscous properties.

This second model was later adapted into a two layer model by Keller (1998), who considered the case of finite depth with inviscid water under the ice layer. This opened the way for the development of a variety of such two-layer models. De Carolis and Desiderio (2002) formulated a model in which viscosity is also added to the water under the ice, while Wang and Shen (2010b) considered a model in which the water layer is inviscid, but the ice layer follows a viscoelastic model (Voigt model). Such models are a better description of reality, as a clear separation between grease ice and water is observed in the experiments, and these two phases have vastly different properties. Better agreement is also observed between these models and laboratory data than with the previously mentioned one layer models (Newyear and Martin, 1999), even though the estimation of model quality has often been based on curve fitting and visual impression rather than quantitative metrics (see, for a discussion of this issue, Rabault et al. (2017)). These models predict attenuation as the solution of complex equations. Therefore,

the wave length and attenuation predicted by two layer models cannot be written using simple functions.

Despite their mathematical sophistication, two layer models are affected by at least two issues. First, while being a better description of reality, the parameters they rely on are in practice obtained from fit to experimental data rather than analysis of the underlying properties of the ice, and as a consequence they differ little from the single layer models on this aspect. Therefore, it is difficult to know whether the better agreement observed with experimental data is due to a better description of the physics, or if it is a mathematical artifact due to more fitting parameters being available. In addition, some of the most recent models (Keller, 1998; Wang and Shen, 2010a) have several issues that were raised by Mosig et al. (2015). In particular, the large number of roots in the dispersion relation of the later model makes it challenging to use, as the selection of the physically relevant propagation mode is made much more challenging than in the case of simpler models. While it was recently proven that the dominant mode can easily be identified in most situations (Zhao et al., 2017), more work is needed to clarify the situation in the mode swap zone, where both flexural-gravity and the pressure wave have similar wave numbers. As a consequence of these difficulties and the inherent complexity of implementation of two layer models, I have focused my efforts towards comparison of experimental data with one layer models, while making the data available to authors who may wish to compare them with the more sophisticated two layer models.

Finally, another effect of wave-ice interaction that can be expected on the field and in experiments is the creation of mean currents under the ice. Such currents can have an influence on important mechanisms such as pollutants and nutrients distribution. A major reason for induced currents under sea ice could arise from diffusion of the vorticity generated in the water-ice boundary layer due to the no-slip boundary condition. This can also be seen as a consequence of wave damping and conservation of momentum (Martin and Kauffman, 1981): as waves carry with themselves a wave momentum flux $M = E/c_p$, where $E \propto a^2$ is the mean wave-energy density, reduction in the wave amplitude implies a reduction of the wave momentum flux. Conservation of momentum then induces a current in the water under the ice, and / or forward stress in the ice cover. A viscous, second order, weakly non linear derivation of the induced currents under a thin cover with longitudinal elasticity is presented in Christensen (2005). While the derivation was initially intended to describe the flow under a thin surfactant film, the equations present some similarities with what would be obtained due to a thin elastic

cover with negligible rigidity and predicts the existence of modified currents (relatively to the Stokes drift observed in the free water cases) under surface covers. However, wave momentum flux diminution is not the only effect that plays a role in the development of currents under the ice. In particular, in the case of grease ice, Martin and Kauffman (1981) observed a mean current in the opposite direction to what would be expect from wave momentum flux considerations. This current was found to be a side-effect of mass conservation, when the grease ice layer gets pushed alongside the wave tank by the incoming waves.

1.3 Main axis of the PhD work

The initial objectives of the present PhD thesis were to further investigate wave propagation and damping in sea ice through a comparison of field and laboratory results, and to study associated induced currents that could participate in the dispersion of pollutants in the Arctic regions.

Regarding the first two objectives, the need for further investigation of wave propagation and damping is made clear by the absence of consensus in the literature regarding which wave damping model to use (Mosig et al., 2015). Indeed, the debates taking place can partly be explained by the limited amount of wave data available, relatively to the wide range of ice conditions that can be encountered. More field and laboratory data are necessary to both calibrate models, and offer an exhaustive overview of the effect of different sea ice conditions on wave propagation. Therefore, a large part of our effort has been to perform new measurements, and to participate in the development of instruments and methodology for performing accurate field and laboratory measurements of waves in ice.

Finally, the presence of wave-induced currents under the ice is a topic that, as pointed out in the literature review, has been little investigated in the past. Regarding this last point, I focused on performing measurements using Particle Image Velocimetry (PIV) and Particle Tracking Velocimetry (PTV) in several cases representative of different ice conditions.

More details about both the field and laboratory work performed are available in the next sections.

1.3.1 Fieldwork investigation of waves in ice

Fieldwork investigations performed in this project have focused on measuring wave-ice interaction in the region around Longyearbyen, Svalbard during the win-

ters 2015, 2016, and 2017 (Rabault et al., 2016b; Sutherland and Rabault, 2016; Rabault et al., 2017), and in the Barents sea during the spring 2016 (Marchenko et al., 2017). Various types of ice were observed during those measurements, including land-fast ice, grease ice, large ice floes and broken ice floes. As indicated in the previous sections, there is a critical need for more field measurements to be performed at a reduced price, in order to quantify the sea ice dynamics happening in the Arctic.

The first difficulty when performing measurements in the arctic is set by the harsh environmental conditions in which instruments must operate (Chang and Bonnet, 2010). As a consequence, commercial solutions are expensive and the cost implied by the deployment of a large number of commercial instruments would have been a challenge for the project. Therefore, instruments built in-house based on Inertial Motion Units (IMUs) were developed for performing measurements of waves in ice. Those developments started with the use of Moxa industrial computers during the first measurement campaign, before shifting to (more adapted) microcontroller-based loggers. While the number of instruments built was limited, and, therefore, the hardware is the result of handcrafting and prototyping rather than a commercial product, I took the decision to release all code and designs as open source material. This presents several advantages. In particular, sharing all the details of the design of an instrument can make it easier to reproduce experiments, by drastically reducing the cost and time necessary to build an exact copy of the instrument initially used. In addition, this makes it easier for different groups to build upon a common platform, therefore, encouraging modularity and reuse of previous designs rather than fragmented in-house development, which very likely is redundant between research groups and private suppliers, leading to unnecessary costs. Finally, resorting to open source instruments gives access to the details of their internal functioning, therefore, allowing better transparency over how data is collected and pre-processed compared with many commercial solutions.

The data obtained from the IMU instruments can be used in several ways. The most common uses for the data, which are presented in our publications (Sutherland and Rabault, 2016; Rabault et al., 2017; Sutherland et al., 2017b), include computing the wave energy spectrum (and, from it, other important quantities such as the significant wave height, peak wave frequency, and other spectral characteristics), and estimating the wavelength and dispersion relation.

Once the power spectrum density of acceleration data $S[\eta_{tt}]$ has been computed, usually by means of the Welch method to reduce the noise level, one must

convert it to obtain the power spectrum density $S[\eta]$ of wave elevation, following Tucker and Pitt (2001):

$$S[\eta] = \omega^{-4} S[\eta_{tt}]. \quad (1.12)$$

The wave spectrum S gives information about the wave energy content at different frequencies. It can be used in a variety of ways, including most interestingly for waves in ice to compute the wave damping if several measurements are performed at different points in space. Considering $\alpha(f)$ the frequency dependent spatial damping coefficient, $a_{i/j}(f) = \sqrt{S_i(f)/S_j(f)}$ the attenuation coefficient for waves propagating from sensor j to sensor i , and $d_{i,j}$ the distance along wave propagation direction between those sensors, the damping can be obtained as:

$$\alpha(f) = -\frac{\log(a_{i/j}(f))}{d_{i,j}}. \quad (1.13)$$

Wavelength can also be obtained from comparing the phase shift between sensors separated by a known distance along the direction of wave propagation. Indeed, the phase difference between sensors i and j can be expressed both from the definition of the wave number:

$$\phi_{i,j}(f) = k(f)d_{i,j}, \quad (1.14)$$

as well as from the co-spectral density $S_{i,j}(f)$ between sensors i and j :

$$\phi_{i,j}(f) = \tan^{-1} \left(\frac{Im[S_{i,j}(f)]}{Re[S_{i,j}(f)]} \right), \quad (1.15)$$

where Im and Re indicate the real and imaginary part, respectively. To get best results, the distance between the sensors used for performing a cross correlation analysis should be typically half a wavelength. For distances larger than a wavelength, signal aliasing complicates the processing.

I pushed this approach further in Marchenko et al. (2017) and computed both the dispersion relation and the peak direction of the waves, by using a triad of sensors in a triangle configuration. Each pair of sensors in the triad is used to compute the component of the wave vector along the corresponding direction, so that using three non aligned sensors the full wave vector can be reconstructed from elementary trigonometry.

Following the experience gained from a series of measurement campaigns, I now believe that the configuration used in Marchenko et al. (2017) is the most

promising for performing detailed wave measurements in the field using IMU instruments. In this experiment, a series of 3 triads of IMU instruments (plus one individual instrument, as 10 were available) were positioned over a direction roughly aligned with the direction of wave propagation observed during deployment. As a consequence, both the wave vector (and, hence, dispersion relation) and damping can be obtained in theory. Unfortunately in this experiment, the distance between the sensors (limited by the size of the ice floe they were all deployed on, for logistics reasons) was too little in relation with the wave damping to estimate α with significant error bars. Nonetheless, I hope to be able to deploy again instruments in such a configuration over a larger distance in landfast ice in the future.

Finally, attempts have been made to measure currents in the field using an Acoustic Doppler Velocimeter (ADV) and an Acoustic Doppler Current Profiler (ADCP). No usable data has been generated yet, but it is planned to perform further deployments in the years to come.

1.3.2 Laboratory investigation of the interaction between sea ice and waves

As the goal of this wave in ice study is to describe phenomena happening at larger scales in the nature, field measurements are the final truth against which one should aim to compare models and theory. However, performing experiments in the laboratory presents several advantages compared with field studies:

- Laboratory experiments can be performed in a standardized fashion, therefore, allowing a higher reproducibility of results over what can be achieved in the necessarily complex situations encountered in nature. This is especially true in the case of wave / ice interactions, where for example the ice properties and water eddy viscosity have been shown to drastically vary from one measurement to another (De Carolis and Desiderio, 2002; Timco and Weeks, 2010).
- Laboratory experiments give us control (to some extent) over which physical phenomena are dominant in a given experiment, and which ones can be neglected. For example, concerns have been raised in the case of field measurements of wave attenuation in the marginal ice zone over how much the wind input to the wave spectrum can influence results (Li et al., 2017). This is naturally easily avoided in the laboratory.

- Laboratory experiments are much better adapted than the ocean for applying some of the most informative - but also most challenging to deploy - measurement techniques, such as Particle Image Velocimetry (PIV). This allows to obtain information about the underlying physics that could not have been obtained in the field.

Therefore, this project has relied on a combination of field and laboratory experiments, in which the phenomena observed in field experiments were reproduced in the laboratory for further investigation. For this, three facilities were used:

1. An intermediate size wave tank at the University of Oslo. The wave tank is 24.5 m long, 0.5 m wide, and can be filled with up to 0.7 m of water (Sutherland et al., 2017a). It is equipped with an hydraulics-controlled piston type paddle. The water cannot be frozen and, therefore, no real ice can be used. As a consequence, the ice was modeled using either a thin latex sheet (thickness: 0.25 or 0.5 mm), or a plastic cover (PEHD, thicknesses: 1, 3 and 4 mm). This wave tank is well equipped, with both ULS ultrasonic gauges (resolution 0.18 mm), a white LED lightsheet, and a Falcon 2 camera that can be used to record PIV images. This facility was used for the work presented in the following papers: Sutherland et al. (2017a); Rabault et al. (2016a).
2. The second facility is a small scale wave tank (3.5×0.3 m, filled with up to 0.25 m of water), located in a cold laboratory in Longyearbyen, Svalbard. A piston paddle was built for that tank, and an open source control system was designed (for more information, see the Appendix A). Both Banner ultrasonic gauges (model S18U, resolution 0.5 mm) and the same PIV setup as in Oslo were used in the cold room. As the tank is entirely made of Plexiglas, easy optical access to the water and the side of the ice are available. When growing ice, isolation foam is put around the tank to make sure that ice grows from the surface down into the water. This tank was used for the work presented in Rabault et al. (2018).
3. The last facility is the ice wave tank of HSVA, located in Hamburg, Germany. This is a large climate controlled wave tank, of dimensions 78×10 m, which can be filled with up to 2.5 m of water. As optical access is not possible, PIV could not be used. Instruments provided by the university of Oslo

during those experiments include a set of Banner ultrasonic gauges, an ADV and an ADCP. As measurements at HSVA were performed towards the end of the project, analysis of the data is still under work.

All measurements in the laboratory presented later in the Thesis were performed using monochromatic waves. In addition, a few measurements resorting to a JONSWAP spectrum were performed at the university of Oslo, but analysis of the results proved challenging. As previously stated, three kinds of measurements were performed, depending on the facility used: measurements of wave elevation using ultrasonic gauges, measurements of the water motion using PIV / PTV, and measurements of the water column velocity profile using ADCPs (ADCPs were only used in the last set of experiments in Hamburg).

Ultrasonic gauges provide high frequency measurements (up to 200 Hz) of the wave elevation. Calibration is performed either automatically by the gauges (ULS gauges), or manually by both setting the gauges range and measuring the water height in a set of reference cases (Banner gauges). The information obtained from ultrasonic gauges can be used in a very similar way to the IMU data obtained in the field. In particular, the Fourier spectrum of the wave elevation signal, $S(f)$, can be used to obtain the wave amplitude a by integrating around the harmonic frequency:

$$a(x) = \sqrt{\int_{f_0-\Delta f}^{f_0+\Delta f} S(f, x) df}, \quad (1.16)$$

where f_0 is the harmonic frequency, Δf the half frequency integration width, and x the distance along the wave-tank. A fit of the wave attenuation can be performed on the amplitude data obtained, in a similar way to what is performed with field data.

Information about the wavelength and, therefore, the dispersion relation, can also be obtained from ultrasonic gauges. By setting up gauges in such a way that two of them are separated by typically half a wavelength, one can suppress aliasing effects and obtain a measurement of the wavelength by either a correlation or a cross-spectrum analysis, in a similar way to what is presented in Eqn. (1.15).

One of the advantages of laboratory measurements is to allow (depending on the construction of the wave tank) easy optical access to the water and, therefore, one can perform direct optical measurements of the water velocity field. Compared with instruments such as ADCPs and ADVs, optical measurements have the advantage of being non intrusive and more accurate. Optical measurements

performed in this project relied on a simple mono-camera setup. The light source used was a white light LED array, which is easier and safer to deploy than PIV lasers. A Falcon 2 4M camera was used to acquire images at a frequency of 75 frames per second.

The optical images recorded were used in two ways. In the case of the experiments performed at the University of Oslo under latex or PEHD covers, the damping is very small and boundary layers are too thin to be visible. Therefore, there is little deviation to see in the instantaneous velocity field, and the work performed focused on studying the steady currents under the surface cover. As a consequence, Particle Tracking Velocimetry (PTV) was used, as it can follow the particle drift without introducing the errors that would be obtained from integrating PIV velocity fields. Obtaining unambiguous results about mean currents under waves is difficult, as a number of second order effects happen simultaneously and cannot be studied separately. These effects include the elasticity induced effect that was the main object of interest and the Stokes drift, but also recirculation in the tank, effects of the start of the wave train, and possibly large convection motions due to temperature differences in the room. Despite these difficulties, it was possible to observe an effect of the surface cover (Rabault et al., 2016a) that is in agreement with the predictions of Christensen (2005).

By contrast, the damping was much higher in the experiments performed under grease ice in the wavetank in Svalbard, and rich dynamics could be observed in the water when blocks of grease ice collided. As a consequence, PIV was used in this case. In order to extract information from all the PIV snapshots into a few reduced modes, the Proper Orthogonal Decomposition (POD) relying on the snapshot method was used. The POD is computed from the Singular Value Decomposition (SVD) of the snapshot matrix (for detailed explanations about POD and the snapshot method, see for example Berkooz et al. (1993); Kerschen et al. (2005)). The snapshot matrix, X , is constructed as:

$$X = \begin{bmatrix} u_1^1 & \dots & u_n^1 \\ \vdots & \dots & \vdots \\ u_1^k & \dots & u_n^k \end{bmatrix}, \quad (1.17)$$

where $u_i^j = u(\mathbf{x}_j, t_i)$, with \mathbf{x}_j the position of the point considered, and t_i the time of the snapshot. Both the X and Y components of velocity are stored in u , by letting the $u_i^{1..k/2}$ represent the X component and the $u_i^{k/2+1..k}$ represent the Y component, respectively. As a consequence, each column of X contains the 2D,

2-components velocity field at a given time reshaped into a 1D vector. The SVD decomposition is then computed as:

$$X = USV^*, \quad (1.18)$$

where U and V are unitary matrices. The diagonal coefficients of S^2 give the energy of each mode, while U and V contain the POD modes and POD mode coefficients. The POD modes together with the POD mode coefficients contain the full information about the velocity field at all times. In particular, the description of the velocity field obtained with POD is interesting as it optimizes the energy content in the modes of lower index, therefore, effectively extracting an ordered list of the most energetic coherent structures in the flow.

The results obtained from POD allow for a direct confirmation of the exponential attenuation of the waves under the ice. In addition, a recirculation current similar to the one observed qualitatively by Martin and Kauffman (1981), is detected. Finally, in the case of colliding grease ice packs, eddy structures are detected. This provides a possible mechanism for the injection of eddy motion in the field.

1.4 Unsuccessful directions, future work and a few personal thoughts

While one usually only reports positive results in the published literature, I find that this Thesis may be the place to also talk about unsuccessful directions and problems encountered in the project.

No real unsuccessful attempts were encountered in the field, but a number of difficulties inherent to working with sea ice restricted the amount of data collected. In particular, the winters 2016 and 2017 were too mild to encounter ice conditions similar to the landfast ice found in 2015, which was the ideal case for studying large continuous ice sheets (Sutherland and Rabault, 2016). Looking back with the experience acquired during the project, it is clear to me that our group was extremely lucky collecting the 2015 dataset. Indeed, both landfast ice and incoming waves were present, and rich dynamics including the development of cracks in the ice cover were observed. In addition, the direction of the wind kept the ice packed into the fjord instead of scattering it towards the open sea and, therefore, the instruments could be recovered. Had the wind blown towards the open ocean,

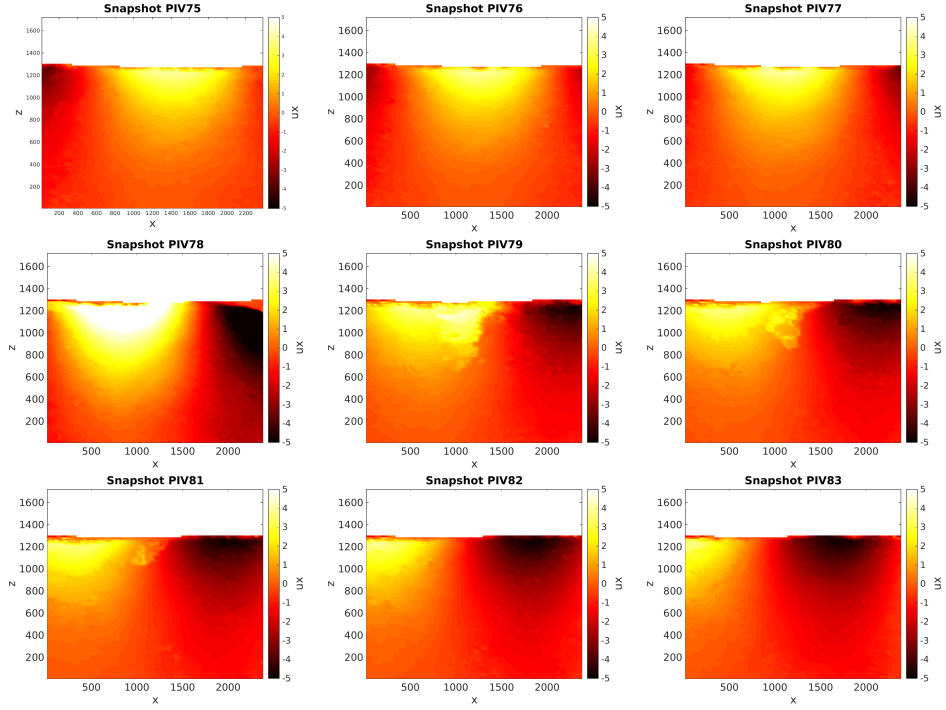


Figure 1.3: Raw PIV snapshots obtained from PIV images taken by Trygve Halsne during the course of his Master Thesis (Halsne, 2015). It proved impossible to reproduce similar turbulent bursts in subsequent experiments and, therefore, one can expect that an external source of disturbance probably is necessary to trigger the instability.

the instruments (and wave records) would have been lost. This pinpoints the necessity of including some satellite data transmission to our instruments, which our group will be working on in the years to come.

By contrast, at least one unsuccessful direction was found in the laboratory experiments, which regards the detection of turbulent bursts under waves propagating under inextensible latex covers. In a series of experiments performed during the Master Thesis of Trygve Halsne (Halsne, 2015), turbulent bursts were observed for high steepness waves (see Fig. 1.3). However, I was not able to reproduce those observations in later experiments, despite several months of investigation at the University of Oslo wave tank. A possibility is that additional disturbances, such as the presence of small bubbles under the cover, or water runup at the leading edge of the latex sheet, helped trigger those bursts in the original experiments and were later removed.

In addition, concerns should be raised about the validation of laboratory experiments compared with field measurements. Indeed, the Reynolds number is not scaled between waves at sea and wave experiments performed in the laboratory. More specifically, the very first imperative of laboratory experiments on waves is to be in the right water depth regime. Indeed, the wave velocity profile and the distribution of wave energy with depth is obviously very different between deep and shallow waves, and can have an effect on the physics at stake if some of the dissipation happens in the water under the ice. Due to the very limited depth of most wave tanks, this puts a sharp requirement on the minimum frequency that can be used for tests in the laboratory. Considering as a first approximation in all the discussion that follows that the deep water dispersion relation is enforced, so that $\omega^2 = gk$, one needs to enforce typically $kH > 1$, i.e. $\omega > \omega_{min} = \sqrt{g/H}$. In addition, the steepness of the waves must be kept moderate to limit nonlinear effects, typically $\epsilon = ka \approx 0.1$, i.e. $a < 0.1g/\omega^2$, where k is the wave vector and a the wave amplitude. If one considers that the amplitude-based Reynolds number defined in Babanin (2006), $Re_a = a^2\omega/\nu_{water}$, is the right non-dimensional parameter for describing turbulence under waves and large eddy structures under the ice, one then finds that in a laboratory experiment, with a wave-tank of depth H :

$$Re_a = \frac{a^2\omega}{\nu_{water}} < \frac{10^{-2}g^2}{\omega^3\nu_{water}} < \frac{10^{-2}g^{1/2}H^{3/2}}{\nu_{water}}. \quad (1.19)$$

This implies that, even in the case of a wave-tank several meters deep, the maximum Reynolds number that can be achieved in the laboratory for deep water waves of reasonable steepness is much lower than any typical swell on deep water. More specifically, the maximum Reynolds number obtained in a wave tank scales as the water depth to the power $3/2$. As a consequence, studying phenomena related to water wave turbulence and wave-induced eddy viscosity is challenging in the laboratory, as it is impossible to investigate whether a higher Reynolds number could lead to different physics. In particular, the Reynolds number attained in our laboratory experiments in a cold room make the full investigation of theories about wave-generated turbulence challenging. One could argue that turbulent flows exhibit a similar behavior above a critical Reynolds number which depends on the flow configuration, and therefore one could expect that reasonable results regarding the effect of turbulent processes could be obtained in large scale laboratory experiments without reproducing the full-scale Reynolds numbers, but more research is needed in this direction before any definitive statement can be made.

On a more technical point of view, this project has underlined the need for further development of a series of affordable, open source instruments relying on GPS, IMUs and Iridium communications for performing measurements of waves in ice. The capability and accuracy of the instruments developed to fulfil these requirements during the project have been carefully evaluated, to make sure that they can be used in a research context. While instruments very similar to those that will be further developed by our group are already used by another group of researchers (Doble et al., 2006, 2017), relatively little information is available about the details of their design. In the years to come, more work will be performed towards developing general purpose instruments and making their design freely available. This is, in the opinion of the author, the best answer that can be provided to the need of collecting drastically more field data in the polar regions.

1.5 Conclusion

The polar regions are the focus of increased attention due to a combination of environmental, political and economic reasons. One of the many factors that deeply influence these regions is the interaction between waves and ice. Prior to this dissertation, it had become clear that successful modeling of wave-ice interaction is challenging. In particular, both field and laboratory data were still too scarce to unambiguously point towards one successful wave-ice interaction model, and as a consequence a number of competing models exist where each model can be approximately fitted to the observations available. To remedy this problem, new experimental insights are needed.

In the present work, efforts were directed towards helping clarify these questions through two main axis. First, much work was performed towards the development of new methodology and instruments to perform measurements of the ice dynamics in the Arctic. Second, several datasets coming from both field and laboratory experiments were collected, analyzed, and compared with several theories. While more work is needed to bring definite answers, this work has contributed to turning the focus of research at least partly towards the dissipative phenomena happening in the water layer under the ice, rather than only the rheological properties of the ice cover as was implied by some of the recent models for wave propagation in ice covered sea.

Building, calibrating and validating models that integrate the effect of both the rheology of the ice and the dynamics of the water beneath the ice is made difficult

by the complexity, both physical and analytical, that is implied by describing all these phenomena at once. However, it appears as one of the long-term goals of wave-ice interaction study. Much work probably remains before such a complete model can be developed into maturity, and a number of complex phenomena that were not discussed here will also probably play a role, such as ice breakup by wave forcing.

1.6 Appendix: some technical aspects: an overview of the open source tools released in the course of the project

Several designs and code bases have been released as open source in the course of this project, both as code on the Github of the author and as a series of web pages. A list of released materials is provided here:

- The code and general design of the instruments that performed measurements of waves in ice using IMUs are presented in Rabault et al. (2017) and released on github:

<https://github.com/jerabaul29/LoggerWavesInIce> .

In addition, a web page presents some technical aspects of the systems used:

<https://folk.uio.no/jeanra/Microelectronics/MicrocontrollerBasedLoggers.html>

- The paddle control system and the coupled logging system used for the wave tank measurements in Svalbard are released on github:

<https://github.com/jerabaul29/ArduinoPaddleControl>

<https://github.com/jerabaul29/PaddleAndUltrasonicGauges> .

This system allows to perform automated measurements for a range of wave amplitude and frequencies.

- The logging system used during the experiments at HSVA is released on github:

https://github.com/jerabaul29/logging_ultrasonic_gauges .

Bibliography

- Ardhuin, F., Sutherland, P., Doble, M., and Wadhams, P. (2016). Ocean waves across the arctic: Attenuation due to dissipation dominates over scattering for periods longer than 19 s. *Geophysical Research Letters*, 43(11):5775–5783.
- Babanin, A. V. (2006). On a wave-induced turbulence and a wave-mixed upper ocean layer. *Geophysical Research Letters*, 33(20):n/a–n/a. L20605.
- Berkooz, G., Holmes, P., and Lumley, J. L. (1993). The proper orthogonal decomposition in the analysis of turbulent flows. *Annual review of fluid mechanics*, 25(1):539–575.
- Chang, M. and Bonnet, P. (2010). Monitoring in a high-arctic environment: Some lessons from MANA. *IEEE Pervasive Computing*, 9(4):16–23.
- Christensen, K. and Broström, G. (2008). Waves in sea ice. Technical report, Norwegian Meteorological Institute.
- Christensen, K. H. (2005). Transient and steady drift currents in waves damped by surfactants. *Physics of Fluids*, 17(4):042102.
- Collins III, C. O., Rogers, W. E., and Marchenko, A. (2016). On wave-ice interaction in the arctic marginal ice zone: Dispersion, attenuation, and ice response. Technical report, Naval Research Lab Stennis Detachment.
- Council, N., Board, T., Board, M., Studies, D., Board, P., and Needs, C. (2007). *Polar Icebreakers in a Changing World: An Assessment of U.S. Needs*. National Academies Press.
- De Carolis, G. and Desiderio, D. (2002). Dispersion and attenuation of gravity waves in ice: a two-layer viscous fluid model with experimental data validation. *Physics Letters A*, 305(6):399 – 412.
- Dierking, W. (2013). Sea ice monitoring by synthetic aperture radar. *Oceanography*, 26.

- Doble, M., Mercer, D., Meldrum, D., and Peppe, O. (2006). Wave measurements on sea ice: developments in instrumentation. *Annals of Glaciology*, 44:108–112.
- Doble, M. J., De Carolis, G., Meylan, M. H., Bidlot, J.-R., and Wadhams, P. (2015). Relating wave attenuation to pancake ice thickness, using field measurements and model results. *Geophysical Research Letters*, 42(11):4473–4481. 2015GL063628.
- Doble, M. J., Wilkinson, J. P., Valcic, L., Robst, J., Tait, A., Preston, M., Bidlot, J.-R., Hwang, B., Maksym, T., and Wadhams, P. (2017). Robust wavebuoys for the marginal ice zone: Experiences from a large persistent array in the beaufort sea. *Elem Sci Anth*, 5.
- Ewing, M. and Crary, A. (1934). Propagation of elastic waves in ice. part ii. *Physics*, 5(7):181–184.
- Feltham, D. (2015). Arctic sea ice reduction: the evidence, models and impacts. *Philosophical Transactions of the Royal Society of London A: Mathematical, Physical and Engineering Sciences*, 373(2045).
- Fox, C. and Haskell, T. G. (2001). Ocean wave speed in the antarctic marginal ice zone. *Annals of Glaciology*, 33:350–354.
- Gaster, M. (1962). A note on the relation between temporally-increasing and spatially-increasing disturbances in hydrodynamic stability. *Journal of Fluid Mechanics*, 14(2):222–224.
- Greenhill, A. G. (1886). Wave motion in hydrodynamics. *American Journal of Mathematics*, 9(1):62–96.
- Halsne, T. (2015). Eksperimentell undersøkelse av bølgeindusert strømning ved nærvær av ulike overflate-dekker. Master's thesis.
- Hayes, D. H., Jenkins, A., and McPhail, S. (2005). Surface wave decay and directional spectra in the marginal sea ice zone measured by an autonomous underwater vehicle. In *Proceedings of the IEEE/OES Eighth Working Conference on Current Measurement Technology*, 2005., pages 36–40.
- Keller, J. B. (1998). Gravity waves on ice-covered water. *Journal of Geophysical Research*, 103:7663–7669.
- Kerschen, G., Golinval, J.-c., Vakakis, A. F., and Bergman, L. A. (2005). The method of proper orthogonal decomposition for dynamical characterization and order reduction of mechanical systems: An overview. *Nonlinear Dynamics*, 41(1):147–169.

- Kohout, A. L., Penrose, B., Penrose, S., and Williams, M. J. (2015). A device for measuring wave-induced motion of ice floes in the antarctic marginal ice zone. *Annals of Glaciology*, 56(69):415–424.
- Kohout, A. L., Williams, M. J. M., Dean, S. M., and Meylan, M. H. (2014). Storm-induced sea-ice breakup and the implications for ice extent. *Nature*, 509(7502):604–7.
- Lamb, H. (1932). *Hydrodynamics*. Cambridge Mathematical Library. Cambridge University Press.
- Li, J., Kohout, A. L., Doble, M. J., Wadhams, P., Guan, C., and Shen, H. H. (2017). Rollover of apparent wave attenuation in ice covered seas. *Journal of Geophysical Research: Oceans*, 122(11):8557–8566.
- Liu, A. K., Holt, B., and Vachon, P. W. (1991). Wave propagation in the marginal ice zone: Model predictions and comparisons with buoy and synthetic aperture radar data. *Journal of Geophysical Research: Oceans*, 96(C3):4605–4621.
- Liu, A. K. and Mollo-Christensen, E. (1988). Wave propagation in a solid ice pack. *Journal of Physical Oceanography*, 18(11):1702 – 1712.
- Marchenko, A. and Lishman, B. (2017). The influence of closed brine pockets and permeable brine channels on the thermo-elastic properties of saline ice. *Phil. Trans. R. Soc. A*, 375(2086):20150351.
- Marchenko, A., Morozov, E., and Muzylev, S. (2013). Measurements of sea-ice flexural stiffness by pressure characteristics of flexural-gravity waves. *Annals of Glaciology*, 54(64):51–60.
- Marchenko, A., Rabault, J., Sutherland, G., Collins, C. O. I., Wadhams, P., and Chumakov, M. (2017). Field observations and preliminary investigations of a wave event in solid drift ice in the barents sea. In *24th International Conference on Port and Ocean Engineering under Arctic Conditions*.
- Marsan, D., Weiss, J., Larose, E., and Métaxian, J.-P. (2012). Sea-ice thickness measurement based on the dispersion of ice swell. *The Journal of the Acoustical Society of America*, 131(1):80–91.
- Martin, S. and Kauffman, P. (1981). A field and laboratory study of wave damping by grease ice. *Journal of Glaciology*, 27:283–313.
- McPhee, M. G. and Martinson, D. G. (1994). Turbulent mixing under drifting pack ice in the weddell sea. *Science*, 263(5144):218–221.

- Meylan, M. H., Bennetts, L. G., and Kohout, A. L. (2014). In situ measurements and analysis of ocean waves in the antarctic marginal ice zone. *Geophysical Research Letters*, 41(14):5046–5051.
- Mosig, J. E. M., Montiel, F., and Squire, V. A. (2015). Comparison of viscoelastic-type models for ocean wave attenuation in ice-covered seas. *Journal of Geophysical Research: Oceans*, 120(9):6072–6090.
- Newyear, K. and Martin, S. (1997). A comparison of theory and laboratory measurements of wave propagation and attenuation in grease ice. *Journal of Geophysical Research: Oceans*, 102(C11):25091–25099.
- Newyear, K. and Martin, S. (1999). Comparison of laboratory data with a viscous two-layer model of wave propagation in grease ice. *Journal of Geophysical Research: Oceans*, 104(C4):7837–7840.
- Overland, J. E. and Wang, M. (2013). When will the summer arctic be nearly sea ice free? *Geophysical Research Letters*, 40(10):2097–2101.
- Parkinson, C. (1997). *Earth From Above: Using Color-Coded Satellite Images to Examine the Global Environment*. University Science Books.
- Pfirman, S., Eicken, H., Bauch, D., and Weeks, W. (1995). The potential transport of pollutants by arctic sea ice. *Science of The Total Environment*, 159(2–3):129 – 146.
- Rabault, J., Halsne, T., Sutherland, G., and Jensen, A. (2016a). PTV investigation of the mean drift currents under water waves. In *Proceedings of the 18th Int. Lisb. Symp.*
- Rabault, J., Sutherland, G., Gundersen, O., and Jensen, A. (2017). Measurements of wave damping by a grease ice slick in svalbard using off-the-shelf sensors and open-source electronics. *Journal of Glaciology*, page 1–10.
- Rabault, J., Sutherland, G., Jensen, A., Christensen, K. H., and Marchenko, A. (2018). Experiments on wave propagation in grease ice: combined wave gauges and piv measurements. *submitted to Journal of Fluid Mechanics*.
- Rabault, J., Sutherland, G., Ward, B., Christensen, K. H., Halsne, T., and Jensen, A. (2016b). Measurements of waves in landfast ice using inertial motion units. *IEEE Transactions on Geoscience and Remote Sensing*, 54(11):6399–6408.
- Rigor, I. and Colony, R. (1997). Sea-ice production and transport of pollutants in the laptev sea, 1979–1993. *Science of The Total Environment*, 202(1–3):89 – 110. Environmental Radioactivity in the Arctic.

- Shao, Z.-D. and Ke, C.-Q. (2015). Spring–summer albedo variations of antarctic sea ice from 1982 to 2009. *Environmental Research Letters*, 10(6):064001.
- Shen, H., Perrie, W., Hu, Y., and He, Y. (2018). Remote sensing of waves propagating in the marginal ice zone by sar. *Journal of Geophysical Research: Oceans*, 123(1):189–200.
- Squire, V. (2007). Of ocean waves and sea-ice revisited. *Cold Regions Science and Technology*, 49(2):110 – 133.
- Squire, V., Dugan, J. P., Wadhams, P., Rottier, P. J., and K., A. (1995). Of ocean waves and sea-ice. *Annual Review of Fluid Mechanics*, 27:115 – 168.
- Squire, V. A. (1984). A theoretical, laboratory, and field study of ice-coupled waves. *Journal of Geophysical Research: Oceans*, 89(C5):8069–8079.
- Squire, V. A. (1993). A comparison of the mass-loading and elastic plate models of an ice field. *Cold Regions Science and Technology*, 21(3):219 – 229.
- Sutherland, G., Halsne, T., Rabault, J., and Jensen, A. (2017a). The attenuation of monochromatic surface waves due to the presence of an inextensible cover. *Wave Motion*, 68:88 – 96.
- Sutherland, G. and Rabault, J. (2016). Observations of wave dispersion and attenuation in landfast ice. *Journal of Geophysical Research: Oceans*, 121(3):1984–1997.
- Sutherland, G., Rabault, J., and Jensen, A. (2017b). A method to estimate reflection and directional spread using rotary spectra from accelerometers on large ice floes. *Journal of Atmospheric and Oceanic Technology*, 34(5):1125–1137.
- Sutherland, P. and Gascard, J.-C. (2016). Airborne remote sensing of ocean wave directional wavenumber spectra in the marginal ice zone. *Geophysical Research Letters*, 43(10):5151–5159. 2016GL067713.
- Thomson, J. and Rogers, W. E. (2014). Swell and sea in the emerging arctic ocean. *Geophysical Research Letters*, 41(9):3136–3140.
- Timco, G. and Weeks, W. (2010). A review of the engineering properties of sea ice. *Cold Regions Science and Technology*, 60(2):107 – 129.
- Tucker, M. and Pitt, E. (2001). *Waves in Ocean Engineering*. Elsevier ocean engineering book series. Elsevier.

- Wadhams, P. (1973). Attenuation of swell by sea ice. *Journal of Geophysical Research*, 78(18):3552–3563.
- Wadhams, P. (1975). Airborne laser profiling of swell in an open ice field. *Journal of Geophysical Research*, 80(33):4520–4528.
- Wang, R. and Shen, H. H. (2010a). Experimental study on surface wave propagating through a grease–pancake ice mixture. *Cold Regions Science and Technology*, 61(2 - 3):90 – 96.
- Wang, R. and Shen, H. H. (2010b). Gravity waves propagating into an ice-covered ocean: A viscoelastic model. *Journal of Geophysical Research: Oceans*, 115(C6).
- Weber, J. E. (1987). Wave attenuation and wave drift in the marginal ice zone. *Journal of Physical Oceanography*, 17(12):2351–2361.
- Zhao, X., Cheng, S., and Shen, H. H. (2017). Nature of wave modes in a coupled viscoelastic layer over water. *Journal of Engineering Mechanics*, 143(10):04017114.
- Zhao, X. and Shen, H. H. (2015). Wave propagation in frazil/pancake, pancake, and fragmented ice covers. *Cold Regions Science and Technology*, 113:71 – 80.

Chapter 2

Selected publications

This chapter is a selection of 7 works that were (or are being) published during the course of the project. Those publications are chosen to reflect both the laboratory experiments and fieldwork performed.

1. The first publication (Sutherland, G. and Rabault, J. (2016), "Observations of wave dispersion and attenuation in landfast ice", *Journal of Geophysical Research: Oceans*, 121(3):1984–1997) is an analysis of the measurements performed during the first measurement campaign in Svalbard. It includes discussions about wave propagation and attenuation. It is one of the few studies published in the literature where both the wave attenuation and dispersion relation are obtained in the case of field measurements. In this paper, we present a direct measurement of the dispersion relation for waves in continuous ice, and we observe the development of cracks which correspond to a suppression of the flexural effects.
2. The second publication (Rabault, J., Sutherland, G., Gunderson, O., and Jensen, A. (2017), "Measurements of wave damping by a grease ice slick in Svalbard using off-the-shelf sensors and open-source electronics", *Journal of Glaciology*, page 1–10) focuses on measurements of wave attenuation in grease ice, obtained during the second measurement campaign in Svalbard. Those data are especially relevant for calibration of wave in ice models. In addition, discussions of a more technical order about both the necessity of developing open source instruments and the importance of quantifying the quality of models using numerical indicators rather than visual observations

of quality of fit are presented.

3. The third publication (Sutherland, G., Rabault, J., and Jensen, A. (2017), "A Method to Estimate Reflection and Directional Spread Using Rotary Spectra from Accelerometers on Large Ice Floes", *Journal of Atmospheric and Oceanic Technology*, 34(5):1125–1137) is a more in-depth analysis of the rotary spectrum method used in the first publication, as well as a discussion of some difficulties encountered when performing measurements with IMUs. In particular, it is shown that measurements of reflected wave energy and directional spread of the incoming waves can be obtained from a study of the horizontal components of the ice acceleration.
4. The fourth publication (Marchenko, A., Rabault, J., Sutherland, G., Collins, C. O. I., Wadhams, P., and Chumakov, M. (2017), "Field observations and preliminary investigations of a wave event in solid drift ice in the Barents Sea", In *24th International Conference on Port and Ocean Engineering under Arctic Conditions*) summarizes a series of measurements performed in the Barents sea. There are two notable points with this study. First, several kinds of instruments relying on different measurement techniques (pressure sensors, ADVs and IMUs) were deployed at the same location. The results obtained from all instruments are very similar, therefore, providing a validation of the methodology used. In addition, the deployment configuration of the IMU instruments as a succession of triads presented in this article is a promising way to measure both the wave attenuation and the dispersion relation, without the need for any assumption on the wave direction of propagation.
5. The fifth publication (Rabault, J., Halsne, T., Sutherland, G., and Jensen, A. (2016), "PTV investigation of the mean drift currents under water waves", In *Proceedings of the 18th Int. Lisb. Symp.*) is a proceeding article, in which currents under inextensible covers are studied by means of PTV. We reached the conclusion that diffusion of vorticity due to the presence of an inextensible cover does influence the mean currents.
6. The sixth publication (Sutherland, G., Halsne, T., Rabault, J., and Jensen,

A. (2017), "The attenuation of monochromatic surface waves due to the presence of an inextensible cover", *Wave Motion*, 68:88 – 96) is another analysis of the effect of thin inextensible covers on wave propagation in the wave-tank, this time focusing on wave damping. It is shown that, in a well controlled wave tank situation where the surface cover is a smooth, non rigid surface, the damping predicted by Lamb is observed.

7. Finally, the seventh work (Rabault, J., Sutherland, G., Jensen, A., Christensen, K. H., and Marchenko, A. (2018), "Experiments on wave propagation in grease ice: combined wave gauges and PIV measurements", *under review*) presents the results obtained in a wave tank experiment in Svalbard, studying wave propagation under a layer of grease ice. Both wave attenuation and wavelength are compared with a series of one layer models. Satisfactory agreement is found between these one layer models and our experimental results. In addition, PIV measurements are performed for the first time in the case of waves propagating under grease ice. The exponential wave attenuation predicted theoretically is well visible, and vorticity created by colliding blocks of grease ice as well as mean currents are observed.

In addition, two publications written in the course of the project are not included in this Thesis. This includes one article about measurements of waves in landfast ice (Rabault, J.; Sutherland, G.; Ward, B.; Christensen, K.H.; Halsne, T.; Jensen, A. (2016), "Measurements of Waves in Landfast Ice Using Inertial Motion Units", *IEEE Transactions on Geoscience and Remote Sensing*, vol. 54, no. 11, pp. 6399-6408), which is mostly technical and has been extended and completed by Publication 1 and Publication 3, and one work that is the result of a side project (Rabault, J.; Kolaas, J.; Jensen, A. (2017), "Performing particle image velocimetry using artificial neural networks: a proof-of-concept", *Measurement Science and Technology* 28 (12), 125301).

2.1 Publication 1: Observations of wave dispersion and attenuation in landfast ice

Sutherland, G. and Rabault, J. (2016), "Observations of wave dispersion and attenuation in landfast ice", *Journal of Geophysical Research: Oceans*, 121(3):1984–1997.

RESEARCH ARTICLE

10.1002/2015JC011446

Key Points:

- Observations of the dispersion relation in landfast ice using inertial motion units
- Observed a transition from flexural-gravity waves to open water dispersion relation
- Transition period associated with up to 40% of the wave energy attenuated over one wavelength for frequencies greater than 0.15 Hz

Correspondence to:G. Sutherland,
graigors@math.uio.no**Citation:**

Sutherland, G., and J. Rabault (2016), Observations of wave dispersion and attenuation in landfast ice, *J. Geophys. Res. Oceans*, 121, 1984–1997, doi:10.1002/2015JC011446.

Received 6 NOV 2015

Accepted 2 MAR 2016

Accepted article online 7 MAR 2016

Published online 26 MAR 2016

Observations of wave dispersion and attenuation in landfast ice

Graig Sutherland¹ and Jean Rabault¹¹Department of Mathematics, University of Oslo, Oslo, Norway

Abstract Observations of wave propagation in landfast ice were obtained in Tempelfjorden, Svalbard during March 2015. Wave motion was measured near the ice edge using inertial motion units and consisted of a combination of swell from the North Atlantic and wind-generated waves. The waves were observed to be unidirectional in the ice with comparable magnitudes in the vertical and horizontal displacements. The dispersion relation was calculated from the measured phase difference between two adjacent sensors separated by a distance of approximately 60 m. Deviations from the gravity wave dispersion relation were observed during the growth phase of the waves and were consistent with the presence of flexural waves. This period of wave growth was accompanied by significant wave attenuation in the high frequency portion of the wave spectrum which persisted for 3–5 h.

1. Introduction

Surface water waves are known to have a significant impact on sea ice [Squire *et al.*, 1995; Squire, 2007] and can break large continuous ice sheets into much smaller fragments on the order of hours [Liu and Mollo-Christensen, 1988; Langhorne *et al.*, 1998; Collins *et al.*, 2015]. While theoretical aspects of wave-ice interaction have been studied for over a century [Greenhill, 1886], observational evidence is relatively sparse due to the difficult and dangerous environmental conditions where sea ice is present [Squire, 2007].

Changing ice conditions in both the Arctic and the Antarctic have created a renewed interest in field observations of wave propagation and attenuation in sea ice [Kohout *et al.*, 2014; Meylan *et al.*, 2014; Doble *et al.*, 2015; Collins *et al.*, 2015]. These studies have primarily focused on wave attenuation [Meylan *et al.*, 2014; Doble *et al.*, 2015] ice break up [Aspin *et al.*, 2014; Collins *et al.*, 2015] and possible feedback mechanisms between surface waves and changing ice conditions [Thomson and Rogers, 2014]. In contrast, the study of wave propagation in sea ice, specifically observations of the dispersion relation, have remained sparse [Squire, 2007].

Understanding how waves propagate in sea ice requires accurate knowledge of the dispersion relation [Liu and Mollo-Christensen, 1988; Squire, 2007]. Liu and Mollo-Christensen [1988] attributed a rapid break up event in pack ice to a focusing of wave energy 560 km from the ice edge. They attributed the large amplitude wave that was observed to nonlinear effects, which were enhanced in ice relative to open water due to the flexural and compression terms in the dispersion relation. Collins *et al.* [2015] also investigated some nonlinear aspects of waves in ice for a coastal region and suggested a possible feedback mechanism for large waves to penetrate further distances into pack ice.

While direct observations of the dispersion relation in ice are rare, there have been a few studies which have calculated it for various sizes of ice floes. Fox and Haskell [2001] calculated the dispersion relation for ice floes in the Antarctic marginal ice zone, and found a similar dispersion relation to that of open water with a slight modification due to the added mass from the ice floes. The dimensions of the ice floes were an order of magnitude smaller than the dominant wavelength and no evidence of flexural motion was observed.

Using an array of three seismometers on a 1 km ice floe, Marsan *et al.* [2012] calculated the dispersion relation for infragravity waves, with a peak period between 25 and 30 s, propagating in pack ice. While no flexural motions are expected to be present at this frequency, a bandpass filter was applied to separate various

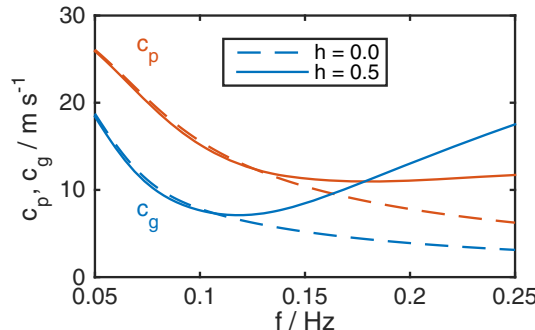


Figure 1. Phase (red) and group (blue) velocities for surface gravity waves (dashed lines) and flexural-gravity waves (solid lines) using an ice thickness of $h = 0.5$ m.

large errors and low correlations in the high frequency band, especially for the 0.14 and 0.25 Hz frequencies.

Presented here are observations of wave propagation near the ice-water edge in landfast ice. A brief review of some of the basic premises behind wave propagation in sea ice is presented in section 2. A description of the experimental setup and observations is presented in section 3 followed by spectral analysis of the observations in section 4. Details of the method and observations of the dispersion relation in sea ice is presented in section 5. Section 6 presents observations of wave attenuation near the edge. A discussion of the results and summary is presented in section 7.

2. Wave Propagation in Ice

There are two key components to wave propagation in sea ice: attenuation, which directly affects how the wave energy is lost, and the dispersion relation, which determines the rate of energy propagation. The two dominant mechanisms for wave attenuation in ice are due to discrete scattering from several small floes and/or inhomogeneities in the ice [Kohout and Meylan, 2008], or viscous effects associated with an ice continuum from frazil and grease ice [Weber, 1987], viscous effects in the water or ice [Wang and Shen, 2010] or ice creep [Wadhams, 1973]. Observations of attenuation have focused on lower frequency ice motion (less than 0.1 Hz) and use measurements over several kilometers to obtain accurate statistics [Meylan et al., 2014; Kohout et al., 2014; Doble et al., 2015].

The dispersion relation for waves in sea ice is derived by modeling the ice as a thin elastic plate [Squire et al., 1995]. For water of depth H , the dispersion relation relating the frequency f with the wavenumber k for an elastic plate can be written as [Liu and Mollo-Christensen, 1988]

$$(2\pi f)^2 = \frac{(gk + Dk^5 - Qk^3)}{\coth kh + kM} \quad (1)$$

where g is gravity, D is the bending modulus, Q is due to compression forces and M is due to the added mass of the ice sheet. The bending modulus D is a function of the rheological properties of the ice and is strongly dependent on the ice thickness, i.e., $D = Eh^3/\rho_w 12(1-\nu^2)$, where E is the Young's modulus, ν the Poisson ratio, h is the ice thickness and ρ_w is the water density. In general the contribution from ice compression, $Q = Ph/\rho_i$, and mass loading, $M = h\rho_i/\rho_w$, are much smaller than the gravity and flexural terms and can be neglected.

The elastic bending modulus of the sea ice cover strongly affects the dispersion relation due to the k^5 dependence and may lead to nonlinear effects even when the wave steepness ak , where a is the wave amplitude, is too small to create appreciable nonlinear effects in open water [Liu and Mollo-Christensen, 1988; Collins et al., 2015]. Figure 1 shows the phase and group velocities calculated from (1) for open water and for an ice cover of thickness $h = 0.5$ m assuming typical rheological parameters of $E = 3 \times 10^9$ N/m 2 , $P = 0$, $\rho_w = 1025$ kg/m 3 , $\rho_i = 922.5$ kg/m 3 [Squire et al., 1995]. Effects on the group velocity for an ice

frequency components. The dispersion relation was calculated from the time shift of the correlation between adjacent sensors of the bandpass filtered signal. This required an ice thickness to give the observed group velocity that was a factor of 2 smaller than in situ measurements. The discrepancy between the measured ice thickness and that inferred from wave propagation was assumed to arise from an omnidirectional swell spectrum and Marsan et al. [2012] obtained a more consistent estimate of the ice thickness using an inversion technique with a variable wave direction. Since ocean swell was the dominant source for wave motion there were

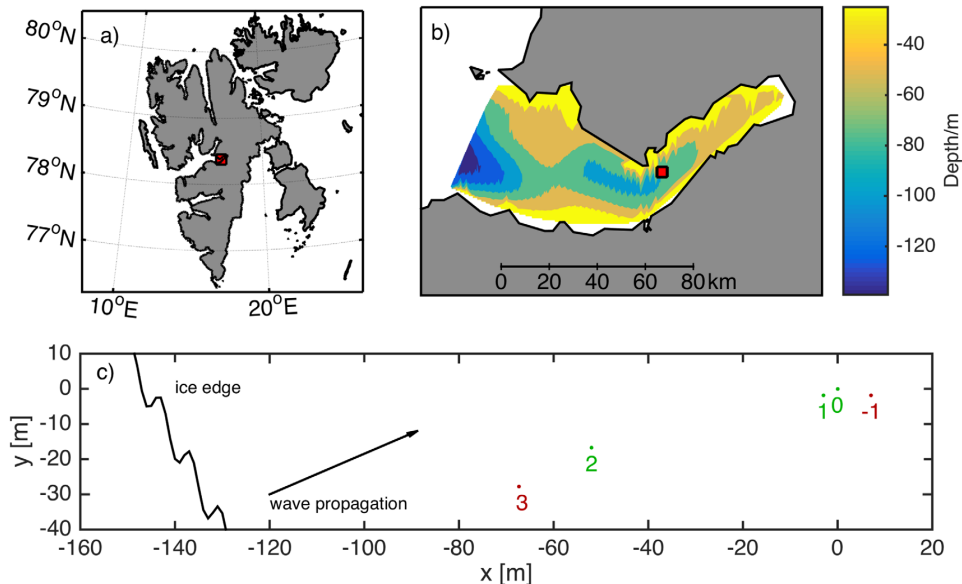


Figure 2. (a) Location of Tempelfjorden, Svalbard. The experiment site in Figures 2a and 2b is shown in red. (b) The bathymetry in Tempelfjorden. Relative sensor orientation is shown in Figure 2c along with the approximate ice edge and wave propagation direction. (c) The green points denote functioning wave sensors and the red points denote sensors that did not successfully record data.

thickness of 0.5 m can be seen in Figure 1. For frequencies greater than 0.18 Hz the group velocity (c_g) is greater than the phase velocity (c_p) with this transition to $c_g > c_p$ occurring at the local minimum of c_p .

3. Observations

Observations were made on Tempelfjorden, Svalbard between 25 March 2015 and 28 March 2015. Figure 2 shows the location of the experiment and orientation of wave sensors. The landfast ice was fastened to the shore along the edge of the fjord with the open water ice edge located approximately 100–200 m from the observation site (Figure 2c). Several inertial motion units (IMUs) and a single weather station were deployed on the sea ice. The IMUs were placed onto the ice and buried under 20–30 cm of snow. Two test holes were drilled near the measurement location, location “0” on Figure 2c, and the ice thickness was estimated from these cores to be between 0.5 and 0.6 m.

3.1. Wave Motion

The VN-100 IMU, manufactured by Vectornav Co., was used for detecting wave motion in the sea ice. Each sensor consisted of a 3-axis accelerometer, 3-axis gyroscope, 3-axis magnetometer, barometric sensor and a temperature sensor. Each IMU is factory calibrated for temperatures ranging from -40° to 85°C . The accelerometer has a factory rated resolution of $5 \times 10^{-3}g$ and the angular rate resolution is $3.5 \times 10^{-4} \text{ rad s}^{-1}$. The IMUs recorded the measurements at 10 Hz on a central data logger and the timestamp was synced with a GPS.

A total of 5 sensors were placed near the ice edge in Tempelfjorden, Svalbard. The sensors were deployed on 25 March 2015 16:00 until 27 March 2015 09:00. The location of each sensor, the approximate ice edge and the mean wave propagation direction are shown in Figure 2. Of the five sensors deployed, three successfully recorded data during the experiment, and are shown in green in Figure 2.

Wave displacement in the three orthogonal directions was calculated by double integrating the acceleration in each direction with respect to time. A second-order Butterworth bandpass filter was applied, with cutoff frequencies of 0.05 and 2 Hz, after each integration step to remove any low-frequency noise

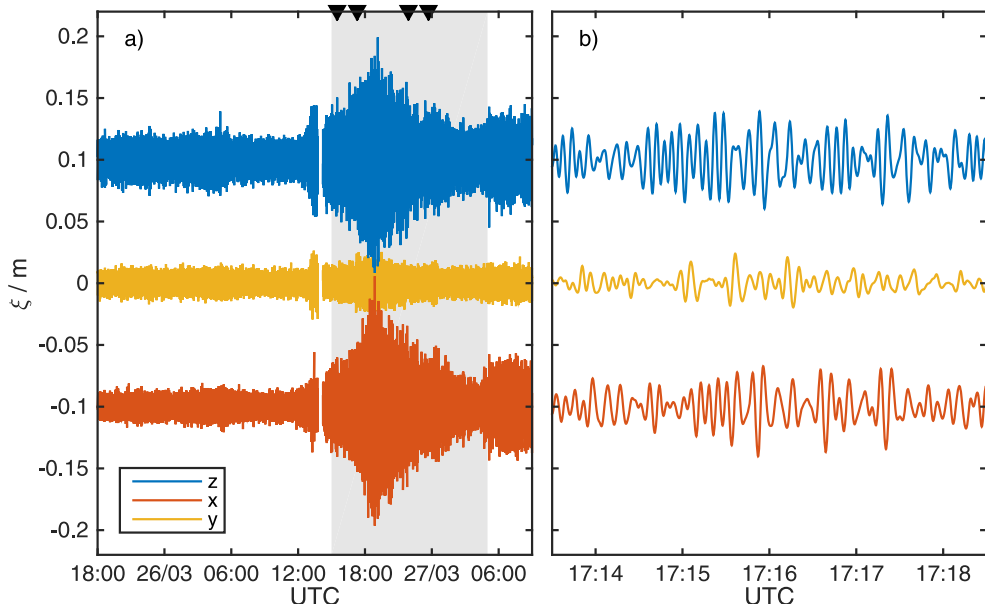


Figure 3. Time series of displacement in three directions for sensor 0. The z and x components are offset by ± 0.1 m for visualization. (a) The duration of observations with the shaded region denoting the time of wave activity used in the analysis and the black triangles denote the times for the examples in Figures 5, 6 and 7. (b) A 9 min segment centered at 26 March 2015 17:16 UTC corresponding to the second triangle to the left in Figure 3a.

associated with the integrated signal. Figure 3 shows an example time series for sensor 0 of the displacement (ξ) in the three orthogonal directions with z being the vertical and x the direction of wave propagation.

The vertical direction was determined from the gravity vector measured by the IMU as gravity was the only mean acceleration present over the duration of the experiment. This allows for the projection of the 3-axis accelerations onto this vertical vector z to obtain a true vertical motion. The horizontal direction was obtained by rotating the plane orthogonal to z to find a preferential propagation direction derived from the variance of the horizontal signal. This is compared with the magnetometer vector in the $x - y$ plane to ensure it is in the along-fjord direction. At our location, the horizontal magnetic field in the $x - y$ plane is an order of magnitude smaller than in the z direction with substantial variability on the order of hours, and thus the compass is only used to obtain the absolute mean direction over the duration of the observations. This direction is aligned with the fjord and is shown in Figure 2.

Although some wave motion was observed in the ice at 26 March 2015 12:00 UTC, we limit our analysis to the period from 26 March 2015 15:00 UTC up until 27 March 2015 05:00 (gray shaded region in Figure 3a). The 20 min gap in the data record at 26 March 2015 14:00 (Figure 3a) was due to the batteries being replaced. The observed wave motion was predominantly unidirectional with very little variance observed in the cross-fjord direction y (Figure 3).

3.2. Meteorological Conditions

Meteorological parameters such as mean wind speed, mean wind direction, air pressure, relative humidity and air temperature were measured using a Davis Vantage Pro 2 weather station mounted roughly 2 m above ice level. Ten min average values were recorded every 30 min. The meteorological conditions during the experiment are shown in Figure 4.

The wind direction in Figure 4a is aligned with the fjord so 0 corresponds to wind from the fjord to the sea and is in units of radians (positive clockwise). Before 26 March 2015 12:00 LMT the wind direction was coming from the fjord. At this time the wind shifted to the opposite direction and began to blow from the sea (Figure 4a). This shift corresponded with a rapid increase in wind speed from 1 m s^{-1} to 6 m s^{-1} over 2 h. Wave motion was observed over the time period when the wind direction was coming from the sea (shaded region, Figure 4).

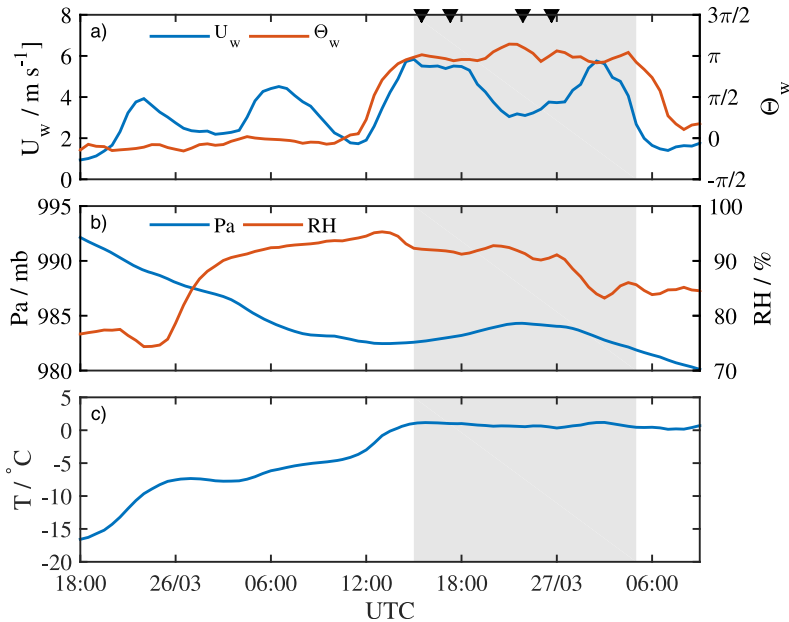


Figure 4. Meteorological observations of (a) the wind speed (U_w) and direction (Θ_w), (b) air pressure (Pa) and relative humidity (RH), and (c) air temperature (T) measured at 2 m above the ice. Θ_w is in radians and is relative to the fjord axis (positive clockwise) so 0 radians correspond to wind coming from the fjord. The shaded region shows the time period where wave motion was observed. The inverted black triangles denote the times for the examples in Figures 5, 6 and 7.

4. Wave Spectra

The power spectral density (PSD) was calculated for individual sections of 27.3 min (16,384 data points) by the Welch method [Earle, 1996; Kohout et al., 2015]. Each section was subdivided into subsections of 2048 points with a 50% overlap and a Hanning window was applied to each subsection. The resulting PSD is the average of the Fourier transform for each subsection having 21 degrees of freedom [Earle, 1996]. Examples of the calculated PSD for the displacement and slope are shown in Figure 5. The units for the displacement PSD is m^2/Hz and for the slope is rad^2/Hz . The noise threshold, chosen from visual inspection to be 10 times the factory noise level, is shown by the dashed line in Figure 5. Sensitivity to the choice of noise threshold is limited to the lower frequencies due to the $(2\pi f)^{-2}$ dependence on transforming from acceleration to displacement. This sensitivity to the noise threshold will have little affect on the frequency range where flexural waves are expected to occur (Figure 1). Observations were generally greater than the noise threshold for frequencies between 0.08 and 0.25 Hz (Figure 5).

4.1. Directional Spectra

Calculating the directional spectra in sea ice is difficult for several reasons. First, the dispersion relation is a complex function of various sea ice parameters which are difficult to determine a priori. While the dispersion relation can be calculated from the PSD of the elevation and horizontal slope, this is generally used in practice to verify the response function of the wave measuring device [Longuet-Higgins et al., 1963; Earle, 1996; Tucker and Pitt, 2001]. This point will be elaborated on in section 5.

To avoid the requirement of knowing the dispersion relation a priori to calculate the directional spectra, we take advantage of the fact that the wave motion in the ice was observed to be predominantly unidirectional, as can be seen in Figure 3, with comparable magnitudes in the vertical and horizontal displacements. Modeling the surface displacement as

$$\xi = \xi_z + i\xi_x, \quad (2)$$

where ξ_z and ξ_x are the vertical and horizontal displacements, allows for the calculated PSD of (2) to yield a rotary spectra where the orbital directionality can be determined.

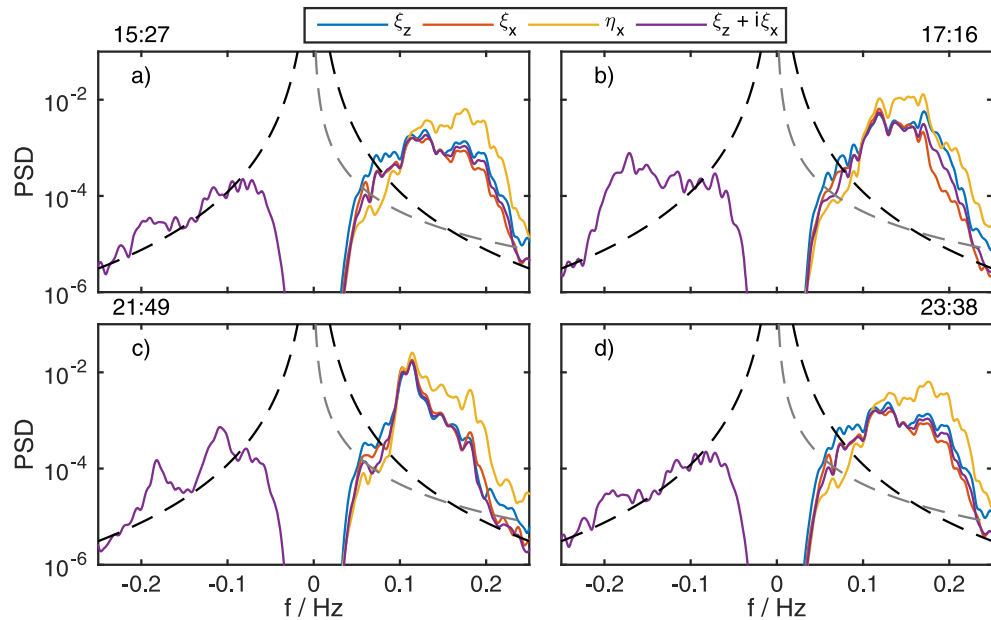


Figure 5. Power spectral density for the vertical displacement (ξ_z , blue), horizontal displacement (ξ_x , red), slope in direction of wave propagation (η_x , yellow, divided by 500 for visualization purposes) and complex displacement ($\xi_z + i\xi_x$, purple) for sensor 0 at (a) 15:27, (b) 17:16, (c) 21:49, and (d) 23:38 UTC on 26 March 2015. The blacked dashed line shows the noise level for the displacement while the gray dashed line shows the noise level for the surface slope.

Figure 5 shows the rotary PSD compared with the PSD from one dimensional measurements of the wave field. The positive frequencies denote the wave propagation into the ice and negative frequencies denote wave propagation toward the sea. The PSD was greater for waves propagating into the ice than out to sea. The PSD of (2) for positive frequencies was comparable in magnitude with the one dimensional estimates from the vertical and horizontal displacements (Figure 5). There were also appreciable peaks in the negative frequency component, especially around the time of Figure 5b, where the spectrum peak was at a higher frequency for the negative component than the positive. This will be explored further in section 6.

5. Dispersion Relation

In the absence of high resolution space and time observations to directly calculate the wavenumber and frequency, the dispersion relation can be inferred from correlating signals between adjacent sensors [Fox and Haskell, 2001; Marsan et al., 2012] or by a single wave buoy measurement by comparing the PSD from the heave with the PSDs from the pitch and roll [Longuet-Higgins et al., 1963; Long, 1980; Kuik et al., 1988],

$$k = \frac{S_p(f) + S_r(f)}{S_h(f)} \quad (3)$$

where $S_h(f)$, $S_p(f)$ and $S_r(f)$ are the PSDs from the heave, pitch and roll respectively. In practice, (3) is not an ideal method for measuring the dispersion relation as the precise response of the measuring system, which includes the coupling of the measuring device with the media as well as the temporal response of the heave, pitch and roll sensors, must be accurately known [Longuet-Higgins et al., 1963]. Often (3) is used to check the validity of the wave spectrum with the known dispersion relation [Longuet-Higgins et al., 1963; Earle, 1996; Tucker and Pitt, 2001].

A more robust method to measure the dispersion relation can be calculated by looking at correlations between sensors that are relatively close to one another (preferably a distance on the order of one wavelength). The dispersion relation is calculated from the simultaneous phase difference, ϕ_{mn} , between sensors m and n separated by a horizontal displacement \mathbf{x}_{mn} , i.e.,

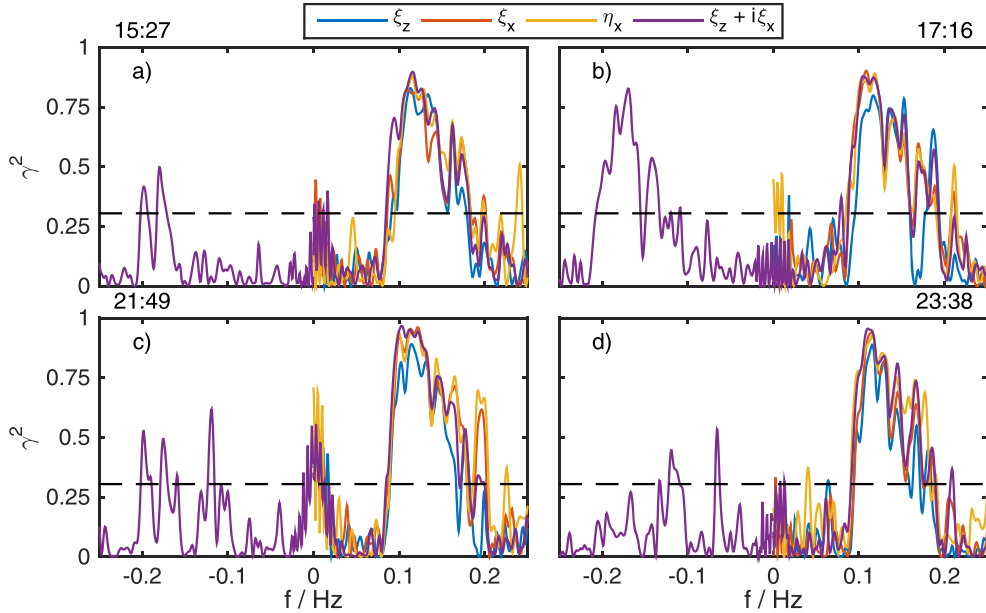


Figure 6. Spectral coherency (γ^2) between sensors 0 and 2 for the vertical displacement, horizontal displacement (ξ_x , red), slope in direction of wave propagation (η_x , yellow) and complex displacement ($\xi_z + i\xi_x$, purple) at (a) 15:27, (b) 17:16, (c) 21:49, and (d) 23:38 UTC on 26 March 2015. The horizontal dashed line denotes the coherency required to reject the null hypothesis with 99.9% confidence.

$$\phi_{mn} = \mathbf{k} \cdot \mathbf{x}_{mn} \quad (4)$$

where \mathbf{k} is the vector wavenumber. There will be phase wrapping associated with wavelengths less than $|\mathbf{x}_{mn}|$, but this will be limited to no more than one phase wrap for our given sensor spacing of 60 m and a frequency range $0.1 < f < 0.25$ Hz.

To relate frequency f and wavenumber k , ϕ was calculated in the spectral domain from the cospectral density between adjacent sensors S_{mn} , i.e.,

$$\phi_{mn}(f) = \tan^{-1} \left(\frac{\text{Im}[S_{mn}(f)]}{\text{Re}[S_{mn}(f)]} \right). \quad (5)$$

Equation (5) was used to equate f and k assuming the signal at both locations was correlated and both were above the noise threshold. The spectral coherence (γ) between two signals was calculated with

$$\gamma_{mn}^2(f) = \frac{|S_{mn}(f)|^2}{|S_{mm}(f)||S_{nn}(f)|}. \quad (6)$$

To reject the hypothesis that the signals were not correlated at the 99.9% confidence level requires $\gamma^2 \geq 0.305$ for our PSD estimates with 21 degrees of freedom [Amos and Koopmans, 1963].

Figure 6 shows γ^2 for the same time intervals as Figure 5. Between 0.1 and 0.2 Hz the signal was predominantly coherent for positive frequencies. The corresponding phase shift ϕ for conditions where the coherency and signal are above their respective noise thresholds is shown in Figure 7. These were compared with the expected phase shift for the open water dispersion relation (in black) and for flexural-gravity waves (in gray) given the known distance between the sensors. There was a slight deviation from the open water dispersion for the earliest time (Figure 7a) consistent with flexural waves with an estimated ice thickness of 0.5 m. At subsequent times there is no clear evidence for flexural waves from the observed phase lag.

Figure 7 also demonstrates the relatively narrow bandwidth in which the dispersion relation from flexural-gravity waves can be differentiated from the open water dispersion relation. Equation (1) deviates from the gravity dispersion relation between the frequencies 0.11 and 0.20 Hz at which point it will cross the

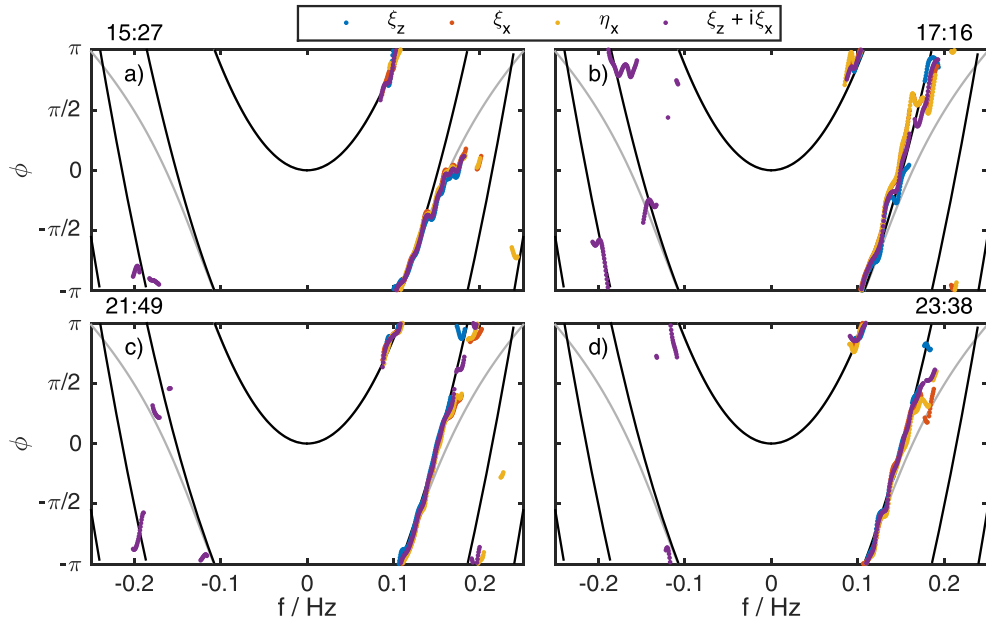


Figure 7. Phase angle between sensors 0 and 2 for the vertical displacement (ξ_z , blue), horizontal displacement (ξ_x , red), slope in direction of wave propagation (η_x , yellow) and complex displacement ($\xi_z + i\xi_x$, purple) at (a) 15:27, (b) 17:16, (c) 21:49, and (d) 23:38 UTC on 26 March 2015. The expected phase difference for open water (black) and for an 0.5 m thick ice sheet (sheet) is also shown.

wrapped phase from the gravity waves with the slower phase velocity. The difference can easily be spotted with a continuous spectrum from the slope in ϕ , but if discrete frequencies were analyzed, such as in *Marsan et al. [2012]*, care must be taken to avoid ambiguities which could arise.

Figure 8 shows the calculated dispersion relation using (4) and (5) with the color denoting the time in UTC. The dispersion relation in Figure 8 was calculated using the complex height ξ to obtain the phase lag $\phi_{mn}(f)$, but there was little observed variation if the coherency of other wave signals were used. For frequencies between 0.08 and 0.12 Hz and for an ice thickness up to 0.75 m, gravity dominates the dispersion relation and the observations coincided with the open water dispersion relation (Figure 8). For frequencies

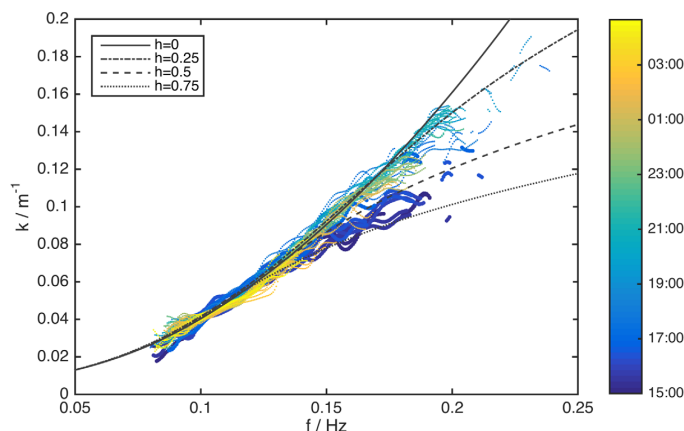


Figure 8. The dispersion relation calculated by the phase difference between sensors 2 and 0 and sensors 1 and 0. The color denotes the time of day. Times before 17:00 are denoted by slightly larger symbols. The black lines show the dispersion relation for various values of ice thickness h (solid = 0 m, dashed-dot = 0.2 m, dashed = 0.5 m, and dotted = 1 m).

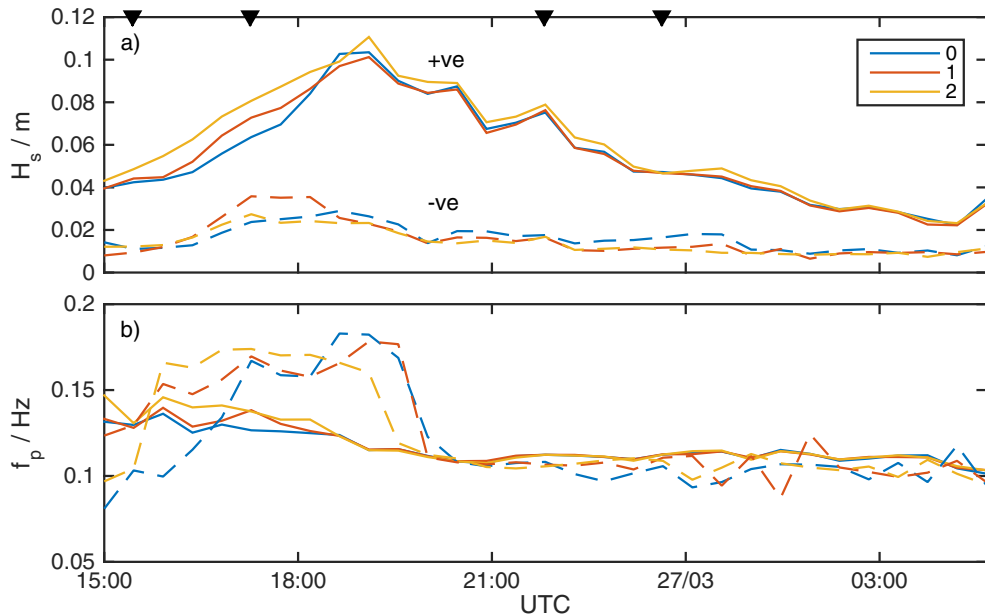


Figure 9. (a) Significant wave height and (b) peak frequency at the three sensor locations. The forward propagation in the ice (+ve) and propagation out to sea (-ve) are shown by the solid and dashed lines respectively. The inverted black triangles denote the times for the examples in Figures 5–7. The color denotes individual IMUs.

greater than 0.12 Hz there was an increasing amount of time-dependent scatter in the calculated dispersion relation. Before 17:00 UTC there was a clear deviation from the gravity wave dispersion relation corresponding to an ice thickness $0.5 < h < 0.75$ (Figure 8, heavy dots). After 17:00 UTC, this deviation vanished and the dispersion relation was similar to that of open water (Figure 8, light dots).

6. Wave Attenuation

The significant wave height H_s and peak frequency f_p are shown in Figure 9 for the three sensor locations near the ice edge. The solid lines represent wave propagating into the fjord and the dashed lines represent propagation out of the fjord. There was a clear gradient in H_s between the three sensors from 15:00 to 19:00 where the significant wave height was increasing. This time frame corresponded to a small peak in the reflected H_s (dashed line Figure 9a) and f_p (dashed line Figure 9b) suggesting that there might exist a relatively high amount of reflected energy in the higher frequency portion of the wave spectrum.

Figure 10 shows the spectrogram for the ratio of the PSD calculated at (a) sensor location 0 and 2 and (b) 1 and 2. In Figure 10, no decrease in energy corresponds to a value 0 and a 100% reduction corresponds to a value of 1. Wave attenuation was predominantly small except for the time period between 15:00 and 20:00 where as much as 80% of the energy was attenuated for frequencies greater than 0.15 Hz.

The mean spectral attenuation shown in Figure 10 was averaged between 15:00 and 20:00 as a function of frequency (Figure 11). A gradual increase in the spectral attenuation was observed for frequencies greater than 0.15 Hz. The attenuation increased linearly from 0% at $f = 0.15$ Hz to nearly 40% at $f = 0.23$ Hz. While wave-wave nonlinear interactions can redistribute energy in the spectrum, these effects are slow and will only accumulate over distances on the order of ten wavelengths [Liu and Mollo-Christensen, 1988].

A peak was also observed in the negative frequencies between 15:00 and 20:00 (Figure 9), suggesting that reflection/scattering may be involved with the wave attenuation observed at high frequencies. Although the source of the reflection in the sea ice was unknown, we can compare the spectral energy propagating into the ice with that propagating out at each sensor location. The spectrogram, at location 0, for positive and negative frequencies can be seen in Figure 12 and the peak frequency is shown by the dashed lines. The peak frequency for the positive frequencies slowly decayed over time while the peak frequency for the negative

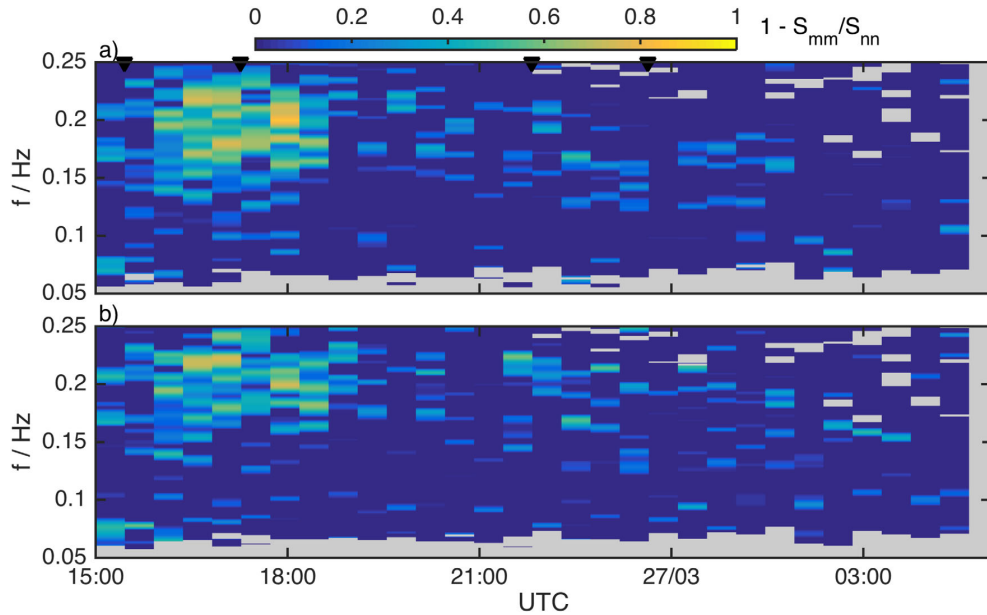


Figure 10. Spectral attenuation shown between sensors (a) 0 and 2 and (b) 1 and 2 for the forward propagating wave energy. The inverted black triangles denote the times for the examples in Figures 5–7.

frequencies was more variable (Figure 12b). Most notably was the local peak frequency for the negative frequencies between 0.15 and 0.18 Hz observed between 17:00 and 20:00 (Figure 12b). This peak in the negative frequencies was preceded by sensors 1 and 2 by 1–2 h (Figure 9b) suggesting a complex frequency dependence on the effects from ice draft and cracks which affected the wave reflection [Squire, 2007].

An estimate for the ratio of reflected energy is given by S_{-ve}/S_{+ve} , and is shown in Figure 13 for sensor 0. Enhanced values of S_{-ve}/S_{+ve} were observed from 17:00 in the frequency range 0.15–0.2 Hz. Although the enhancement was greatest between 17:00 and 20:00 UTC, corresponding to where the peak frequency for

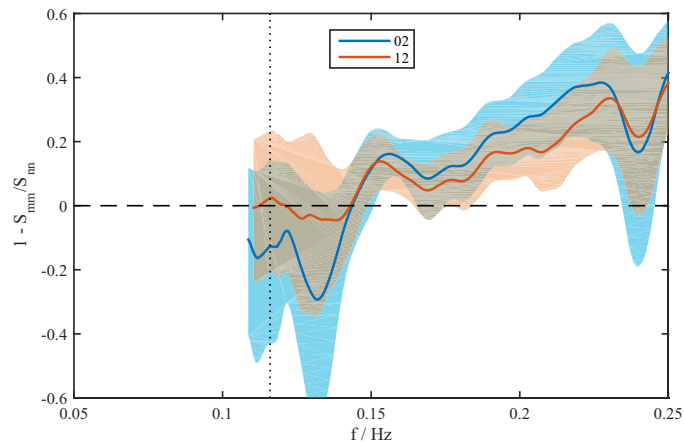


Figure 11. Mean attenuation calculated between 15:00 and 20:00 on 26 March 2015. Shaded region shows the 95% confidence interval as calculated using the bootstrap method. The vertical dotted line shows the mean peak frequency associated with incoming swell. In the legend, 02 refers to the attenuation between sensors 2 and 0, while 01 refers to the attenuation between sensors 1 and 0.

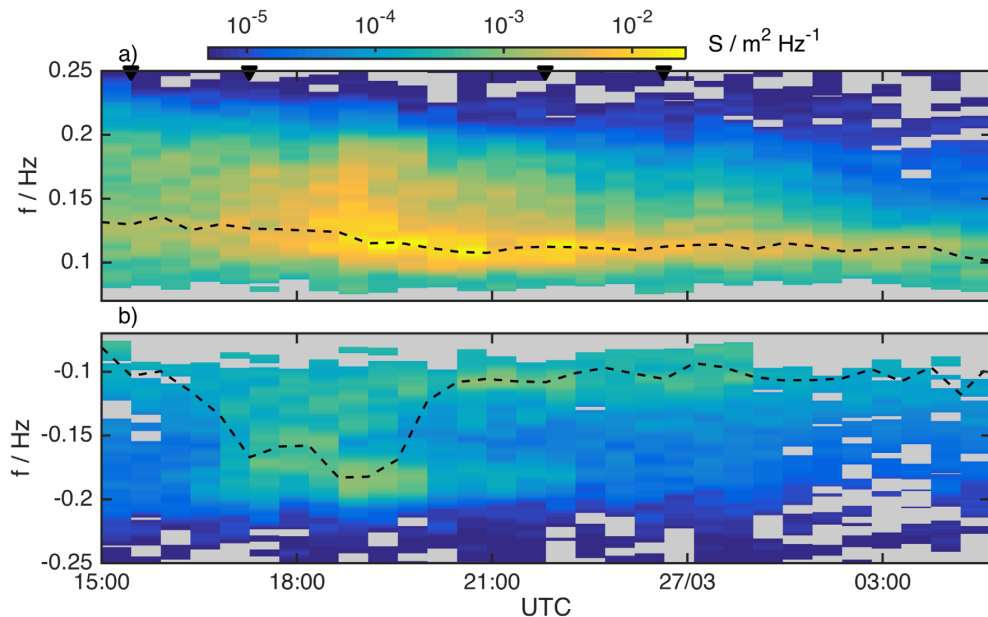


Figure 12. Power spectral density for (a) positive and (b) negative rotary components for sensor 0. The dashed line shows the peak frequency. The inverted black triangles denote the times for the examples in Figures 5–7.

the reflected wave was a maximum, the enhancement appeared to persist throughout the record for frequencies between 0.15 and 0.2 Hz when the wave motion was above the detectable limit (Figure 13).

A mean spectral reflection coefficient is calculated for the period between 15:00 and 20:00, similar to the averaging for the absolute attenuation in Figure 11, and is shown in Figure 14. This ratio estimates an “integrated reflection coefficient” for a particular sensor location as the exact location of where the reflections took place in the ice were not known. However, the location can not be too far as there is high attenuation

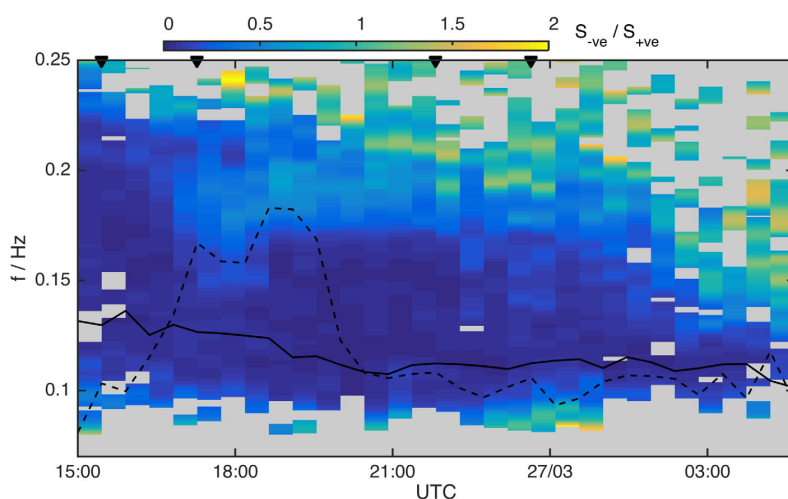


Figure 13. Ratio of negative to positive rotary spectra components at sensor 0. The solid line shows the positive peak frequency and the dashed line is the peak frequency for the negative component. The inverted black triangles denote the times for the examples in Figures 5–7.

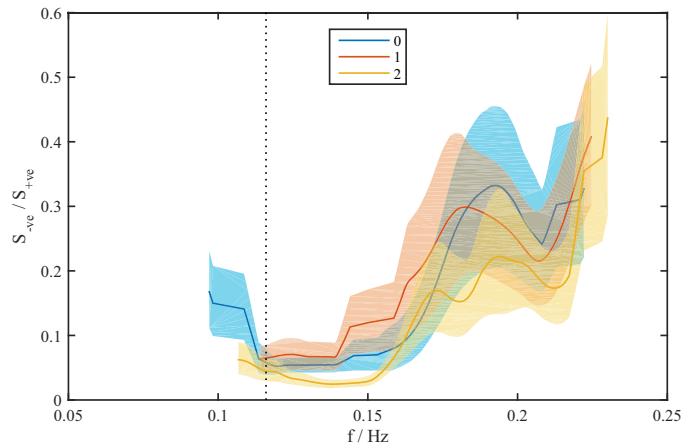


Figure 14. Mean ratio of negative to positive rotary spectra components calculated between 15:00 and 20:00 on 26 March 2015. Shaded region shows the 95% confidence interval as calculated using the bootstrap method. The vertical dotted line shows the mean peak frequency associated with incoming swell. The color denotes individual IMUs.

for frequencies greater than 0.15 Hz (Figure 11). Figure 14 has a similar structure to Figure 11 with a gradual increase in S_{-ve}/S_{+ve} for frequencies greater than 0.15 Hz.

7. Summary and Discussion

Observations of wave motion were obtained using inertial motion units near the ice-water edge in landfast ice located in Tempelfjorden, Svalbard. The dispersion relation was calculated from the spectral phase shift measured between adjacent sensors. Evidence of flexural-gravity waves, as determined from the dispersion relation, were observed during the first 2 h of the wave motion at which point there was a transition to a gravity wave dispersion relation. Cracks in the ice were not quantified, but there was a noticeable increase in their number over approximately 36 h between deployment and recovery of the sensors. These cracks appear to have an impact on the ability of the ice cover to transmit flexural stress and a shift in the dispersion relation from flexural-gravity waves to gravity waves was observed over a short period of time.

There are other possible processes, other than the presence of flexural waves, which would lead to a deviation from the open water dispersion relation as seen in Figure 8. If the medium was moving, there will be a Doppler shift and/or refraction which will depend on u/c_p where u is the velocity of the moving medium and c_p is the phase velocity. Our observations are obtained from landfast ice and u should be zero. If cracks developed and the ice moved with the local tidal currents, which are less than 0.1 m s^{-1} in this region [Kowalik et al., 2015], then the change in frequency will be proportional to $u/c_p \approx 0.1/10 = 0.01$ which is much smaller than the observed deviation for frequencies greater than 0.15 Hz. Wave refraction can also occur due to a change in the medium velocity, but this too shall scale with u/c_p , and our value of 0.01 is much too low for appreciable refraction [Johnson, 1947].

Another possible source of deviation from the open water dispersion relation comes from using (4) and the possible misalignment between \mathbf{k} and \mathbf{x}_{mn} for certain frequencies. For the observed deviation in Figure 8, the angle between \mathbf{k} and \mathbf{x}_{mn} would have to increase as a function of frequency, which seems physically implausible in the absence of refraction. It is possible that there is a complex wave pattern due to scattering of high frequency energy, but our observations are insufficient to address such spatial heterogeneity.

Appreciable attenuation in the wave spectral energy density was observed over approximately one wavelength between approximately 15:00 and 20:00 on 26 March 2015 (Figure 9). The wave propagation direction was predominantly along the fjord and was separated into a positive propagating wave (i.e., into the ice) and a negative propagating component (i.e., back to sea) via a rotary spectrum of the surface

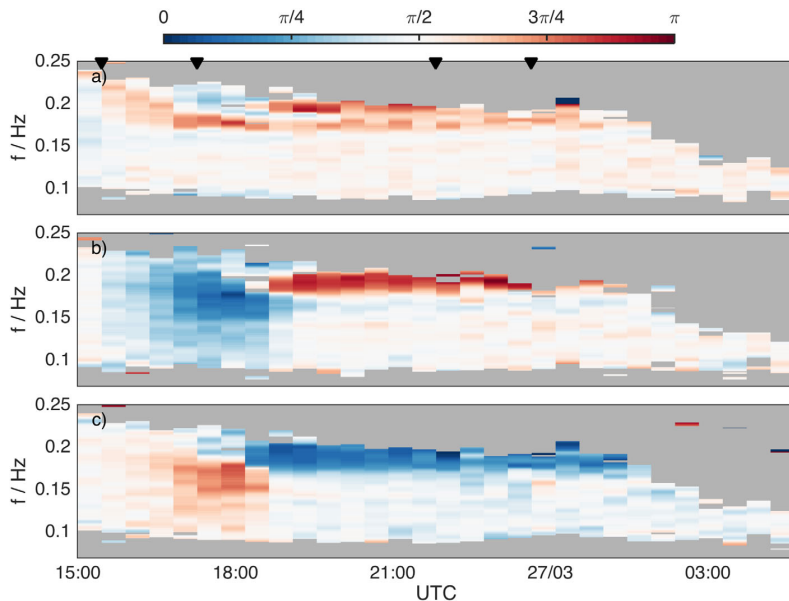


Figure 15. Phase difference between vertical and horizontal displacement for (a) sensor 2, (b) sensor 1 and (c) sensor 0. The inverted black triangles denote the times for the examples in Figures 5–7.

displacement. For frequencies less than 0.15 Hz, which was close to the frequency where the phase and group velocities are equal assuming an ice thickness of 0.5 m (Figure 1), there was no appreciable attenuation. For larger frequencies the attenuation in the power spectral density was observed to steadily increase (Figure 11). Confidence intervals are relatively large, but for frequencies around 0.2 Hz approximately 10–40% of the energy density at the outermost sensor was attenuated. The high wave attenuation occurred over the same time-spectral space where the deviation from the open water dispersion relation (Figure 8), which we suspect to be due to flexural waves, were present. The frequency dependence of the ratio of reflected to propagating wave energy (Figure 14) was very similar to that observed for the wave attenuation with similar confidence intervals for the estimates, which is consistent with scattering being the dominant process for wave attenuation in this frequency range of 0.15–0.25 Hz. A greater spatial sampling of the wave motion is required to investigate how high frequency wave energy is scattered near the ice edge.

An interesting feature of the ice motion was the comparable amplitudes in the horizontal and vertical displacements. The wave motion was expected to be primarily in the vertical [e.g., Fox and Haskell, 2001] and this strong horizontal motion is somewhat puzzling. It could be that cracks in the ice affected the horizontal motion or it may be that this motion is a property of wave propagation in an ice covered sea. Further experiments would be necessary to determine under what conditions horizontal and vertical motion are comparable.

The phase relation between the vertical and horizontal motion was calculated from the cospectra between the two signals. Figure 15 shows the phase difference between horizontal and vertical motions for the three sensors. For frequencies less than 0.17 Hz the phase difference was close to $\pi/2$ except for sensors 0 and 1 where the phase difference was π or 0 consistent with rectilinear motion. For all sensors at frequencies greater than 0.17 the phase was 0 or π . The time and frequencies where the wave motion was out of quadrature, i.e., $\phi \neq \pi/2$, (Figure 15) coincided with the time and frequencies where wave attenuation was the largest (Figure 11). It would be interesting to investigate whether the surface motion was related to stresses in the ice, analogous to the case of wave stresses in the ocean [Cavaleri and Zecchetto, 1987], as this phase shift between vertical and horizontal motions may be an important component of rapid break up of coastal sea ice.

Acknowledgments

The authors are grateful to Brian Ward at NUI Galway for providing the data logger and IMUs which made the experiment possible. We also thank Atle Jensen, Olav Gunderson, Erika Lindstrøm from UiO, Kai Christensen from met.no and Eugene Morozov from the Shirshov Institute for all their help with the field work. A special thanks to Aleksey Marchenko and the entire logistics staff at UNIS for their support on Svalbard. The authors are especially thankful to Trygve Halsne for his help in the preparation and execution of the field work. Funding for the experiment was provided by the Norwegian Research Council under the PETROMAKS2 233901 project. The data used in this study are available by request from the corresponding author at graigors@math.uio.no. The authors are grateful to the two anonymous reviewers whose comments have greatly improved the manuscript.

References

- Amos, D., and L. Koopmans (1963), *Tables of the Distribution of the Coefficient of Coherence for Stationary Bivariate Gaussian Processes*, Sandia Corp., Albuquerque, N. M.
- Asplin, M. G., R. Scharian, B. Else, S. Howell, D. G. Barber, T. Papakyriakou, and S. Prinsenberg (2014), Implications of fractured Arctic perennial ice cover on thermodynamic and dynamic sea ice processes, *J. Geophys. Res. Oceans*, 119, 2327–2343, doi:10.1002/2013JC009557.
- Cavalieri, L., and S. Zecchetto (1987), Reynolds stresses under wind waves, *J. Geophys. Res.*, 92(C4), 3894–3904.
- Collins, C. O., III, W. E. Rogers, A. Marchenko, and A. V. Babanin (2015), In situ measurements of an energetic wave event in the arctic marginal ice zone, *Geophys. Res. Lett.*, 42, 1863–1870, doi:10.1002/2015GL063063.
- Doble, M. J., G. D. Carolis, M. H. Meylan, J. R. Bidlot, and P. Wadhams (2015), Relating wave attenuation to pancake ice thickness, using field measurements and model results, *Geophys. Res. Lett.*, 42, 4473–4481, doi:10.1002/2015GL063628.
- Earle, M. D. (1996), Nondirectional and directional wave data analysis procedures, *NDBC Tech. Doc* 96-01, Natl. Data Buoy Cent., Natl. Oceanic and Atmos. Admin., U.S. Dep. of Commer., Washington, D. C.
- Fox, C., and T. G. Haskell (2001), Ocean wave speed in the Antarctic marginal ice zone, *Ann. Glaciol.*, 33(1), 350–354.
- Greenhill, A. G. (1886), Wave motion in hydrodynamics, *Am. J. Math.*, 9(1), 62–96.
- Johnson, J. (1947), The refraction of surface waves by currents, *Eos Trans. AGU*, 28(6), 867–874.
- Kohout, A., M. Williams, S. Dean, and M. Meylan (2014), Storm-induced sea-ice breakup and the implications for ice extent, *Nature*, 509(7502), 604–607.
- Kohout, A., and M. H. Meylan (2008), An elastic plate model for wave attenuation and ice floe breaking in the marginal ice zone, *J. Geophys. Res.*, 113, C09016, doi:10.1029/2007JC004434.
- Kohout, A., L. B. Penrose, S. Penrose, and M. J. M. Williams (2015), A device for measuring wave-induced motion of ice floes in the Antarctic marginal ice zone, *Ann. Glaciol.*, 56(69), 415–424.
- Kowalik, Z., A. Marchenko, D. Brazhnikov, and N. Marchenko (2015), Tidal currents in the western Svalbard fjords, *Oceanologia*, 57(4), 318–327.
- Kuij, A., G. P. Van Vledder, and L. Holthuijsen (1988), A method for the routine analysis of pitch-and-roll buoy wave data, *J. Phys. Oceanogr.*, 18(7), 1020–1034.
- Langhorne, P. J., V. A. Squire, and C. Fox (1998), Break-up of sea ice by ocean waves, *Ann. Glaciol.*, 27, 438–442.
- Liu, A. K., and E. Mollo-Christensen (1988), Wave propagation in a solid ice pack, *J. Phys. Oceanogr.*, 18(11), 1702–1712.
- Long, R. B. (1980), The statistical evaluation of directional spectrum estimates derived from pitch/roll buoy data, *J. Phys. Oceanogr.*, 10(6), 944–952.
- Longuet-Higgins, M. S., D. Cartwright, and N. Smith (1963), Observations of the directional spectrum of sea waves using the motions of a floating buoy, in *Ocean Wave Spectra*, pp. 111–136, Prentice Hall, Englewood Cliffs, N. J.
- Marsan, D., J. Weiss, E. Larose, and J.-P. Métaixian (2012), Sea-ice thickness measurement based on the dispersion of ice swell, *J. Acoust. Soc. Am.*, 131(1), 80–91.
- Meylan, M. H., L. G. Bennetts, and A. L. Kohout (2014), In situ measurements and analysis of ocean waves in the Antarctic marginal ice zone, *Geophys. Res. Lett.*, 41, 5046–5051, doi:10.1002/2014GL060809.
- Squire, V. (2007), Of ocean waves and sea-ice revisited, *Cold Reg. Sci. Technol.*, 49(2), 110–133.
- Squire, V. A., J. P. Dugan, P. Wadhams, P. J. Rottier, and A. K. Liu (1995), Of ocean waves and sea ice, *Annu. Rev. Fluid Mech.*, 27(1), 115–168.
- Thomson, J., and W. E. Rogers (2014), Swell and sea in the emerging arctic ocean, *Geophys. Res. Lett.*, 41, 3136–3140, doi:10.1002/2014GL059983.
- Tucker, M. J., and E. G. Pitt (2001), *Waves in Ocean Engineering*, vol. 5, 550 pp., Elsevier.
- Wadhams, P. (1973), Attenuation of swell by sea ice, *J. Geophys. Res.*, 78(18), 3552–3563.
- Wang, R., and H. H. Shen (2010), Gravity waves propagating into an ice-covered ocean: A viscoelastic model, *J. Geophys. Res.*, 115, C06024, doi:10.1029/2009JC005591.
- Weber, J. E. (1987), Wave attenuation and wave drift in the marginal ice zone, *J. Phys. Oceanogr.*, 17(12), 2351–2361.

2.2 Publication 2: Measurements of wave damping by a grease ice slick in Svalbard using off-the-shelf sensors and open-source electronics

Rabault, J., Sutherland, G., Gundersen, O., and Jensen, A. (2017), "Measurements of wave damping by a grease ice slick in Svalbard using off-the-shelf sensors and open-source electronics", *Journal of Glaciology*, page 1–10.

Measurements of wave damping by a grease ice slick in Svalbard using off-the-shelf sensors and open-source electronics

JEAN RABAULT, GRAIG SUTHERLAND, OLAV GUNDERSEN, ATLE JENSEN

Department of Mathematics, University of Oslo, Oslo, Norway

Correspondence: Jean Rabault <jeanra@math.uio.no>

ABSTRACT. Versatile instruments assembled from off-the-shelf sensors and open-source electronics are used to record wave propagation and damping measured by Inertial Motion Units (IMUs) in a grease ice slick near the shore in Adventfjorden, Svalbard. Viscous attenuation of waves due to the grease ice slick is clearly visible by comparing the IMU data recorded by the different instruments. The frequency dependent spatial damping of the waves is computed by comparing the power spectral density obtained from the different IMUs. We model wave attenuation using the one-layer model of Weber from 1987. The best-fit value for the effective viscosity is $\nu = (0.95 \pm 0.05 \times 10^{-2}) \text{ m}^2 \text{ s}^{-1}$, and the coefficient of determination is $R^2 = 0.89$. The mean absolute error and RMSE of the damping coefficient are 0.037 and 0.044 m^{-1} , respectively. These results provide continued support for improving instrument design for recording wave propagation in ice-covered regions, which is necessary to this area of research as many authors have underlined the need for more field data.

KEYWORDS: frazil ice, ice/ocean interactions, sea ice

1. INTRODUCTION

Understanding the interaction between surface waves and sea ice is an area of ongoing research. Specific applications of eventual successful quantitative results include the formulation of ocean models for climate, weather and sea state prediction (Christensen and Broström, 2008), the estimation of ice thickness (Wadhams and Doble, 2009) and the analysis of pollution dispersion in the Arctic environment (Pfirman and others, 1995; Rigor and Colony, 1997). Surface waves are also part of a feedback mechanism where reduced ice extent leads to increased fetch and, therefore, increased wave height, which in turn results in the break-up of more of the polar sea ice (Thomson and Rogers, 2014).

Several types of ice are found in polar environments, which affect wave propagation in different ways. Ice floe fields exhibit hydrodynamic interaction with the incoming wave field as well as interaction between adjacent floes (Meylan and Squire, 1996). Continuous ice sheets interact with waves by imposing specific pressure and velocity boundary conditions at the water surface, which are related to flexural effects in the ice and lead to wave damping and modifications in the dispersion relation (Liu and Mollo-Christensen, 1988; Squire and others, 1995; Squire, 2007; Sutherland and Rabault, 2016). Grease ice and pancake ice accumulate and form a viscous layer that strongly attenuates surface waves (Weber, 1987; Keller, 1998). These thinner ice types are in their greatest abundance at the ice margins where wave interaction is strongest and ice–wave interactions the least understood. For these reasons, we focus our work here on these ice types along the marginal seas.

To clarify, grease ice is composed of frazil ice crystals, typically disks of size 1–4 mm in diameter and 1–100 μm in thickness (Newyear and Martin, 1997). Grease ice formation has been reported in cold areas where supercooled water is kept from freezing by surface turbulence (Newyear and Martin, 1997; De la Rosa and Maus, 2012). Grease ice accumulates and forms slicks of typical thickness 10–20 cm

(Smedsrød and Skogseth, 2006; Smedsrød, 2011), that effectively damp high-frequency waves, therefore, appearing visually similar to an oil slick (Newyear and Martin, 1997).

The interactions between ice covers and incoming waves have been studied in previous works (Weber, 1987; Squire and others, 1995; Squire, 2007; Sutherland and Rabault, 2016), and several models have been presented. Mass-loading models only take into account the additional inertial effects originating from the presence of the ice and predict a reduction in the wavelength, but do not account for any damping (Peters, 1950). These models are insufficient when describing wave propagation in grease ice (Newyear and Martin, 1997). Similarly, the thin elastic plate model (Greenhill, 1886; Liu and Mollo-Christensen, 1988) describes the influence of flexural rigidity of the ice on wave propagation, which causes an increase of the wavelength but no damping. Such a model was developed to emulate a continuous unbroken ice sheet, but found to be unsuitable for grease ice (Newyear and Martin, 1997). Neither of these models predict wave attenuation, which needs to be described by separate mechanisms. Such mechanisms can be of two kinds: wave scattering, which is especially important in the case of the marginal ice zone (Kohout and Meylan, 2008); and the introduction of an effective viscosity in either the water or the ice layer (Weber, 1987; Keller, 1998; Carolis and Desiderio, 2002). The introduction of viscosity was initially proposed by Weber (1987) and refined by several authors later on (Keller, 1998; Carolis and Desiderio, 2002; Wang and Shen, 2010b). This last class of models is able to successfully reproduce laboratory observations of wave damping by grease ice, considering the effective viscosity as a fitting parameter. Therefore, it is this last class of models that we will examine in this paper.

More explicitly, the one-layer model of Weber (1987) assumes that the viscosity in the upper ice layer is high enough for the momentum equation to be reduced to ‘a

balance between pressure and friction (creeping motion). To explain, the effect of the creeping motion is to 'effectively halt the horizontal motion in the lower fluid at the interface' (Weber, 1987), and the viscous solution of Lamb (1932) is then recovered in the infinitely deep lower layer. An effective eddy viscosity much higher than the molecular viscosity of water is required in the water layer for the model to be consistent with observations and laboratory experiments. This viscous model of wave damping was later extended by Keller (1998), who describes the top layer by means of the incompressible Navier–Stokes equation, while the finite depth lower layer is described by the incompressible Euler equation. The solution in both layers is then obtained by linearizing about the state of rest. This two-layer model is much heavier mathematically than the one-layer model and features two parameters (ice thickness and effective viscosity of the ice layer) if taking the water depth and densities in each layer as given, instead of only one for the one-layer model (effective viscosity).

More recently, Carolis and Desiderio (2002) included an effective viscosity also in the lower layer, therefore introducing a third parameter in the model. The most recent refinement of this class of models was presented by Wang and Shen (2010b), who use a viscoelastic equation to describe the ice layer and model the water below as an inviscid layer. The formulation of Wang and Shen (2010b) went further to include both the flexural and the damping effects of the ice cover in the same model. However, these last models also suffer from a much increased mathematical complexity, which makes them difficult to use in comparisons with field data (Mosig and others, 2015).

Complementary to the numerous modeling efforts mentioned above, laboratory experiments have been performed in parallel to the development of theoretical models. The trends and theoretical curves obtained from the models are presented in the literature and compared with experimental results as a way to assess the quality of each model. However, quantitative metrics are currently not available in the literature to firmly establish the accuracy of any such model, making it difficult to objectively compare the quality of existing published predictions. Initial measurements in grease ice found good qualitative agreement (Newyear and Martin, 1997) with the one-layer model of Weber (1987). The two-layer model was later found to produce better qualitative agreement with experimental data (Newyear and Martin, 1999), but at the cost of more complex mathematics and the need for an additional parameter (ice thickness), as previously explained. The data from both experiments were used also by Carolis and Desiderio (2002) to validate their extended two-layer model with laboratory data. More recently, the effect of a mixed grease–pancake ice field was presented by Wang and Shen (2010a), which led the authors to the introduction of a viscoelastic description of the ice layer. The viscoelastic ice model was finally tested in laboratory experiments involving a variety of mixtures of grease and pancake ice (Zhao and Shen, 2015), and the authors concluded that it did a reasonable qualitative job fitting the observations, given that both equivalent viscosity and shear modulus are fitted using least-squares fits separately for each ice type.

While the development of more sophisticated models is impressive there are some drawbacks to this approach as the corresponding models grow in mathematical complexity

and a greater number of fitting parameters is necessary. These advances are making it possible to obtain better qualitative agreement with laboratory and field results by enriching the underlying mathematics, but in the end the parameters used in all models are determined from empirical fit to experimental data (Wang and Shen, 2010a; Zhao and Shen, 2015). Such an approach only visually improves the quality of the model fits by adding more fitting coefficients, and pinpoints the need for the use of relevant quantitative metrics when comparing models. In addition, the wave modes for the two-layer models are obtained numerically from solving nonlinear dispersion relations, which are satisfied by infinitely many roots. Choosing the right wave mode requires some decision criterion, which proves challenging in the intermediate frequency range in particular when a viscoelastic model is used (Wang and Shen, 2010b; Mosig and others, 2015).

Moreover, articles about wave attenuation by grease ice report a wide range of empirical best-fit effective viscosity values. In their initial article, Newyear and Martin (1997) report frequency-dependent effective viscosity in the water layer using the model of Weber (1987) in the range $\nu_w = 1.35 - 2.22 \times 10^{-2} \text{ m}^2 \text{s}^{-1}$, depending also on the grease ice thickness. In their second article, Newyear and Martin (1999) need to use an effective viscosity for the grease ice layer in the range $\nu_i = 2.5 - 3.0 \times 10^{-2} \text{ m}^2 \text{s}^{-1}$ to describe experimental data with the two-layer model of Keller (1998). According to Carolis and Desiderio (2002), such variability arises from the fact that effective viscosities model both ice properties and other phenomena at the origin of wave damping, including the turbulence-driven dissipation. Carolis and Desiderio (2002) present a summary of eddy viscosities obtained from field measurements, that range from $\nu_f = 1.6 - 2.0 \times 10^{-2} \text{ m}^2 \text{s}^{-1}$ in the Weddell sea, where a high level of turbulence is present, down to $\nu_f = 0.24 \times 10^{-2} \text{ m}^2 \text{s}^{-1}$ in the central Arctic Ocean where much less turbulent conditions are observed. This high variability in eddy viscosity, and therefore in wave damping and effective viscosity, has also been observed for the same geographic region over just a few days (Doble and others, 2015). Attempts to provide theoretical justifications for the value of the effective viscosity needed to reproduce the damping observed in experiments have been presented (De Carolis and others, 2005), but cannot yet replace empirical fit to experimental data.

The diversity of models and parameter values discussed in the previous paragraphs makes it challenging to get a clear understanding of the situation. Two main questions arise in this context. First is the issue of how representative of the field conditions the different studies presented are. There is variability in the damping for waves in ice, and probably several different damping regimes are possible in the ocean. Therefore, characterizing the conditions in which each damping regime is observed is important. This will only be possible through the collection of much larger volumes of field data than have been discussed up to now (Mosig and others, 2015). While the number of articles that have been published could suggest that much data are available, articles discussing field data often rely on relatively small datasets and the data available on the whole are very scarce compared with the spatial extent of polar regions and diversity of regimes observed. Therefore, a first possible approach for clarifying the situation would be to collect

much more field data. This in turn puts a sharp constraint on the acceptable cost of each measurement. We propose a possible solution for this issue, namely the use of instruments based on off-the-shelf sensors and open-source electronics as a way to reduce costs and increase measurement flexibility.

The second issue is to decide, confronted by the diversity of models presented in the literature, how the appropriate level of model complexity should be selected. Articles published so far have mostly introduced new and ever more complex models, fitted their parameters to a dataset and presented curves offering a visual impression of the quality of the fit. However, going further into determining which model to use should rely on some quantitative metrics that describe the statistical quality of each model. We address this issue by using several of the simplest model-fitting quality estimators, namely the coefficient of determination (Rao, 1973), usually noted R^2 , and the mean absolute error (MAE) and RMSE. R^2 is a number between 0 and 1 that indicates the part of the variance in the data that are explained by the model, so that an R^2 value of 1 indicates that the model fully describes the variance in the data, while an R^2 value of 0 indicates that the model fails in explaining anything of the data presented. The MAE and RMSE are other well-established metrics that can be used to quantify the quality of a model (Willmott, 1982; Chai and Draxler, 2014), and that directly measure the discrepancy between model predictions and experimental data.

The organization of the paper is as follows. We first describe the architecture of the instruments used for the measurements. Next we present the data obtained and the methodology used to compare it with the one-layer model used by Weber (1987) and Newyear and Martin (1997). Finally, we present our results and discuss the agreement between our data and the one-layer model, as well as with the laboratory experiment of Newyear and Martin (1997), regarding the value of the effective viscosity observed.

2. INSTRUMENTATION

The harsh Arctic environment sets demanding requirements for scientific observations. While several commercial solutions are available (companies selling instruments operating in the Arctic include, e.g. Sea Bird Scientific Co., Campbell Scientific Co., Aanderaa Data Instruments A.S.), these usually come at high cost and have reduced flexibility. By contrast, off-the shelf sensors and open-source electronics are now sufficiently evolved, well documented and easy to use that they become a credible alternative to traditional solutions. The specificity of open-source software and electronics is that their source code, internal designs and interfaces are made available through a license that provides the right to study, modify and distribute the product (Joshua, 2014). This has many valuable implications for the scientific community. In particular, sharing all the details of the design of an instrument can make it easier to reproduce experiments, by drastically reducing the cost and time necessary to build an exact copy of the instrument initially used. In addition, this makes it easier to build upon a common platform, therefore encouraging modularity and reuse of previous designs rather than fragmented in-house development, which very likely is redundant between research groups and private suppliers, leading to unnecessary costs.

In the present case, we can choose a sensor with the characteristics required for performing measurements in the Arctic (including thermal calibration between -40 and $+85^\circ\text{C}$), while reducing sharply the cost of each logger. Our approach consists in selecting the most cost-effective off-the-shelf sensor able to perform the measurements we need, and to build the whole logger around it using only open-source electronics and software. In our experience, common electronics components which rely on integrated circuits, flash memory and other semiconductors work in a wide range of temperature and, unlike batteries and sensors, do not present major problems in cold environments. Other groups in oceanography have started using open-source solutions, and the use of open-source electronics has been increasingly reported in the literature in the last few years (Baker, 2014; Gandra and others, 2015; Cauzzi and others, 2016). However, the solutions presented so far lack the generality, robustness and flexibility that will make them easily adaptable to a wide variety of projects. There is, therefore, a need for more groups to start sharing their designs together with detailed documentation, which would help to gather momentum around the use of open-source solutions in ocean research and create an open-source ecosystem similar to what has been achieved with, for example, scientific libraries around the Python language. In summary, transition toward at least partially open-source instrumentation can lead to a drastic reduction in price and development time for all groups working with field measurements, while at the same time making reproducibility of experiments by peers easier.

The data obtained in the present study were collected using an off-the-shelf sensor and an open-source logging system, which was created with generality and ease of modification in mind. The logger is based on a microcontroller rather than a traditional computer. This allows reduced price, power consumption and complexity. In addition an open-source GPS chip and SD card reader are integrated in the logger for absolute time reference, position information and data storage capability. Any type of sensor can then be added to build an instrument in a modular fashion.

The sensor model used to measure waves is the rugged, thermally calibrated VN100 Inertial Motion Unit (IMU) manufactured by Vectornav Co. This IMU was already assessed and used to produce valuable data in the field (Sutherland and Rabault, 2016). The VN100 is configured to output magnetic vector, linear accelerations, angular rates, temperature, pressure and checksum in ASCII format at 10 Hz.

The IMUs and additional electronics were enclosed in hard plastic cases, to which a float was attached for ensuring that the whole system follows the waves well. More details about the technical solutions used for building the wave sensors are given in the Appendix.

3. OBSERVATIONS

Three instruments were deployed at sea near Longearbyen, Svalbard on 17 March 2016. A small boat was used to access the edge of a grease ice slick near shore to deploy the instruments. The water in the measurement area is shallow, down to ~ 80 cm at the point closest to the shore. Wind waves generated locally came approximately perpendicular to the shore, and approximately parallel to a seawall limiting the extend of the grease ice slick to the East. The influence of the seawall on the waves recorded by the

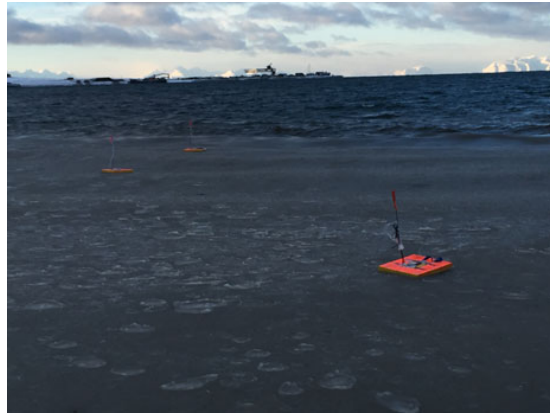


Fig. 1. Sensors F1, F2, F3 (by order of increasing distance from the camera) deployed near shore in a grease ice slick near Longyearbyen, Svalbard.

sensors was negligible. To allow easy recovery, the instruments were tied together with a rope, so that the maximum distance allowed between two instruments tied together was ~ 15 m. The total 30 m rope length used was long enough to not influence the dynamics of the floats and the maximum distance effectively measured between two instruments tied together is ~ 8 m, which indicates that there was no tension on the rope when measurements are performed. A picture of the ice slick and floats is presented in Figure 1. As visible in Figure 1, the instrument F1 entered the grease ice slick, while instruments F2 and F3 remained close to each other, at the limit of the slick during most of the measurement. The position of the instruments, obtained from the recorded GPS data, is presented in Figure 2. In all the following, the instruments are referred to as F1, F2 and F3. After ~ 1

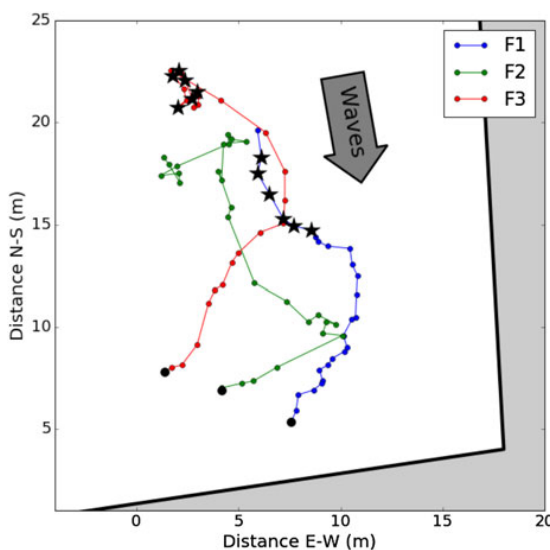


Fig. 2. Tracks of the wave sensors F1, F2 and F3 as recorded by their on-board GPS during the whole time of the measurements (UTC 14.10–16.30). Shore is indicated by the gray area. The positions of instruments F1 and F3 at the times of the beginning of each data sample used for computing wave attenuation by grease ice are marked with black stars. The final position of each instrument is indicated by a black dot.

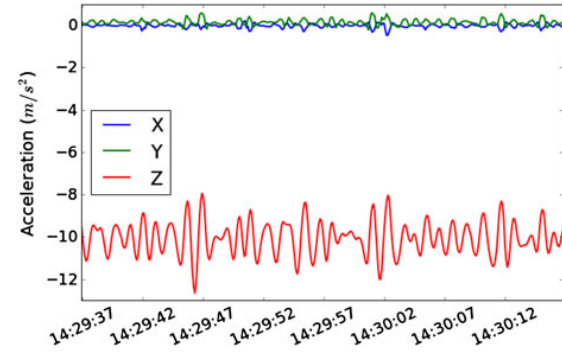


Fig. 3. Sample of the raw data for linear acceleration logged by the sensor F3. The time indicated is UTC on 17 March 2016. Data labeled Z correspond to the IMU axes pointing upwards, while data labeled X and Y correspond to the two IMU axes in the horizontal plane.

h of drifting, F1 got grounded on shore and the wave data obtained by F1 are therefore not reliable after 15.05 UTC.

A sample of the raw data corresponding to the linear accelerations recorded by the instrument F3 is presented in Figure 3. The factory-rated accuracy of the linear acceleration expected from the VN100 is 5×10^{-3} g, with $g = 9.81 \text{ m s}^{-2}$ the acceleration of gravity, which is ~ 2.5 orders of magnitude better than the typical vertical accelerations corresponding to the waves encountered during our measurements in grease ice. Therefore, as visible in Figure 3, the IMU is able to smoothly resolve the wave signal. The measured accelerations are primarily in the vertical direction (Z-axes of the IMU), while only small residual horizontal accelerations are observed (X- and Y-axes of the IMU). This was also observed visually during the deployment of the sensors, with the instruments appearing to be effectively stuck in the horizontal direction relatively to incoming waves due to the viscous grease ice layer.

The 10 Hz sampling frequency is well above the highest wave frequency observed, which is ~ 1.2 Hz. Therefore, the signal is effectively over sampled with respect to the Nyquist criterion in terms of water wave frequencies observed. While we record wave signal at 10 Hz, the IMU works internally at 800 Hz, so that the signal obtained is the result of a low-pass filtering done by the IMU processor and therefore eliminates otherwise possible aliasing of wind induced high-frequency accelerations.

4. METHODOLOGY

When computing the wave elevation power spectral density (PSD), the true vertical direction aligned with gravity is first determined by averaging the acceleration over the whole time series for each sensor. The maximum deviation compared with the Z-direction of the IMUs fixed inside the instrument cases is $< 5^\circ$. The vertical wave acceleration is then obtained for each instrument by projecting the linear acceleration recorded by the IMU on the true vertical acceleration. We tested the effect of the angular deviation by adding to the vertical data an artificial random deviation of similar magnitude as the one experimentally measured, and processing the altered signal in the same way as presented in this section. We could not observe any significant influence on the results, as reported in the next section. The PSD of the

wave vertical acceleration is computed with the Welch method (Earle, 1996) on 20-min intervals, using three time windows with 50% overlap, and low-pass filtered using a sliding average filter of width eight points. Error bars for the Welch spectra are computed using the Chi-squared (χ^2) error estimate. The PSD for the wave elevation is finally computed from the PSD of the wave vertical acceleration using the formula from Tucker and Pitt (2001):

$$\text{PSD}[\eta] = \omega^{-4} \text{PSD}[\eta_{tt}], \quad (1)$$

where $\omega = 2\pi f$ is the angular frequency, f the frequency, η the wave elevation and η_{tt} the vertical acceleration recorded by the IMU.

Since the PSD is quadratic in the wave amplitude, we can write the attenuation coefficient for the wave amplitude between F_i and F_j at each frequency, a_{ij} , as:

$$a_{ij}(f) = \sqrt{\frac{\text{PSD}_i(f)}{\text{PSD}_j(f)}}, \quad (2)$$

where PSD_i is the PSD corresponding to the floating instrument F_i . The direction of the incoming waves, which is approximately perpendicular to the coast line, is at an angle 10° west of north. The projection of the distance d_{ij} between instruments F_i and F_j on the wave propagation direction is therefore computed as:

$$d_{ij} = \mathbf{D}_{10} \cdot \mathbf{r}_{ij}, \quad (3)$$

with \mathbf{D}_{10} the wave propagation direction, and \mathbf{r}_{ij} the position vector from F_i to F_j , computed from the GPS data recorded by the instruments.

The wave damping coefficient $\alpha(f)$ is defined for an incoming monochromatic wave of frequency f as:

$$A_f(x) = A_f(0)e^{-\alpha(f)x}, \quad (4)$$

with $A_f(x)$ the monochromatic wave amplitude at a distance x along the wave direction of propagation, and $x = 0$ is an arbitrary reference position. The damping coefficient α is therefore computed from the attenuation coefficient and the projected distance between F_i and F_j as:

$$\alpha(f) = -\frac{\log(a_{ij}(f))}{d_{ij}}. \quad (5)$$

As emphasized in the introduction, several theoretical models describing wave attenuation by an ice cover have been proposed in the literature. While ice conditions can be controlled in laboratory experiments and grease ice thickness and effective viscosity can be measured and used as parameters in a two-layer model, it was not possible to measure those parameters during our field measurements. We could arbitrarily pick up a value for the grease ice layer thickness corresponding to a typical grease ice slick, and use this with one of the more sophisticated two-layer models. However, there would then be no advantage over the simpler one-layer models as the point of two-layer models is to account explicitly for the properties of the ice layer that are otherwise hidden in the value of the effective viscosity. This conflicts with the use of default values for the ice layer properties. Indeed, if default values for the ice layer properties are used based on a coarse assessment of

the field conditions, all the fitting of the two-layer models is done based on the value of the effective viscosity of the ice or water layer, similarly to a one-layer model. Therefore, we compare our results with the one-layer model of Weber (1987), which has proven to yield satisfactory agreement with long waves at sea (Weber, 1987) and short waves in the laboratory (Newyear and Martin, 1997). The wave solution described by the one-layer model is the deep water limit of the more general viscous wave damping solution described by Lamb (1932). The generic equation describing the damping rate for any water depth, α_g , is (Lamb, 1932):

$$\alpha_g(f) = \frac{\nu k}{2c_g \delta}, \quad (6)$$

with ν the viscosity that in the original derivation is the viscosity of the fluid, but that can be replaced by an effective eddy viscosity in the water layer ν_w to model field data, k the wavenumber, $c_g = \partial\omega/\partial k$ the group velocity, and $\delta = \sqrt{2\nu/\omega}$ the thickness of the Stokes layer.

The one-layer model is obtained by substituting the deep water linear dispersion relation, $\omega^2 = gk$ with $g = 9.81 \text{ m}^2 \text{ s}^{-1}$ the acceleration of gravity, in Eqn (6). The expression for the damping rate using an effective viscosity in the water layer is then (Weber, 1987):

$$\alpha(f) = \frac{\nu_w^{1/2} \omega^{7/2}}{\sqrt{2g^2}}. \quad (7)$$

Dissipation at the sea bottom is neglected in this model, which is justified as long as viscous dissipation due to the grease ice layer is the dominant dissipation mechanism. This hypothesis can be checked a posteriori. A formula describing the damping effect of the bottom and side wall boundary layers in a wave tank is provided by Sutherland and others (2017) as:

$$\alpha_{bs} = \nu \gamma k \frac{[(1/\sinh(2kH)) + (1/kB)]}{c_g}, \quad (8)$$

where $\gamma = 1/\delta$, H is the water depth, B is the width of the wave tank and ν is the viscosity of water. In our case with sea water at 0° Celsius $\nu = 1.83 \times 10^{-6} \text{ m}^2 \text{ s}^{-1}$. In the open sea, if one assumes that the seabed is smooth enough that the boundary layer there is similar to what is expected in a wave tank, only the first term in Eqn (8) will contribute since no side walls are present. The effect of the boundary layers on wave damping on both the experiment of Newyear and Martin (1997) and our field measurements will be analyzed in the Discussion section.

5. RESULTS

Figure 4 shows samples of the observed PSDs. The waves recorded are locally generated wind waves, with a peak frequency $\sim 0.8 \text{ Hz}$ during the whole record. The damping effect of the grease ice slick is clearly visible. While instruments F2 and F3 remain close to each other at the limit of the grease ice slick and present little damping in most of the spectra, the instrument F1 that moved into the grease ice shows clear reduction in the wave PSD, especially at high frequencies as is expected from theory (Weber, 1987; Keller, 1998). However, F1 drifts to shallow areas as time

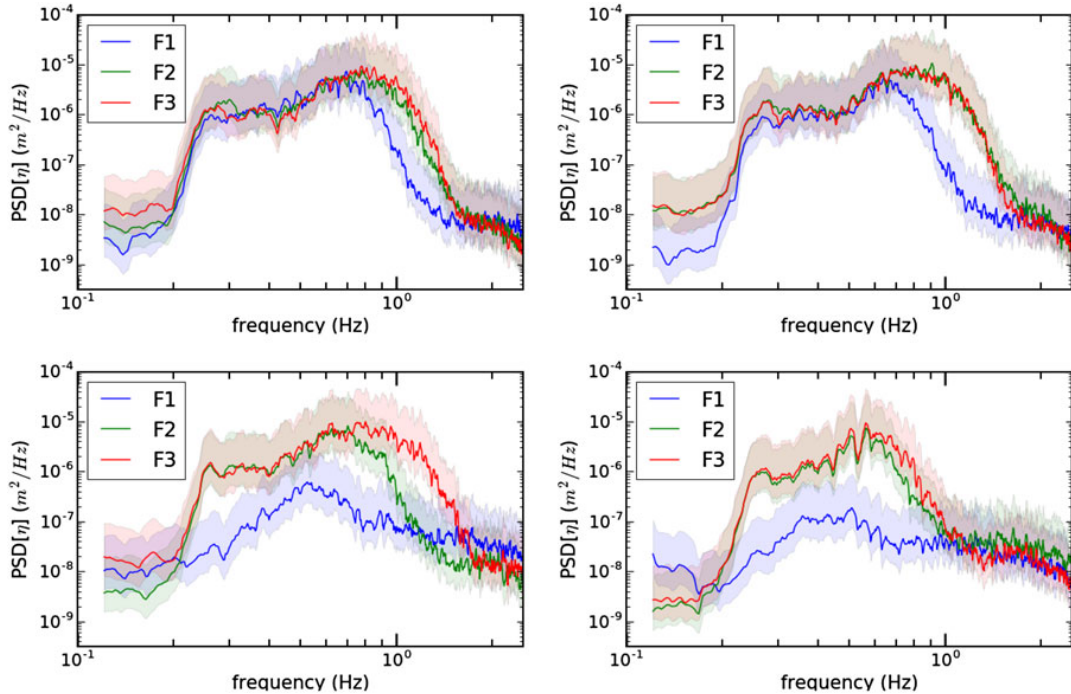


Fig. 4. Evolution with time of the PSD for wave elevation recorded by the sensors F1, F2 and F3 computed using the Welch method on 20-min intervals, using three time windows and 50% overlap followed by a sliding average filter. From left to right, top to bottom, the UTC time obtained from the internal GPS for the beginning of the time series used is 14.15, 14.25, 15.05, 15.25.

goes on and was grounded when recovered. This explains the excessive attenuation observed for times 15.05 and 15.25 UTC, and the corresponding PSD obtained from F1 should not be trusted.

During the time interval between 14.15 and 15.00 UTC, F1 is about 7 m further in the grease ice slick compared with F3, so that reliable wave damping coefficients can be computed. The location of the instruments during this time window is presented in Figure 2. During this time interval we can compute the damping based on the PSD for F1 and F3.

The value of the effective viscosity in the water layer yielding best agreement between Eqn (7) and laboratory experiments of Newyear and Martin (1997) is of the order of $(1.35 \pm 0.08 \times 10^{-2}) \text{ m}^2 \text{s}^{-1}$ at 1.173 Hz for a 11.3 cm grease ice layer thickness (Table 1 of Newyear and Martin (1997)). Using the same model Eqn (7), we compute the best-fit

effective viscosity using nonlinear least-squares fit on the attenuation rate obtained through Eqn (5) for the collection of signal sample start times 14.20, 14.25, 14.30, 14.35, 14.40 and 14.45 UTC. We find a value $v_w = (0.95 \pm 0.05 \times 10^{-2}) \text{ m}^2 \text{s}^{-1}$ using a 5- σ confidence interval for the viscosity spread, which corresponds to a relative difference to the value found in previous cold laboratory experiments of $(30 \pm 10\%)$. Propagating the angular deviation of the true vertical signal leads to relative variations in v_w of $<1\%$. We also compute the coefficient of determination of our model on the field data and obtain a value of $R^2 = 0.89$. Finally, we compute the value of the MAE and RMSE relative to the prediction of the attenuation parameter, which are 0.037 and 0.044 m^{-1} , respectively. Results are summarized in Table 1.

6. DISCUSSION

Obtaining a closed form wave damping formula from Eqn (6) requires the use of the deep water dispersion relation, as the more general intermediate water depth dispersion relation is not invertible in terms of exact known functions. However, the deep water approximation, which is already not strictly enforced in the laboratory study by Newyear and Martin (1997), is not strictly justified at the lower frequencies we report here. Therefore, we also compare the damping obtained in the field with Eqn (6), using the same effective viscosity in the water layer $v_w = 0.95 \times 10^{-2} \text{ m}^2 \text{s}^{-1}$ and the intermediate water depth dispersion relation:

$$\omega^2 = gk \tanh(kH), \quad (9)$$

where $H = 0.8 \text{ m}$ is the water depth. Newyear and Martin (1997, 1999) showed that the effect of the grease ice layer

Table 1. Comparison between the results obtained by Newyear and Martin (1997) in the laboratory and our field measurements in Svalbard

	Experiments by Newyear and Martin (1997)	Field measurements in Svalbard
Frequency domain (Hz)	1.173	0.35–1.1
Best-fit effective viscosity ($\text{m}^2 \text{s}^{-1}$)	$1.35 \pm 0.08 \times 10^{-2}$	$0.95 \pm 0.05 \times 10^{-2}$
R^2	N/A	0.89
MAE (m^{-1})	N/A	0.037
RMSE (m^{-1})	N/A	0.044

R^2 , MAE and RMSE are computed based on the attenuation coefficient. We include only the measurement by Newyear and Martin (1997) at the frequency closest to the frequency range observed in the field.

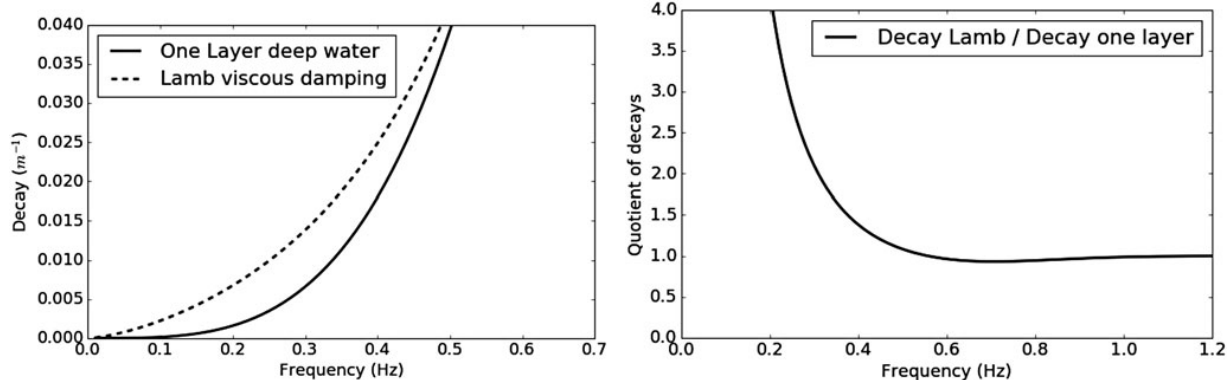


Fig. 5. Illustration of the effect of the choice of the deep or intermediate water depth dispersion relation on the wave attenuation obtained from Eqn (6). One layer label indicates that the formula from Weber (1987) which relies on the deep water dispersion relation is used, while Lamb label indicates that the intermediate water depth dispersion relation is used. Left: comparison of the attenuation curves for low frequencies. Right: quotient of both attenuation curves.

on the real part of the dispersion relation, i.e. changes in the wavelength introduced by the grease ice layer, can be neglected up to ~ 1.2 Hz, which is over the higher frequency limit for which we are able to compute damping. Therefore, we can use Eqn (9) to compute wavelength and group velocity even in the presence of a grease ice layer.

In the limit of low-frequency waves, the difference between the deep and intermediate water depth dispersion relations becomes important. As shown in Figure 5(a), both dispersion relations lead together with Eqn (6) to a zero attenuation in the low-frequency limit. However, the predicted quotient of the two attenuation curves goes to infinity in the low-frequency limit as shown in Figure 5(b), indicating that the velocity at which convergence to zero happens is very different between the two curves. As can be seen in Figure 5(b), the damping predicted by both dispersion relations is similar down to a frequency of ~ 0.4 Hz, which is slightly above the minimum frequency measured in the field, before diverging sharply. However, the damping in the frequency domain below 0.4 Hz for which both dispersion relations yield significantly different predictions is much smaller than for higher frequencies, and therefore the absolute difference between both predictions has a small impact on the least-squares fit used for obtaining the effective viscosity.

Results of the damping values obtained from the field measurements, compared with the one-layer model using the fitted effective viscosity value, are presented in Figure 6. The thin lines indicate damping obtained from Eqn (5) for the six signal samples equally spaced in time, with start times between 14.20 and 14.45 UTC, that were used to fit the effective viscosity. The gray area indicates the 3σ confidence interval based on all the damping curves. The thick black line indicates the one-layer model prediction from Eqn (7) obtained with the effective viscosity value previously reported, and the dashed line the intermediate water depth prediction from Eqn (6) using the same viscosity. Observations of wave attenuation in the field are therefore consistent with both the one-layer model of Weber (1987) and previous experiments in the laboratory.

We find good agreement, both qualitatively and quantitatively, between the one-layer model and the field data as shown by the width of the confidence intervals obtained, the value of the R^2 coefficient and the visual inspection of

Figure 6. By contrast, we obtain a bigger discrepancy between the effective viscosity computed from our measurements and obtained by Newyear and Martin (1997). Several explanations can be attempted to explain the corresponding ($30 \pm 10\%$) discrepancy. Firstly, the effective viscosity reported by Newyear and Martin (1997) increases slightly with frequency, which they attribute to a possible non-Newtonian behavior of the ice layer, so that reproducing their experiment for a lower frequency range corresponding to the field data obtained may yield better agreement. Secondly, as was emphasized in the introduction, the literature does report intrinsic variability in the effective viscosity due to, among other things, the thickness of the grease ice layer or the level of turbulence in the water. Those variables are difficult to measure in the field, and would be challenging to obtain from remote sensing and include in a wave model, therefore not testable at this time. As a consequence it is satisfactory to find that the one-layer model, which models all

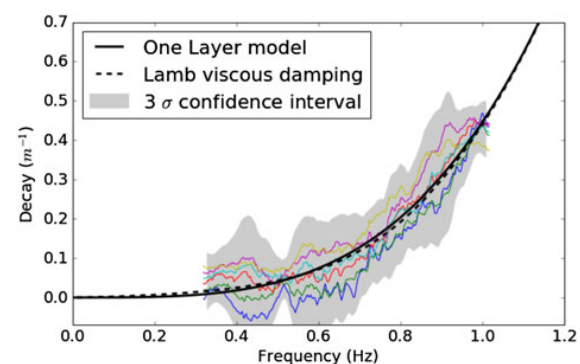


Fig. 6. Comparison of the observed damping rate from experimental data with the one-layer model. The thin curves show the frequency-dependent damping rate obtained by comparing the PSD for wave elevation obtained from sensors F1 and F3 for six equally spaced data samples with start times between 14.20 and 14.45 UTC. The gray area is the corresponding 3σ confidence interval. The thick line is the prediction of the one-layer model, with an effective viscosity in the water layer $\nu_w = 0.95 \times 10^{-2} m^2 s^{-1}$. The dashed line is the prediction of the more general Lamb viscous damping solution, computed for the same effective viscosity as the one-layer model using the intermediate water depth dispersion relation.

those effects in one single parameter (the effective viscosity), manages to produce similar results between field measurement and laboratory experiments, at least for the present small-scale study.

Another cause of discrepancy between our field measurements and laboratory results could be friction on the wave tank side walls. As explained previously, it is well known that the effects of the boundary layers on a wave tank side and bottom walls can affect wave damping, and must be accounted for to accurately compare laboratory results with theories (Sutherland and others, 2017). We can therefore use Eqn (8), together with the intermediate water depth dispersion relation (9), to estimate the effect of the seabed boundary layer on the measurements we performed in Svalbard, and of both the wave tank bottom and side walls in the case of the experiment by Newyear and Martin (1997). We use the viscosity of water at 0°C when computing the effect of the boundary layers. Results are presented in Figure 7. The effect of the seabed (or bottom wall) on wave decay has a peak at an intermediate frequency that depends on the water depth, and diminishes for higher frequency waves as wave motion gets concentrated near the surface. By contrast, the effect of the side walls increases with higher frequencies.

A comparison between the results presented in Figures 6 and 7 shows that the effect of the seabed on wave damping is about three orders of magnitude smaller than the effect of the grease ice at 0.6 Hz. Therefore, even considering that the seabed roughness may increase the damping effect on the field data, the effect of the seabed boundary layer on wave decay can be neglected. In the case of the experiments by Newyear and Martin (1997), Figure 7 shows that while the effect of the side walls increases at higher frequencies, it is there also about two orders of magnitude smaller than the decay coefficient reported in their Table 1. However, the presence of ice at the water surface could

add another source of friction on the wave tank walls, which is not accounted for here. Unfortunately, we would need to perform a direct measurement of the friction coefficient of the grease ice on the material used for building the walls of the wave tank used by Newyear and Martin (1997) to assess the magnitude of this effect.

7. CONCLUSIONS

In the present paper, wave sensors are deployed in a grease ice slick near the shore in Svalbard and successfully measure wave spectra and wave attenuation by the grease ice. We present a comparison with the one-layer model of Weber (1987) in the frequency range 0.4–1 Hz. The value of the effective viscosity in the water layer giving the best fit to the experimental data is $\nu_w = (0.95 \pm 0.05 \times 10^{-2}) \text{ m}^2 \text{s}^{-1}$, which is $(30 \pm 10\%)$ less than the value found at slightly higher frequency in previous cold laboratory experiments. We discuss the possible origin of this discrepancy, and cannot find any significant effect of the boundary layers developing on the wave tank walls and bottom. Therefore, we expect that the discrepancy arises from variability in the grease ice properties and the slightly lower frequency observed in the field compared with the laboratory.

In addition to the value of the effective viscosity, we obtain a coefficient of determination $R^2 = 0.89$, and values for the MAE and RMSE relative to the prediction of the attenuation parameter of 0.037 and 0.044 m^{-1} , respectively. This proves that, in realistic conditions corresponding to field data where only partial information is available, so that sophisticated two-layer models could not be applied, the simpler one-layer model can still provide valuable information about wave damping. Using quantitative metrics such as the coefficient of determination, the MAE and RMSE could be a method to objectively compare different models for wave attenuation by grease ice.

The need for more field measurements for wave attenuation by ice has been underlined previously in the literature (Mosig and others, 2015). In this context, the instruments used for performing this work may also be of interest for other groups. Indeed, we built instruments that are versatile and based on off-the-shelf sensors and open-source electronics, which could make experiments both cheaper and easier to replicate by peers. Code and hardware details are shared as open-source material on the Github of the corresponding author (more details in the Appendix). It is hoped that such an open-source policy can become the norm for field measurements.

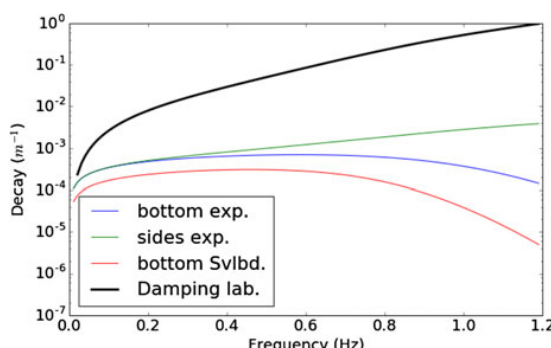


Fig. 7. Wave damping arising from the bottom and side walls in the experiment by Newyear and Martin (1997) (bottom exp. and sides exp. curves, respectively), along with the effect of the seabed boundary layer on the measurements we report in Svalbard (curve bottom Svlbd.). Decays are computed using Eqn (8) together with the intermediate depth dispersion relation Eqn (9) and the viscosity of water at 0°C. According to the information provided by Newyear and Martin (1997), we use a water depth $H = 0.5 \text{ m}$ and a wave tank width $B = 1 \text{ m}$ in the laboratory data case. The water depth used in the field data case is $H = 0.8 \text{ m}$. The damping predicted by the one-layer model using the effective viscosity found by Newyear and Martin (1997) together with the dispersion relation for waves in intermediate water depth is presented for comparison (curve Damping laboratory).

ACKNOWLEDGMENTS

The help of Aleksey Marchenko during the field work is gratefully acknowledged. The work was funded through the project ‘Experiments on Waves in oil and ice’ (Petromaks 2, Grant 233901). The authors want to thank two anonymous reviewers whose feedback greatly improved the initial manuscript. More information about the loggers can be found in the Appendix or on the Github of the first author (<https://github.com/jerabaul29/LoggerWavesInIce>).

REFERENCES

- Baker E (2014) Open source data logger for low-cost environmental monitoring. *Biodivers. Data J.*, **2**, e1059 (doi: 10.3897/BDJ.2.e1059)

- Carolis GD and Desiderio D (2002) Dispersion and attenuation of gravity waves in ice: a two-layer viscous fluid model with experimental data validation. *Phys. Lett. A*, **305**(6), 399–412 (doi: [http://dx.doi.org/10.1016/S0375-9601\(02\)01503-7](http://dx.doi.org/10.1016/S0375-9601(02)01503-7))
- Cauzzi C and 5 others (2016) An open-source earthquake early warning display. *Seismol. Res. Lett.*, **87** (doi: 10.1785/0220150284)
- Chai T and Draxler RR (2014) Root mean square error (RMSE) or mean absolute error (MAE)? Arguments against avoiding RMSE in the literature. *Geosci. Model Dev.*, **7**(3), 1247–1250 (doi: 10.5194/gmd-7-1247-2014)
- Chang M and Bonnet P (2010) Monitoring in a high-arctic environment: some lessons from MANA. *IEEE Pervasive Comput.*, **9**(4), 16–23 (doi: <http://doi.ieeecomputersociety.org/10.1109/MPRV.2010.53>)
- Christensen K and Broström G (2008) *Waves in sea ice*. Technical Report, Norwegian Meteorological Institute, Oslo
- De Carolis G, Olla P and Pignagnoli L (2005) Effective viscosity of grease ice in linearized gravity waves. *J. Fluid Mech.*, **535**, 369–381 (doi: 10.1017/S002211200500474X)
- De la Rosa S and Maus S (2012) Laboratory study of frazil ice accumulation under wave conditions. *Cryosphere*, **6**(1), 173–191 (doi: 10.5194/tc-6-173-2012)
- Doble MJ, De Carolis G, Meylan MH, Bidlot JR and Wadhams P (2015) Relating wave attenuation to pancake ice thickness, using field measurements and model results. *Geophys. Res. Lett.*, **42**(11), 4473–4481 (doi: 10.1002/2015GL063628), 2015GL063628
- Earle MD (1996) Nondirectional and directional wave data analysis procedures. DBC Tech. Doc 96-01, National Data Buoy Centre, National Oceanic and Atmospheric Administration, U.S. Department of Commerce, Washington, DC.
- Gandra M, Seabra R and Lima FP (2015) A low-cost, versatile data logging system for ecological applications. *Limnol. Oceanogr.: Methods*, **13**(3), 115–126 (doi: 10.1002/lom3.10012), e10012
- Greenhill AG (1886) Wave motion in hydrodynamics. *Am. J. Math.*, **9**(1), 62–96
- Joshua MP (2014) *Open-Source Laboratory*, Elsevier, Amsterdam
- Keller JB (1998) Gravity waves on ice-covered water. *J. Geophys. Res.*, **103**, 7663–7669 (doi: 10.1029/97JC02966)
- Kohout AL and Meylan MH (2008) An elastic plate model for wave attenuation and ice floe breaking in the marginal ice zone. *J. Geophys. Res.: Oceans*, **113**(C9), n/a–n/a (doi: 10.1029/2007JC004434), c09016
- Lamb H (1932) *Hydrodynamics*. Cambridge Mathematical Library, Cambridge University Press, Cambridge
- Liu AK and Mollo-Christensen E (1988) Wave propagation in a solid ice pack. *J. Phys. Oceanogr.*, **18**(11), 1702–1712 (doi: 10.1175/1520-0485)
- Meylan MH and Squire VA (1996) Response of a circular ice floe to ocean waves. *J. Geophys. Res.: Oceans*, **101**(C4), 8869–8884 (doi: 10.1029/95JC03706)
- Mosig JEM, Montiel F and Squire VA (2015) Comparison of visco-elastic-type models for ocean wave attenuation in icecovered seas. *J. Geophys. Res.: Oceans*, **120**(9), 6072–6090 (doi: 10.1002/2015JC010881)
- Newyear K and Martin S (1997) A comparison of theory and laboratory measurements of wave propagation and attenuation in grease ice. *J. Geophys. Res.: Oceans*, **102**(C11), 25091–25099 (doi: 10.1029/97JC02091)
- Newyear K and Martin S (1999) Comparison of laboratory data with a viscous two-layer model of wave propagation in grease ice. *J. Geophys. Res.: Oceans*, **104**(C4), 7837–7840 (doi: 10.1029/1999JC000002)
- Peters AS (1950) The effect of a floating mat on water waves. *Commun. Pure Appl. Math.*, **3**(4), 319–354 (doi: 10.1002/cpa.3160030402)
- Pfirman S, Eicken H, Bauch D and Weeks W (1995) The potential transport of pollutants by arctic sea ice. *Sci. Total Environ.*, **159** (23), 129–146 (doi: [http://dx.doi.org/10.1016/0048-9697\(95\)04174-Y](http://dx.doi.org/10.1016/0048-9697(95)04174-Y))
- Rao CR (1973) *Linear statistical inference and its applications*. Wiley, New York (doi: 10.1002/9780470316436)
- Rigor I and Colony R (1997) Sea-ice production and transport of pollutants in the laptev sea, 19791993. *Sci. Total Environ.*, **202**(13), 89–110 (doi: [http://dx.doi.org/10.1016/S0048-9697\(97\)00107-1](http://dx.doi.org/10.1016/S0048-9697(97)00107-1)), environmental Radioactivity in the Arctic
- Smedsrød LH (2011) Grease-ice thickness parameterization. *Ann. Glaciol.*, **52**, 77–82 (doi: 10.3189/172756411795931840)
- Smedsrød LH and Skogseth R (2006) Field measurements of arctic grease ice properties and processes. *Cold Regions Sci. Technol.*, **44**(3), 171–183 (doi: <http://dx.doi.org/10.1016/j.col-regions.2005.11.002>)
- Squire V (2007) Of ocean waves and sea-ice revisited. *Cold Regions Sci. Technol.*, **49**(2), 110–133 (doi: <http://dx.doi.org/10.1016/j.col-regions.2007.04.007>)
- Squire V, Dugan JP, Wadhams P, Rottier PJ and Ilu AK (1995) Of ocean waves and sea-ice. *Annu. Rev. Fluid Mech.*, **27**, 115–168 (doi: <http://dx.doi.org/10.1146/annurev..27.010195.000555>)
- Sutherland G and Rabault J (2016) Observations of wave dispersion and attenuation in landfast ice. *J. Geophys. Res.: Oceans*, **121**(3), 1984–1997 (doi: 10.1002/2015JC011446)
- Sutherland G, Halsne T, Rabault J and Jensen A (2017) The attenuation of monochromatic surface waves due to the presence of an inextensible cover. *Wave Motion*, **68**, 88–96 (doi: <http://dx.doi.org/10.1016/j.wavemoti.2016.09.004>)
- Thomson J and Rogers WE (2014) Swell and sea in the emerging arctic ocean. *Geophys. Res. Lett.*, **41**(9), 3136–3140 (doi: 10.1002/2014GL059983)
- Tucker M and Pitt E (2001) *Waves in ocean engineering. Elsevier ocean engineering book series*, Elsevier, University of Michigan
- Wadhams P and Doble MJ (2009) Sea ice thickness measurement using episodic infragravity waves from distant storms. *Cold Regions Sci. Technol.*, **56**(23), 98–101 (doi: <http://dx.doi.org/10.1016/j.col-regions.2008.12.002>)
- Wang R and Shen HH (2010a) Experimental study on surface wave propagating through a greasepancake ice mixture. *Cold Regions Sci. Technol.*, **61**(23), 90–96 (doi: <http://dx.doi.org/10.1016/j.col-regions.2010.01.011>)
- Wang R and Shen HH (2010b) Gravity waves propagating into an ice-covered ocean: a viscoelastic model. *J. Geophys. Res.: Oceans*, **115**(C6), n/a–n/a (doi: 10.1029/2009JC005591), c06024
- Weber JE (1987) Wave attenuation and wave drift in the marginal ice zone. *J. Phys. Oceanogr.*, **17**(12), 2351–2361 (doi: 10.1175/1520-0485(1987)017<2351:WAAWDI>2.0.CO;2)
- Willmott CJ (1982) Some comments on the evaluation of model performance. *Bull. Am. Meteorol. Soc.*, **63**(11), 1309–1313 (doi: 10.1175/1520-0477(1982)063<1309:SCOTEO>2.0.CO;2)
- Zhao X and Shen HH (2015) Wave propagation in frazil/pancake, pancake, and fragmented ice covers. *Cold Regions Sci. Technol.*, **113**, 71–80 (doi: <http://dx.doi.org/10.1016/j.col-regions.2015.02.007>)

APPENDIX

TECHNICAL DETAILS ABOUT THE INSTRUMENTS USED

The general architecture of the instruments is the following. An Arduino Mega microcontroller board is used together with a GPS chip, an active GPS antenna, and an SD card reader to build a modular instrument. The GPS chip communicates with the microcontroller through one of its four physical serial interfaces, while the SD card reader is wired on the SPI microcontroller bus. Sensors can then be added by simply plugging them into one of the three remaining

Table 2. Summary of the power consumption of the electronics used, under active logging with 5 V power supply

Electronic component	Current consumption (mA at 5 V)
Arduino Mega	60
SD card reader	20 (dependent on SD card)
VN100 IMU	70
GPS and active antenna	30
Total	180

physical serial interfaces of the microcontroller, or by using the SPI or I2C bus. In addition, the GPS, SD card reader and sensors receive power through a MOSFET transistor that can be switched on and off from the microcontroller, which allows the whole instrument to be put in a low-power consumption mode if requested.

Since the VN100 sensor used in our study relies on a RS232 3 V level for serial communications while the microcontroller board uses TTL 5 V logic, a MAX232 logic converter chip is used for level conversion between the VN100 and the serial port of the microcontroller board used for logging. Data are logged directly in ASCII format at 10 Hz. Binary format can be used to compress the data, but this was not necessary in our case and therefore ASCII was chosen for ease of programming and debugging. The current consumption of the whole system, when logging both the IMU at 10 Hz and GPS data at 1 Hz, is 180 mA at 5 V (see Table 2). This is ~20 times less than the overall power consumption that was needed for powering the MOXA computer-based instrument used in Sutherland and Rabault (2016).

Battery autonomy is the limiting factor for long-time logging in cold regions, which is made an even more critical issue than in temperate environments since the capacity of traditionally used lead acid batteries drops drastically in cold (Chang and Bonnet, 2010). We solve this issue by using industry grade rechargeable prismatic lithium iron (LiFe) batteries that feature low self-discharge and excellent performance in the

cold. Two 40 Ah, 3.2 V cells are assembled in series to provide a voltage of 6.4 V, which is reduced to the 5 V needed by our electronics using a low dropout voltage regulator. In addition, a protection circuit module is inserted between the battery and the voltage regulator to prevent overloading or overdischarging. This solution was tested in the laboratory with the complete instrument including the VN100 IMU at a temperature of -18° , and was able to work continuously for over 8 days. When only a few hours of logging are needed, we use more affordable lithium ion batteries.

To make the instrument resilient to failures caused by external events, such as short power interruptions due to shocks or other real work issues, a watchdog timer is used to reboot the microcontroller in case of a malfunctioning. In addition, the microcontroller logs the data to a new file every 15 min, and the name of the previous file is stored in the nonvolatile EEPROM microcontroller memory to avoid erasing previous data even in the event of a reboot by the watchdog. This ensures that at most 15 min of data will be lost in case of a watchdog reset or power loss.

The microcontroller board, IMU, GPS chip and antenna, SD card reader and battery with protection circuit module are enclosed in a robust pelican case. The pelican cases are chosen, so that the whole system is buoyant, independently of any additional float.

Using microcontrollers presents several advantages over more powerful computer systems, such as the MOXA computer used in Sutherland and Rabault (2016). Price, power consumption, complexity, weight and size can be reduced, and therefore more sensors can be deployed for the same budget and can deliver longer autonomy (over 1 week of continuous measurements for an instrument weighting <5 kg) without operator intervention. Microcontrollers are not able to run sophisticated embedded processing, but they are able to perform logging and to interact with various sensors. More details about the code and the electrical components used are available on the corresponding author GitHub repository (<https://github.com/jerabaul29/LoggerWavesInIce>).

MS received 20 May 2016 and accepted in revised form 3 January 2017; first published online 8 February 2017

2.3 Publication 3: A Method to Estimate Reflection and Directional Spread Using Rotary Spectra from Accelerometers on Large Ice Floes

Sutherland, G., Rabault, J., and Jensen, A. (2017), "A Method to Estimate Reflection and Directional Spread Using Rotary Spectra from Accelerometers on Large Ice Floes", *Journal of Atmospheric and Oceanic Technology*, 34(5):1125–1137.

A Method to Estimate Reflection and Directional Spread Using Rotary Spectra from Accelerometers on Large Ice Floes

GRAIG SUTHERLAND, JEAN RABAULT, AND ATLE JENSEN

Department of Mathematics, University of Oslo, Oslo, Norway

(Manuscript received 7 November 2016, in final form 16 February 2017)

ABSTRACT

The directional wave spectra in sea ice are an important aspect of wave evolution and can provide insights into the dominant components of wave dissipation, that is, dissipation due to scattering or dissipation due to viscous processes under the ice. A robust method for the measurement of directional wave spectra parameters in sea ice from a three-axis accelerometer—or a heave, pitch, and roll sensor—is proposed. The method takes advantage of certain aspects of sea ice and makes use of rotary spectra techniques to provide model-free estimates for the mean wave direction, directional spread, and reflection coefficient. The method is ideally suited for large ice floes—that is, where the ice floe length scale is much greater than the wavelength—but a framework is provided to expand the parameter space where the method may be effective.

1. Introduction

It has been common practice to use accelerometers, or inertial motion units (IMUs), to detect surface wave motion in sea ice (e.g., Wadhams et al. 1986). These have several advantages, including low cost, relatively easy to deploy, and extensive literature on using such sensors for measuring ocean waves (Bender et al. 2010). While techniques to obtain one-dimensional estimates of the wave energy are relatively robust (Bender et al. 2010), there are several challenges associated with calculated directional wave spectra from a single sensor (Benoit 1992; Young 1994). One of the largest challenges for measuring waves in ice is due to the multimodal nature expected from reflections, scattering from inhomogeneities in the ice cover and changes in the dispersion relation (Wadhams et al. 1986; Sutherland and Rabault 2016).

Understanding the directional spectra is important in order to address the dominant mechanism for wave attenuation, which is due to the scattering of wave energy arising from inhomogeneity in the ice cover or due to viscous attenuation between the ice cover and the fluid beneath (Squire et al. 1995; Squire 2007). While both methods are expected to give an exponential amplitude decay as a function of distance

(Wadhams et al. 1988), distinction between the two dissipative processes is expected to be possible if accurate measurements of the directional spread are available (Ardhuin et al. 2016). This is true for pack ice and the marginal ice zone (MIZ), as Ardhuin et al. (2016) used observations located between 1000 and 1500 km from the ice edge to infer the dissipation mechanism for waves with a period greater than 19 s.

The only published in situ study of the directional wave spectra in sea ice, to our knowledge (and according to Squire and Montiel 2016), is the study by Wadhams et al. (1986), who used several heave, pitch, and roll buoys to calculate the spectra inside and outside the marginal ice zone. Wadhams et al. (1986) calculated directional spectra using the methodology of Long and Hasselmann (1979), which is an inverse technique that fits the observations to a preferred parametric model for the shape of the directional spectra, as this method has been shown to resolve bimodal seas (Lawson and Long 1983). There are other methodologies for calculating the directional spectra in bimodal seas, but they all require knowledge of the directional shape function and use various techniques to obtain the best fit [see Benoit (1992) for a review of some of the techniques]. As a first approach we will make no assumptions about the spectral shape and will work directly with the Fourier series expansion

Corresponding author: Graig Sutherland, graigors@math.uio.no

approach of Longuet-Higgins et al. (1963). This approach is used in part to simplify the analysis, but it is also justified due to the scarcity of observations of directional spectra in ice and the lack of data with regard to a preferred spreading shape. Recent advances in the development of low-cost IMUs have allowed for the development of wave sensors that can be developed into wave buoys or easily deployed on ice floes (e.g., Doble and Wadhams 2006; Kohout et al. 2015; Rabault et al. 2016). This development will make it easier to measure waves in ice and therefore greatly increase the number of in situ observations available. In addition, as these sensors can take advantage of satellite communications, such as Iridium, to send data remotely, it is advantageous to be able to estimate aspects of the directional spectra in a robust manner, similar to the model-independent parameters proposed by Kuik et al. (1988), to reduce data transmission volume.

One of the primary motivations for this paper is to explain why the horizontal acceleration, as measured by an IMU on sea ice presented by Sutherland and Rabault (2016) and Rabault et al. (2016), is equivalent in magnitude to the vertical acceleration. In previous studies where the horizontal acceleration was presented (Fox and Haskell 2001; Bender et al. 2010), the acceleration orthogonal to the vertical was shown to be negligible. The studies of Sutherland and Rabault (2016) and Rabault et al. (2016) intuitively used this information to infer the direction of propagation but lacked a thorough analysis as to why this should be so. In this paper, a new methodology for estimating information about the directional spectra is presented. This method takes advantage of typical IMU measurements in order to obtain robust estimates of mean direction, directional spread, and reflection. These directional parameters are estimated using a rotary spectra technique (Gonella 1972). This technique is compared with that of Longuet-Higgins et al. (1963) and model-independent estimates using the Fourier coefficients (Kuik et al. 1988). The outline of the paper is as follows. Section 2 outlines the theoretical basis for our methodology and how it relates to the original theory as laid out by Longuet-Higgins et al. (1963). The data and methodology are presented in section 3. Details of the wave motion as measured by IMUs are presented in section 4. Calculation of directional spectra using an IMU and comparisons with the new rotary spectra method, along with estimating model-independent parameters for directional spread and reflection, are presented in 5. A summary and discussion of the results, along with limitations of the proposed method, can be found in section 6.

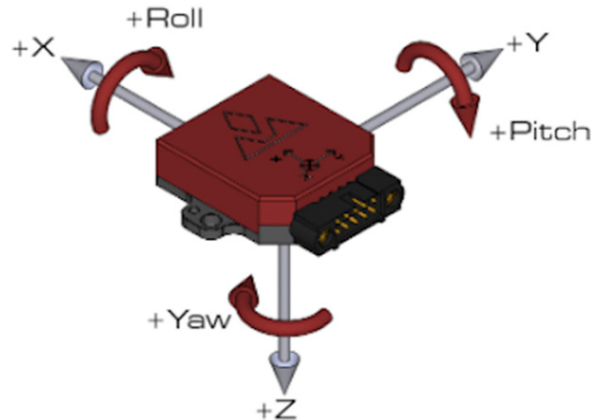


FIG. 1. Axis orientation for the VN-100 IMU.

2. Theory

We begin our analysis with the three orthogonal accelerations in the reference frame of the IMU, as shown by Bender et al. (2010) to be written as

$$X_S = a_x + g_x, \quad (1)$$

$$Y_S = a_y + g_y, \quad (2)$$

$$Z_S = a_z + g_z, \quad (3)$$

where a_x , a_y , and a_z are the three orthogonal accelerations and g_x , g_y , and g_z are the components of gravity in the x , y , and z directions, respectively, of the IMU frame of reference, which we denote by the subscript S . There exists some variability in the coordinate system used by various IMU manufacturers (Bender et al. 2010), but for our purposes we will use the VN-100 manufactured by VectorNav (2014) and the orientation is shown in Fig. 1. The components of gravity in each of the three orthogonal components are a function of the pitch θ , defined to be the angle rotated about the y axis in a right-hand system, and ϕ , defined to be the angle rotated about the x axis in a right-hand system, such that

$$g_x = g \sin\theta, \quad (4)$$

$$g_y = -g \cos\theta \sin\phi, \quad (5)$$

$$g_z = -g \cos\theta \cos\phi. \quad (6)$$

Equations (4)–(6) are identical to method IV of Bender et al. (2010).

Up to this point there has been no assumption made about the nature of the sea ice cover at the surface. For waves in sea ice, the ratio of the horizontal dimension of the ice floe to the wavelength is an important parameter determining the accelerations and angles of the ice floe relative to the ocean surface (Masson and LeBlond 1989;

Meylan and Squire 1994). For ice floes much smaller than the wavelength, the response amplitude operator (RAO) of an ice floe to surface waves is controlled by gravity—that is, the floe can slide down wave slopes—friction between the floe and water, and inertia of the floe (Marchenko 1999). For wavelengths comparable to the ice floe length scale, there can exist complex resonance characteristics strongly affecting the RAO (Masson and LeBlond 1989). For wavelengths much smaller than the ice floe, the ice floe will follow the waves under the ice and the flexural motion of the ice can change the dispersion relation. In general, the accelerations and angles in the three directions are functions of the incident wavelength, the floe geometry, and to a small extent the water depth (Masson and LeBlond 1989). Below we will make some assumptions consistent with the conditions encountered by Sutherland and Rabault (2016), but note that the method may still work for smaller floes. This latter point will be elaborated on further in section 6.

As one of the primary motivations for this study is to explain the horizontal accelerations observed by an IMU on a large continuous sheet of ice (Sutherland and Rabault 2016), we will make the assumption that the horizontal length scale of the ice floe is much greater than the wavelength. This assumption allows us to further assume that the ice is well coupled with the surface waves—that is, that the horizontal motion is negligible, $a_x = a_y = 0$ —and that the angles θ and φ are small enough to neglect the second-order terms, for example, $\sin\theta \approx \theta$ and $\cos\theta \approx 1$. These assumptions, along with (4)–(6), allow (1)–(3) to be written as

$$X_s = g\theta, \quad (7)$$

$$Y_s = -g\phi, \quad (8)$$

$$Z_s = a_z - g. \quad (9)$$

Equations (7)–(9) show that a 3D arrangement of accelerometers on sea ice, to first order, can measure the vertical acceleration along with the angles given the abovementioned assumptions. This is explored further for gravity waves propagating in sea ice.

The surface elevation can be written as

$$\eta(\mathbf{x}, t) = \Re[A e^{i(\mathbf{k} \cdot \mathbf{x} - \omega t)}] = \Re[A e^{i\Phi}], \quad (10)$$

where \Re denotes the real part, A is the amplitude, \mathbf{k} is the wavenumber vector, ω is the angular frequency, \mathbf{x} is the position vector, t is time, and $\Phi = \mathbf{k} \cdot \mathbf{x} - \omega t$ is the phase function. While (10) is the elevation for a single frequency, it can easily be written as a linear sum of several frequencies with no loss of generality. The angles θ and φ are related to the slopes in the x and y

directions, respectively, and can be calculated from (10), that is,

$$\theta = \frac{\partial \eta}{\partial x} = ik_x A e^{i\Phi}, \quad (11)$$

$$-\phi = \frac{\partial \eta}{\partial y} = ik_y A e^{i\Phi}. \quad (12)$$

The vertical acceleration in our coordinate system, where z is positive downward, is calculated as

$$a_z = -\frac{\partial^2 \eta}{\partial t^2} = \omega^2 A e^{i\Phi}. \quad (13)$$

The dispersion relation, assuming a Kirchoff–Love thin elastic plate model (Marchenko et al. 2013), can be written as

$$\omega^2 = gk \tanh(kH) \left(1 + \frac{D}{\rho g} k^4\right), \quad (14)$$

where $k = |\mathbf{k}| = \sqrt{k_x^2 + k_y^2}$, k_x and k_y are the orthogonal components of the wavenumber vector \mathbf{k} , $D = Eh^3/[12(1 - \nu^2)]$ is the bending modulus with E being the elastic modulus of ice, H is the water depth, h is the ice thickness, ρ is the water density, and ν is the Poisson ratio. We define a characteristic length scale for the flexural term identical to Fox et al. (2001), that is,

$$\ell_c = \left(\frac{D}{\rho g}\right)^{1/4}. \quad (15)$$

There are other factors that can affect wave dispersion, such as the inertia of the ice and compressive stress (Liu and Mollo-Christensen 1988). However, ice stresses in an adjacent fjord have a maximum of 37.7 kPa away from the hinge zone (Vindegg 2014), which is much too small to affect the dispersion for typical surface wave frequencies. The inertial term may affect the higher wavenumbers, but it will be limited to a maximum 10% deviation in the dispersion relation for wavelengths less than 50 m and ice thicknesses less than 1 m, and is therefore neglected.

The wavenumber k can be written in terms of one of the orthogonal components k_x and k_y as

$$k = k_x \left[1 + \left(\frac{k_y}{k_x}\right)^2\right]^{1/2}. \quad (16)$$

In general, at least for lower frequencies, which do not quickly attenuate, waves in ice can be approximated as long crested, that is, $(k_y/k_x)^2 \ll 1$ (Sutherland and Rabault 2016). Therefore, from (16), $k_x \approx k$ and k_y will be a small fraction of k . We define $\delta k = k - k_y$, and solving

for k such that $k_y = \varepsilon k$ and ignoring terms of δk^2 gives $\varepsilon = (2\delta k/k)^{1/2}$. Substituting (11)–(15) into (7)–(9) gives

$$X_S = \frac{i\omega^2 A e^{i\Phi}}{\tanh kH[1 + (k\ell_c)^4]} \quad (17)$$

$$Y_S = \frac{\varepsilon i\omega^2 A e^{i\Phi}}{\tanh kH[1 + (k\ell_c)^4]} \quad (18)$$

$$Z_S = \omega^2 A e^{i\Phi} - g. \quad (19)$$

Equations (17)–(19) show that the magnitude of X_S will be comparable to Z_S with a 90° phase shift for wavenumbers $(k\ell_c)^4 \ll 1$. For Y_S , the same 90° phase shift is expected but with a much reduced amplitude.

The characteristic length for a range of E of $1 - 5 \times 10^9 \text{ N m}^{-2}$ and ice thickness h of 0.5 – 1 m gives a range for ℓ_c between 0.58 and 14.6 m. For ocean swell where $(k\ell_c)^4 \ll 1$, the bending term can be omitted and X_S and Z_S should have the same magnitude. For thick, stiffer ice, the flexural motion will impact higher frequencies of wave motion, but for thin, more pliable ice the bending term in the dispersion relation can be safely neglected.

The finite depth can also lead to an increase in the measured horizontal acceleration X_S relative to the vertical acceleration Z_S for small values of kH . Taking $H = 80$ m, which is the depth from Sutherland and Rabault (2016), gives an increase of X_S relative to Z_S of 0.5% for wavelengths of 168 m, corresponding to waves with periods greater than 10 s, and 3.7% for wavelengths of 251 m, corresponding to waves with periods greater than 13 s. For $H = 160$ m, which is the depth for the other data that we will present later, the periods of 18 and 15 s correspond to the 0.5% and 3.7% errors, respectively.

Equations (17)–(19) bring up an interesting corollary with regard to when the magnitude of X_S is not equal to Z_S (e.g., Fox and Haskell 2001) or when X_S and Z_S are not 90° out of phase (e.g., Sutherland and Rabault 2016). Such an inequality could arise from physical horizontal motion (i.e., surge), flexural motion [i.e., $(k\ell_c)^4 \gg 1$], or floe–floe interactions (Yiew et al. 2016), or the waves are not sufficiently long crested (e.g., $|X_S| \approx |Y_S|$). Therefore, the accelerations measured in the IMU reference frame can give information about wave propagation when $|Z_S| \approx |X_S|$ and Z_S and X_S are 90° out of phase. The method also potentially gives some information about the ice cover when only a subset of the abovementioned assumptions hold, and this will be presented for a particular example later on in the manuscript.

3. Data and methods

IMUs equipped with a three-axis accelerometer, a three-axis gyroscope, and a three-axis magnetometer

were used to measure ice motion. The IMUs used are the VN-100 manufactured by VectorNav (2014). Each IMU is factory calibrated for temperatures ranging from -40° to 85°C . The accelerometer has a factory-rated resolution of $5 \times 10^{-4} \text{ g}$ and the angular rate resolution is $3.5 \times 10^{-4} \text{ rad s}^{-1}$. Details of the IMUs and the processing can be found in Rabault et al. (2016).

The VN-100 samples internally at a rate of 800 Hz, and the raw signal is then low-pass filtered by the embedded processor so that the output rate is reduced to 10 Hz. The use of a low-pass filter effectively suppresses aliasing and reduces the noise level of the instrument. The power spectral density (PSD) was calculated for segments of 45 min using the Welch method with a Hanning window of length 5.5 min and a half-width overlap. For overlapping segmented data, the degrees of freedom (DoF) can be approximated by (Earle 1996)

$$\text{DoF} = \frac{2K}{1 + 0.4(1 - K^{-1})}, \quad (20)$$

where K is the total number of segments. We have 15 segments that give us nearly 22 DoF. The PSD of the acceleration is related to the PSD of the surface elevation by the weighting function ω^{-4} (Tucker and Pitt 2001).

Several steps are outlined to obtain the orthogonal coordinates—that is, x , y , and z —relative to the wave. First, the vertical z axis is obtained by the mean acceleration vector measured by the IMU over the duration of the observations. This assumes that gravity is much greater than any mean inertial acceleration experienced by the IMU. Second, the x direction is obtained by maximizing the variance in the horizontal acceleration, as measured by the IMU, in the orthogonal x – y plane about the z axis. The x direction is then verified by ensuring that the gyroscope also has a maximum variance in the same direction. If the direction is changing in time, then the coordinates could be calculated on time windows comparable to the 45 -min time series used for the PSD estimates.

In our analysis we use three different test cases from two different field studies. The first two cases are from a study performed on fast ice in Tempelfjorden, Svalbard ($78^\circ 23' \text{N}$, $16^\circ 54' \text{E}$), during March 2015, as presented in Sutherland and Rabault (2016) and Rabault et al. (2016). The third case is from a study on an ice floe in the Barents Sea ($77^\circ 45' \text{N}$, $25^\circ 15' \text{E}$) during May 2016. The IMU used for observing the wave motion is identical in each case, while the data acquisition system and configuration have been updated in case c, identical to that presented in Rabault et al. (2017). The ice floe in the Barents Sea is approximately 2 km in diameter and 0.3 m thick.

The three different cases all have similar integrated energy but differ in their frequency distribution. Case a

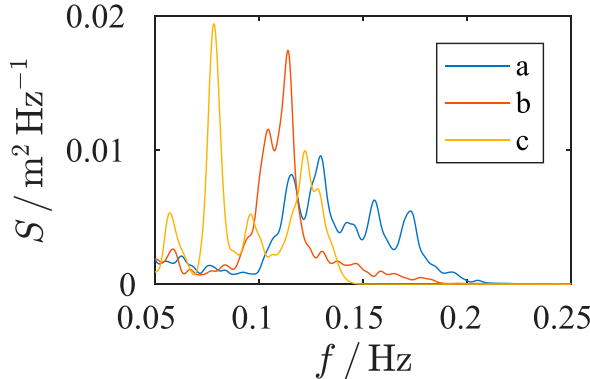


FIG. 2. One-dimensional PSD for three test cases.

is a mixed sea in Tempelfjorden in fast ice with high-frequency energy and an observed deviation from the deep-water dispersion relation (Sutherland and Rabault 2016). Case b is also in Tempelfjorden but after case a, when there was no longer clear evidence for flexural motion. Case c is a swell-dominated regime on a 2-km ice floe in the Barents Sea. Figure 2 shows the PSD for each of the three cases. A summary of the wave parameters, such as significant wave height H_s , peak period T_p , and zero-upcrossing period T_{z0} , can be found in Table 1. The significant wave height and zero-upcrossing periods are calculated from the wave moments, that is, $H_s = 4\sqrt{m_0}$ and $T_{z0} = \sqrt{m_2/m_0}$, respectively, where the i th wave moment is defined as

$$m_i = \int_{f_1}^{f_2} f^i S(f) df, \quad (21)$$

where $S(f)$ denotes the PSD and f_1 and f_2 are the frequency limits, which we select to be $f_1 = 0.05$ Hz and $f_2 = 0.25$ Hz. The lower frequency limit is determined by the IMU sensitivity, and the upper limit is selected to limit high-frequency motion unrelated to surface waves.

In our analysis we will take advantage that the vertical and horizontal accelerations, where the horizontal acceleration is due to the aliasing of the gravity vector, are 90° out of phase and calculate the wave propagation using a rotary spectrum. This technique is commonly used in calculating the rotation of ocean currents (e.g., Gonella 1972) but not so common for surface wave propagation (Sutherland and Rabault 2016).

The vertical and horizontal accelerations measured by the IMU may be written using complex notation, that is,

$$Z_S(t) + iX_S(t) = a_+ e^{i\omega t} + a_- e^{-i\omega t}, \quad (22)$$

where a_+ is the acceleration in the positive orientation in the $x - z$ plane and a_- is the acceleration in the negative

TABLE 1. Wave parameters for the three test cases chosen in this study.

Case	H_s (m)	T_p (s)	T_{z0} (s)
a	0.082	7.7	7.9
b	0.088	8.8	8.9
c	0.083	12.8	10.1

orientation in the $x - z$ plane. Taking the PSD of (22), and scaled by ω^{-4} to convert from acceleration to elevation, gives the energy in the positive (or forward) direction for positive frequencies and the negative (or backward) direction for negative frequencies. Using the measured accelerations, the energy calculated from the rotary PSD is twice the true value calculated from Z_S . The factor of 2 arises from Z_S and X_S having the same magnitude, which is equal to $a\omega^2$, so the $\text{PSD}(Z_S + iX_S) \propto a^2\omega^4 + a^2\omega^4 = 2a^2\omega^4$, where a is the amplitude in (17)–(19).

The rotary spectrum is also used to calculate the predominant direction of wave propagation. After the vertical vector is determined from the mean acceleration, which should be equal to g , the two orthogonal vectors are rotated around this z axis and the optimal orientation is chosen by maximizing the integrated energy for the positive frequencies. Figure 3 shows the rotary spectra calculated in the along-wave (blue) and cross-wave (red) directions for the three test cases. Each case has high asymmetry in the along-wave direction (i.e., any reflected energy is significantly less than the propagating energy) and high symmetry in the cross-wave direction (i.e., symmetric wave shape).

4. Wave motion

Investigating the relationship between the accelerations and angles measured by the IMU can shed some light on some of the assumptions that we have made. For example, if $X_S \approx g\theta$ and the magnitudes of X_S and $Z_S - g$ (henceforth the $-g$ is dropped from the notation) are nearly the same, then the assumption of negligible horizontal motion of the ice, small wave steepness, and a dispersion relation of $\omega^2 = gk$ are validated. Figure 4 shows the vertical acceleration Z_S and the horizontal acceleration in the direction of wave propagation X_S measured by the IMU, in addition to g times the pitch angle θ . It is clear that $X_S \approx g\theta$ and that any physical horizontal motion in the three cases is negligible. The accelerations X_S and Z_S are similar in magnitude but not identical. Since the horizontal motion of the ice floe is shown to be negligible, differences between X_S and Z_S will arise from the dispersion relation or possibly from the long-crested approximation.

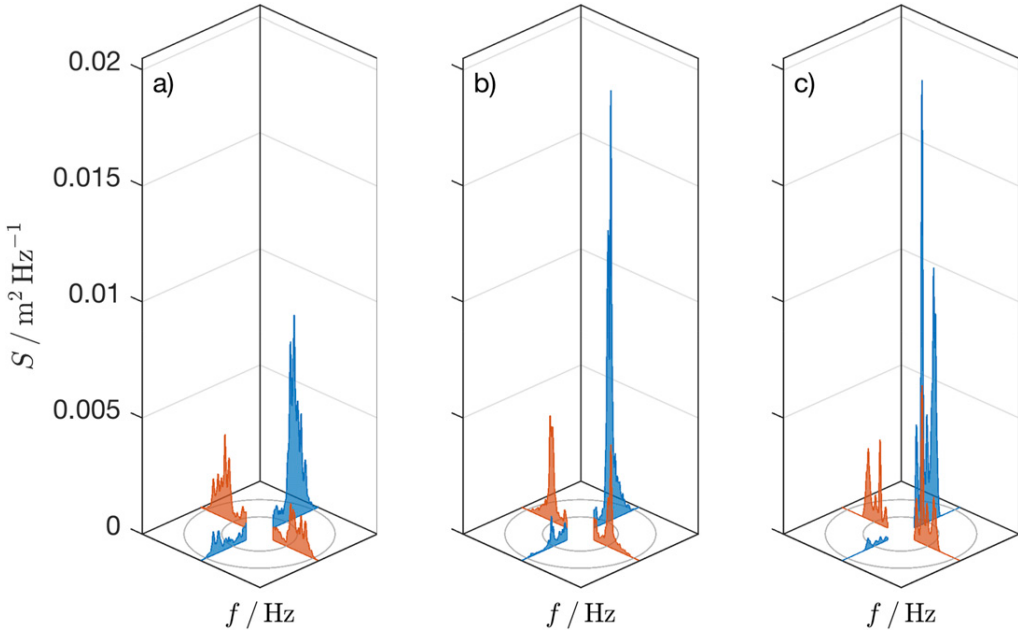


FIG. 3. Rotary spectra in the along-wave (blue) and cross-wave (red) directions for (a) case a, (b) case b, and (c) case c. Gray circles on the base represent 0.1-Hz frequency contours.

From (17) and (19), the accelerations Z_s and X_s are expected to be 90° out of phase with one another, which can be tested by looking at the cospectral density of the two signals. The phase angle α between the acceleration measured in the z and x axes can be determined from the cospectral power density S_{zx} ,

$$\alpha = \tan^{-1} \left[\frac{\Im(S_{zx})}{\Re(S_{zx})} \right], \quad (23)$$

where \Im denotes the imaginary part, assuming that the two signals are correlated. The spectral coherence between the two signals γ_{zx} is calculated by

$$\gamma_{zx}^2 = \frac{S_{zx} S_{zx}^*}{S_{zz} S_{xx}}, \quad (24)$$

where the asterisk (*) denotes the complex conjugate. A value of $\gamma^2 > 0.305$ rejects the hypothesis that the two signals are not correlated at the 99.9% confidence interval (Amos and Koopmans 1963).

The coherence (γ^2) and phase angle (α) between Z_s and X_s are shown in Fig. 5 for the three cases. When $\alpha = 90^\circ$, the vertical and horizontal components are in quadrature and the deep-water dispersion relation is valid. The three cases show a slightly different relation between the two orthogonal accelerations. Figures 5b and 5c show that frequencies with a high correlation ($\gamma^2 > 0.75$) correspond

with $\alpha \approx 90^\circ$. This is in contrast with Figs. 5a and 5b, in which both show deviations from $\alpha = 90^\circ$ when coherence is high ($\gamma^2 > 0.75$). This deviation may be due to flexural motions as it increases with frequency, hence $k\ell_c$ has increased. The deviation is greater for case a than for case b,

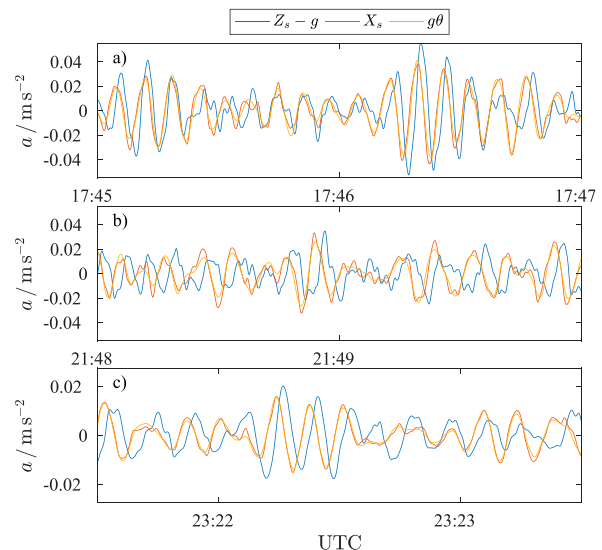


FIG. 4. Acceleration in the along-wave direction measured in the sensor frame of reference for (a) case a, (b) case b, and (c) case c. Horizontal acceleration is predominantly due to the projection of the gravity vector and is equal to $g\theta$.

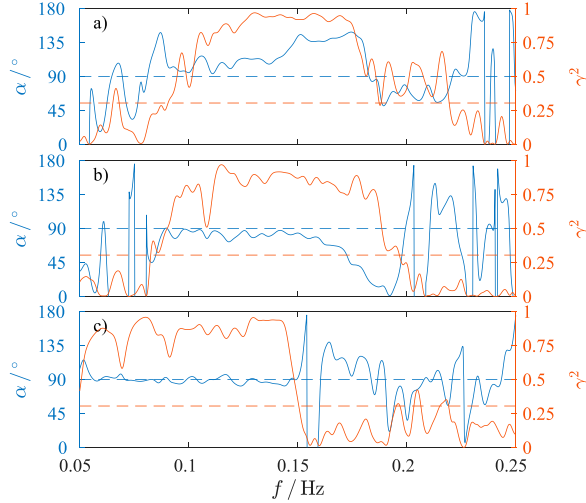


FIG. 5. Phase angle and correlation measured in the sensor frame of reference for (a) case a, (b) case b, and (c) case c. Blue line shows the phase angle between $Z_S - g$ and X_S , and the blue dashed line shows a phase difference of 90°. Red line shows the coherence squared, and the red dashed line indicates the 99.9% probability of rejecting the null hypothesis.

which corresponds to a time when there was evidence of flexural motion from the observed dispersion relation (Sutherland and Rabault 2016).

To test the long-crested wave hypothesis, the same analysis was applied to Y_S and in general Y_S and Z_S are not correlated at the 99.9% confidence level. The details of this analysis can be found in the [appendix](#). This suggests that the phase difference observed between X_S and Z_S is due to the dispersion relation.

5. Directional spectra

An important aspect of geophysical surface waves is the directional spectrum, which includes information about the direction of wave propagation and the directional spread. The directional spectrum F of surface waves as a function of frequency f and direction ψ can be written as

$$F(f, \psi) = S(f)D(f, \psi), \quad (25)$$

where $S(f)$ is the PSD and $D(f, \psi)$ is a spreading function, which is normalized so that

$$\int_{-\pi}^{\pi} D(f, \psi) d\psi = 1.$$

[Longuet-Higgins et al. \(1963\)](#) showed for a heave, pitch, and roll buoy that the directional spectrum can be approximated from the first five Fourier coefficients such that

$$F(f, \psi) = \frac{1}{2}A_0 + (A_1 \cos\psi + B_1 \sin\psi) + (A_2 \cos 2\psi + B_2 \sin 2\psi) + \dots, \quad (26)$$

where the coefficients are determined from the cospectra C_{ij} and quadspectra Q_{ij} of the i and j quantities denoted by 1, 2, and 3 for the vertical acceleration, pitch, and roll, respectively, that is,

$$\begin{aligned} A_0 &= \int_{-\pi}^{\pi} F(f, \psi) d\psi = \frac{1}{\omega^4 \pi} C_{11}, \\ A_1 &= \int_{-\pi}^{\pi} \cos(\psi) F(f, \psi) d\psi = \frac{Q_{12}}{\omega^2 \pi} \left(\frac{C_{11}}{C_{22} + C_{33}} \right)^{1/2}, \\ B_1 &= \int_{-\pi}^{\pi} \sin(\psi) F(f, \psi) d\psi = \frac{Q_{13}}{\omega^2 \pi} \left(\frac{C_{11}}{C_{22} + C_{33}} \right)^{1/2}, \\ A_2 &= \int_{-\pi}^{\pi} \cos(2\psi) F(f, \psi) d\psi = \frac{C_{22} - C_{33}}{\pi} \left(\frac{C_{11}}{C_{22} + C_{33}} \right), \\ B_2 &= \int_{-\pi}^{\pi} \sin(2\psi) F(f, \psi) d\psi = \frac{C_{23}}{\pi} \left(\frac{C_{11}}{C_{22} + C_{33}} \right). \end{aligned} \quad (27)$$

[Longuet-Higgins et al. \(1963\)](#) went on to show that omitting the higher-order terms in (26) is equivalent to applying a weighting function to the true spectrum, that is,

$$F_1(f, \psi) = \frac{1}{2\pi} \int_{-\pi}^{\pi} F(f, \psi') W_1(\psi' - \psi) d\psi', \quad (28)$$

where $W_1 = 1 + 2 \cos(\psi' - \psi) + 2 \cos 2(\psi' - \psi)$ and F_1 is the truncated (26). The weighting function W_1 can be negative for certain directions, which can make $F_1(f, \psi)$ negative, while $F(f, \psi)$ is expected to be strictly positive. To avoid negative energy, [Longuet-Higgins et al. \(1963\)](#) proposed an alternate weighting function that is positive for all directions but arbitrarily widens the distribution,

$$\begin{aligned} F_2(f, \psi) &= \frac{1}{2}A_0 + \frac{2}{3}(A_1 \cos\psi + B_1 \sin\psi) \\ &\quad + \frac{1}{6}(A_2 \cos 2\psi + B_2 \sin 2\psi). \end{aligned} \quad (29)$$

[Figure 6](#) shows the directional distribution, where $D_i(f, \psi) = F_i(f, \psi)/S(f)$, at the peak frequency for each test case. The truncated Fourier series, $D_1(f, \psi)$, gives a narrower peak, negative energy around $\pm 90^\circ$ and positive energy at $\pm 180^\circ$ from the direction of propagation. This is quite different than for $D_2(f, \psi)$, which smooths out the spectral energy to angles greater than $\pm 90^\circ$ and does not have a second peak at $\pm 180^\circ$. So, while it is true that $D_1(f, \psi)$ is negative at directions that are

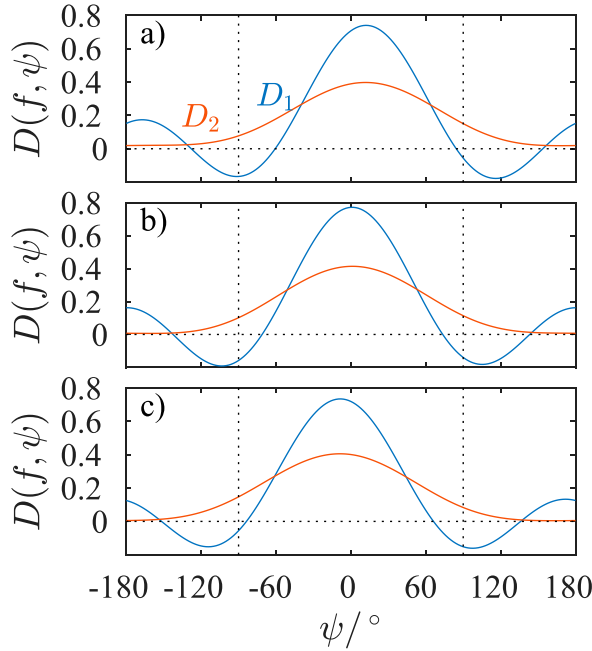


FIG. 6. Directional spreading function of truncated Fourier series D_1 (blue) and weighted function D_2 proposed by Longuet-Higgins et al. (1963) (red) at the peak frequency for the three cases.

orthogonal to the principal direction of propagation, most of the energy for waves in ice is expected to be along one principal direction (Wadhams et al. 1986). Furthermore, since the slope is generally very small for waves in ice, the curvature will be significantly smaller, allowing for a further argument for using the truncated Fourier series as opposed to selecting somewhat arbitrary weights.

To compare the directional spectra estimates with the rotary spectra method, the directional spectra is integrated over each hemisphere as

$$\begin{aligned} S_{Di}(f) &= \int_{-\pi/2}^{\pi/2} \cos\psi F_i(f, \psi) d\psi, \\ S_{Di}(-f) &= \int_{-\pi/2}^{\pi/2} |\cos(\psi - \pi)| F_i(f, \psi - \pi) d\psi, \end{aligned} \quad (30)$$

where i is either 1 or 2 depending on which directional form is used for the wave spectra. The cosine term in (30) is used to project the directional spectra on the axis of propagation used for the rotary spectra. While cosine weighting has little effect on the positive frequencies, as most of the energy is at $\psi = 0$, it will impact the negative frequencies where energy at $\psi = \pm 90^\circ$ can be comparable to $\psi = \pm 180^\circ$ depending on the spreading function used. Figure 7 shows the comparison of (30) with estimates using the 1D vertical, 1D horizontal, and rotary spectra. Note the lower noise level of case c compared with the other two

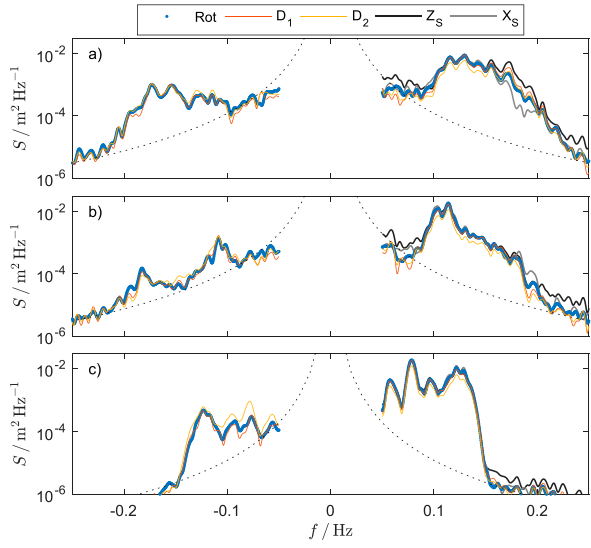


FIG. 7. Rotary spectra compared with other spectral energy estimates for (a) case a, (b) case b, and (c) case c. Noise level is shown by the dashed black line. Note that (c) has a lower noise level than (a) and (b).

cases. This is due to the implementation of the onboard low-pass filter for the Lance cruise, which was not done with the setup for the Tempelfjorden experiment. The onboard filter is programmed to obtain a boxcar average of 80 adjacent samples at the internal IMU sampling rate of 800 Hz and outputs this value at 10 Hz.

There is good qualitative agreement between all estimates of the PSD for the three test cases presented. It is somewhat surprising/encouraging that there is such excellent agreement for the negative frequencies—that is, the “reflected” energy portion of the spectra—and that both directional spectral shapes give similar estimates. This result suggests that the reflection coefficient may be independent of the exact shape of the distribution and calculated from integrated parameters, similar to directional spread (Kuik et al. 1988).

a. Comparisons with rotary spectra

The rotary spectra of the counterclockwise- and clockwise-rotating components (which we will denote by positive and negative frequencies, respectively) can be written in terms of the cospectra and quadspectra of the two components (Gonella 1972), that is,

$$S_{xz}^{\text{rot}}(f) = \frac{1}{8} (C_{xx} + C_{zz} + 2Q_{xz}), \quad (31)$$

$$S_{xz}^{\text{rot}}(-f) = \frac{1}{8} (C_{xx} + C_{zz} - 2Q_{xz}), \quad (32)$$

where C_{ij} and Q_{ij} are the cospectra and quadspectra, respectively, used to define the Fourier coefficients in

(27). Noting that z is equivalent to 1 in (27) and x is equivalent to g times 2 in (27), and using the deep-water dispersion relation (i.e., $C_{zz} = C_{xx}$), which assumes that the wavenumber k satisfies both $(k\ell_c)^4 \ll 1$ and $\tanh kH \approx 1$, we obtain (31) and (32) in terms of the Fourier coefficients, that is,

$$S_{xz}^{\text{rot}}(f) = \frac{A_0 \pi \omega^4}{4} \left(1 + \frac{A_1}{A_0} \right), \quad (33)$$

$$S_{xz}^{\text{rot}}(-f) = \frac{A_0 \pi \omega^4}{4} \left(1 - \frac{A_1}{A_0} \right). \quad (34)$$

Similarly, the rotary spectra in the cross-wave direction can be written as

$$S_{yz}^{\text{rot}}(f) = \frac{A_0 \pi \omega^4}{4} \left[\left(\frac{1}{2} + \varepsilon^2 \right) + \frac{B_1}{A_0} \right], \quad (35)$$

$$S_{yz}^{\text{rot}}(-f) = \frac{A_0 \pi \omega^4}{4} \left[\left(\frac{1}{2} + \varepsilon^2 \right) - \frac{B_1}{A_0} \right]. \quad (36)$$

Equations (33)–(36) will be used to infer calculated values of directional spread and reflection with the Fourier coefficients.

b. Wave reflection

Estimating wave reflection in an ice-covered sea is difficult, as it requires the ability to resolve a bimodal spectrum, with the modes 180° apart, which is challenging using traditional techniques (Benoit 1992). A classic option is to statistically fit a parametric model for spreading from the data, a common model is the “cosine-2s model” $D(\psi) \propto \cos^{2s}(\psi/2)$, where s is the spreading factor and is identical to the methodology of Wadhams et al. (1986) in their study of directional spectra in sea ice. While such methods have shown to be effective in open water (Benoit 1992), there is little evidence suggesting that they will be as effective under an ice cover. Instead, we propose a simple method using rotary spectra, which can determine wave propagation by the clockwise and counterclockwise components. This method may be particularly well suited to measure waves in ice, as IMUs follow the surface relatively well with little horizontal acceleration (see Fig. 4). Furthermore, Wadhams et al. (1986) showed in their analysis that the direction of the reflected spectral peak is very close to 180° from the direction of the incident wave, which is an ideal situation for the use of rotary spectra.

Figure 7 shows that estimates of the reflected energy using the rotary spectra are similar to the directional spectra estimates projected onto the negative along-wave axis. It is expected that the shape of the directional spectrum $D(f, \psi)$ would affect the estimate of the reflected energy, but Fig. 7 shows very similar estimates

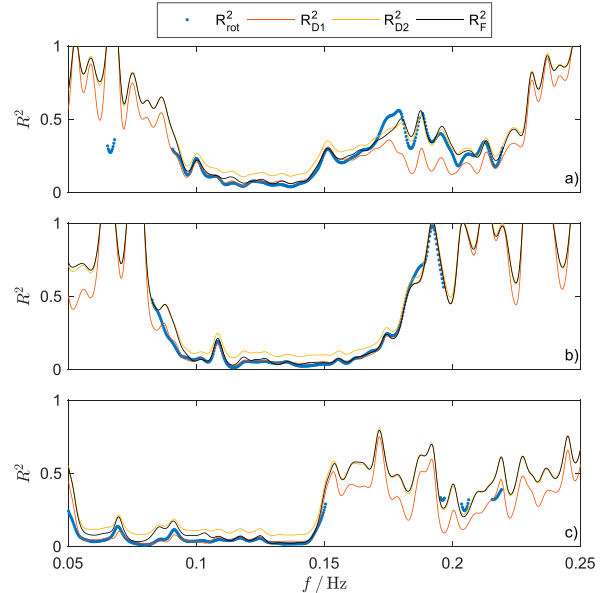


FIG. 8. Comparison of the reflection coefficient for (a) case a, (b) case b, and (c) case c, estimated from the rotary spectrum (blue) and the directional spectrum for two different directional spreading functions.

using the two different directional shapes. In Fig. 6, $D_1(f, \psi)$ shows two separate peaks at $\psi = 0^\circ$ and $\psi \approx \pm 180^\circ$, while $D_2(f, \psi)$ shows a broad peak that extends to angles greater than 90° and goes to zero for $\psi = \pm 180^\circ$. While the two directional estimates are quite different in the directional distribution of energy, it is striking that the integrated values are similar and that the energy propagating from the sea and toward the sea are consistent between the two methods.

The reflection coefficient R^2 is calculated from Fig. 7 using the definition

$$R^2 = \frac{S(-f)}{S(f)}, \quad (37)$$

where $S(\pm f)$ is the PSD estimated using either of the rotary spectral or directional spectral methods, $-f$ denotes the frequency of the reflected energy, and f is the frequency of the propagating energy. The reflection coefficient can also be written in terms of the Fourier coefficients using (33) and (34), which becomes

$$R_F^2 = \frac{1 - A_1/A_0}{1 + A_1/A_0}. \quad (38)$$

Figure 8 shows R^2 estimated using the different methods for the three cases. In all three cases, R_{D2}^2 is greater than the other estimates, which we interpret to arise from the increased spread due to the smoothing

function, as the weighting function is 0 when $\psi = \pm\pi$. The other estimates produce a striking similarity with one another. This similarity suggests that (38) may provide a model-free estimate of the reflection coefficient that can be calculated from the first-order Fourier coefficients.

c. Directional spread

Another important aspect is the directional spread of the propagating wave field. This term is model independent, as it can be calculated from the first-order Fourier coefficients (Kuik et al. 1988), that is,

$$\sigma_1 = \sqrt{2\left(1 - \frac{C_1}{A_0}\right)}, \quad (39)$$

$$\sigma_2 = \sqrt{\frac{1}{2}\left(1 - \frac{C_2}{A_0}\right)}, \quad (40)$$

where $C_i = \sqrt{A_i^2 + B_i^2}$. Equation (40) deviates slightly from the definition of Kuik et al. (1988) by using a different definition for C_2 . Our definition for σ_2 is consistent with Arduhin et al. (2016) and is chosen because it is solely dependent on the second-order Fourier coefficients. While not shown here, the difference between the two definitions of σ_2 is minimal.

We propose that the directional spread may also be estimated from the rotary spectra in the along- and cross-wave directions, which we define as

$$\sigma_r(f) = \tan^{-1} \left[\frac{S_{yz}^{\text{rot}}(f)}{S_{xz}^{\text{rot}}(f)} \right] + \tan^{-1} \left[\frac{S_{yz}^{\text{rot}}(-f)}{S_{xz}^{\text{rot}}(f)} \right], \quad (41)$$

where S_{xz}^{rot} is the along-wave (i.e., $x - z$ plane) rotary spectra and S_{yz}^{rot} is the cross-wave (i.e., $y - z$ plane) rotary spectra. Equation (41) gives a clear geometric relation between the along-wave and cross-wave directions for each frequency. The spread calculated by (41) can also be estimated from the Fourier coefficients using (33)–(36), that is,

$$\sigma_r^*(f) = \tan^{-1} \left[\frac{0.5 + B_1/A_0}{1 + A_1/A_0} \right] + \tan^{-1} \left[\frac{0.5 - B_1/A_0}{1 + A_1/A_0} \right], \quad (42)$$

where ϵ is neglected and thus σ_r^* is expected to provide a lower bound on the estimated spread.

Another method for the determination of the directional spread is to calculate the root-mean-square spread (Kuik et al. 1988), that is,

$$\sigma_D = \sqrt{\int_{-\pi}^{\pi} (\psi - \psi_0)^2 D(f, \psi) d\psi}, \quad (43)$$

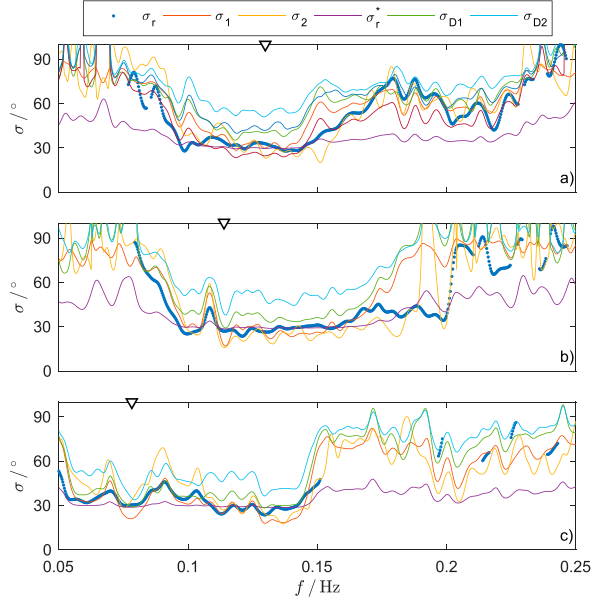


FIG. 9. Directional spread measured in the sensor reference frame for (a) case a, (b) case b, and (c) case c. Inverted triangles show local peaks in the 1D spectrum. Each estimate of the directional spread is multiplied by a factor to ensure the respective isotropic values are equal to 90°.

where ψ_0 is the mean wave direction defined from the Fourier coefficients as $\psi_0 = \tan^{-1} B_1/A_1$. There are various drawbacks to using (43), such as it requires calculating the directional distribution $D(f, \psi)$ and is not expected to be valid for large spreads (Longuet-Higgins et al. 1963), but it is presented here for purely comparative purposes.

Equation (41) estimates the spread from a purely geometrical reasoning, and thus the isotropic limit of $\sigma_r^{\text{iso}} = \pi/2 = 90^\circ$ is more intuitive than previous estimates. For example, the isotropic limit of (39) is $\sigma_1^{\text{iso}} = \sqrt{2} \approx 81^\circ$, while for (40) it is $\sigma_2^{\text{iso}} = \sqrt{2}/2 \approx 40.5^\circ$. Furthermore, the isotropic limit of (43) is $\sigma_D^{\text{iso}} = \pi/\sqrt{3} \approx 104^\circ$. It is tempting to normalize each estimate of spread by a factor related to the isotropic limits (see Squire and Montiel 2016). However, this is inconsistent with the results of Kuik et al. (1988), which showed that σ_1 , σ_2 , and σ_D all give similar results using synthetic data with relatively narrow angular distributions. It is hard to know a priori whether the spread will be small, so we scale each spread in a similar way as in Squire and Montiel (2016), but in our case we scale all of them to have the isotropic limit of 90°.

Figure 9 shows the comparison between the various definitions for the spread for the three test cases. Equation (42) assumes $\epsilon = 0$, which will give a lower estimate to the directional spread. For frequencies less than 0.15 Hz, all estimates of the spread, with the exception of σ_{D2} , give strikingly similar results. It is not too surprising

that σ_{D2} is a bit larger, as the directional spectrum is arbitrarily widened by a smoothing function in order to ensure the energy is positive for all angles.

There are some subtle differences between the methodologies. For instance, in Fig. 9a there is a deviation of spread estimates at $f = 0.15$ Hz that coincides with the frequency where a change in the dispersion relation due to flexural motions was observed (Sutherland and Rabault 2016). After this transition frequency, the estimates converge for frequencies greater than 0.17 Hz, suggesting that the effect of flexural motions on the calculated spread is complicated. This complication is also present in Fig. 9b, where spread estimates also deviated for frequencies between 0.17 and 0.20 Hz. For case c (Fig. 9c), the spread is consistent between the scaled estimates, with the exception of σ_{D1} for the same reasons as mentioned in the previous paragraph.

6. Summary and discussion

A new method for calculating aspects of directional wave spectra, such as mean direction, spread, and reflection, is presented for a single inertial motion unit (IMU) mounted on sea ice. This method is based on calculating the rotary spectra of the vertical and horizontal components of the acceleration as measured in the IMU reference, where the horizontal acceleration has been shown to be equal to g times the slope. This measured horizontal acceleration is predominantly due to the projection of the gravity vector on the horizontal axis as a result of the sloping surface, and any physical horizontal motion is negligible. While this is the case for our data, where the ice floe is much larger than the wavelength, it remains to be seen whether the same relation will hold for IMUs on much smaller floes. For example, Fox and Haskell (2001) observed negligible horizontal acceleration on ice floes of approximately 7–9 m in diameter. As these floes are much smaller than their range of observed wavelength of approximately 50 m to several hundred meters, the floes are expected to follow the orbital motion of the waves. Therefore, the physical acceleration caused by the orbital motion may cancel the aliasing of the gravity vector due to the surface slope, as it is expected to be equal in magnitude and opposite in sign as shown in (17)–(19).

Since the horizontal acceleration is shown to be equivalent to the slope, we presented a method to estimate the reflection and directional spread using a rotary spectra technique (Gonella 1972). The rotary spectra method is compared with directional estimates obtained using the method of Longuet-Higgins et al. (1963) using different weighting functions. The first weighting function is using the truncated Fourier series, which assumes that the effects from the higher-order spectra are negligible but can give

negative energy at angles around $\pm 90^\circ$ from the principal direction of propagation. The second weighting function is the one presented by Longuet-Higgins et al. (1963), which arbitrarily widens the spectra but has the advantage of ensuring that the directional spectral energy is positive for all directions. Although both methods have different spectral shapes, both are found to be consistent with the rotary spectra when projected onto the axis of propagation and integrated over each hemisphere, that is, $-\pi/2 < \psi < \pi/2$ for the propagating wave and $-\pi/2 < \psi - \pi < \pi/2$ for the reflected component. This result suggests that the difference between the two weighting functions is minimal for such a coarse directional resolution.

Our examples consisted of unimodal or bimodal seas where the modes are about 180° apart, and the rotary spectrum is naturally suited for such scenarios but in more complicated multimodal seas; therefore, it is likely that the method may not perform as well. For instance, since the principal direction is determined from the time series by locating the direction that maximizes the along-wave variance, this will find the mean direction associated with the peak of the wave spectra, and not for each frequency band. It may be possible to devise a metric of “multimodalness,” which investigates the symmetry in the cross-wave direction and asymmetry in the along-wave direction, as our observations (Fig. 3) suggest this to be the case for our predominantly unimodal or bimodal seas. Our comment on this is primarily speculation, as our data does not contain such complicated wave fields. Further research is required to investigate the possibility of extending our method to multimodal seas.

The reflection coefficient is calculated using both the rotary spectra and the estimated directional spectra. The calculated reflection coefficients are similar for the three cases using the two methods, with the wider directional distribution D_2 giving slightly larger values, presumably from the spread of energy to angles greater than 90° from the principal direction of propagation. A derivation for the reflection coefficient is presented that is model independent, in that it can be directly calculated from the Fourier coefficients. This model-independent reflection coefficient compares favorably with the estimates other than D_2 , especially when the directional spread is small, that is, near the spectral peak.

Estimates of the directional spread using rotary spectra compared well with the model-independent estimates of Kuik et al. (1988) when proper scaling factors were applied to give the same isotropic limit. The isotropic limit using rotary spectra is $\sigma_r = \pi/2 = 90^\circ$, while the isotropic limits for the other methods are $\sigma_1 = \sqrt{2} \approx 81^\circ$, $\sigma_2 = \sqrt{2}/2 \approx 41^\circ$, and the rms deviation is $\sigma_D = \pi/\sqrt{3} \approx 104^\circ$. While it is expected that $\sigma_1 = \sigma_2 = \sigma_D$ for small directional spreads (Kuik et al. 1988), we found the isotropic scaling to be

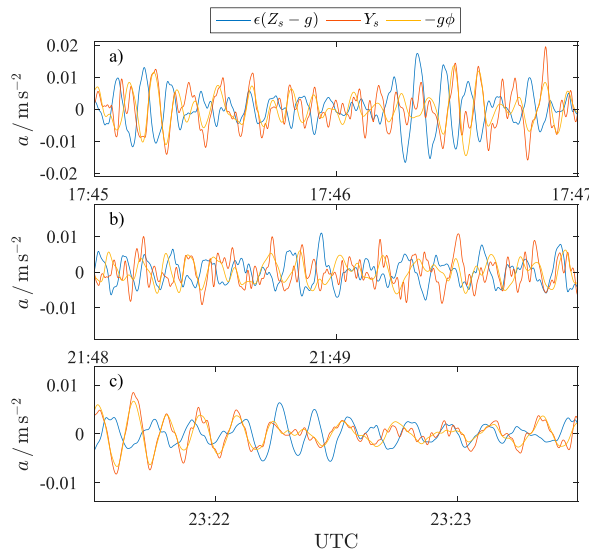


FIG. A1. Acceleration in the cross-wave direction measured in the sensor frame of reference for (a) case a, (b) case b, and (c) case c. Horizontal acceleration measured in the IMU reference frame is predominantly due to the projection of the gravity vector with ϵ estimated to be about $\sqrt{0.1} \approx 0.3$ for illustrative purposes.

necessary for the estimates to be consistent in our data. This type of scaling, based on the isotropic limit, was also employed by Squire and Montiel (2016) in order to relate the spread estimates of the marginal ice zone model of Montiel et al. (2016) with the field observations of Wadhams et al. (1986). In addition, our observations of wave spreading near the peak frequency were consistently around 30° , which is similar to the spread calculated by Wadhams et al. (1986) in the marginal ice zone. It is not clear to us why scaling the directional spread by the isotropic limits gives consistent results between the various methods, as near the spectral peak the directional spreads are much less than the isotropic limit and our previous analysis (section 4) suggests that the wave propagation is predominantly in one direction. This is somewhat troubling—that different methodologies give such different results—and care must be taken when using measurements of directional spread.

Our observations of surface waves under sea ice suggest that the linear accelerations measured in the IMU frame of reference can be related to the angular motion and vice versa in the case of long-crested waves traveling through pack ice (Liu and Mollo-Christensen 1988; Ardhuin et al. 2016). This simplifies the sensors necessary to measure the directional aspects of surface waves, which could lead to a further reduction in cost, both in terms of number of sensors and amount of data that needs to be recorded and/or transmitted. In situations where the horizontal acceleration is not negligible, the

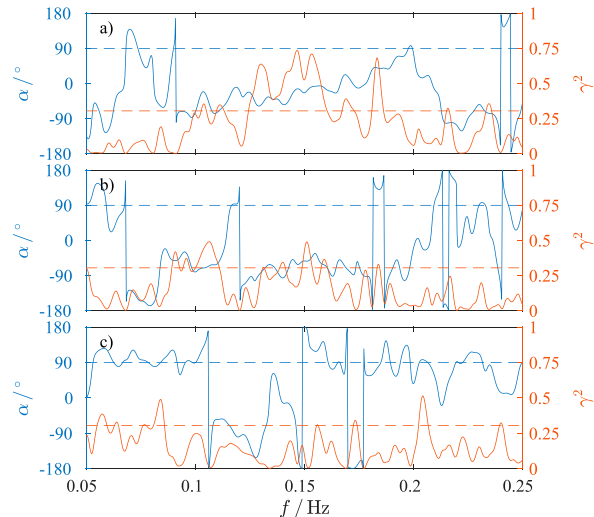


FIG. A2. Phase angle and correlation measured in the sensor reference frame for (a) case a, (b) case b, and (c) case c. Blue line shows the phase angle between $Z_S - g$ and Y_S , and the blue dashed line shows a phase difference of 90° . The red line shows the coherence squared, and the red dashed line indicates the 99.9% probability of rejecting the null hypothesis.

rotary method may still be valid as long as additional data are recorded, for example, the angle about the three orthogonal axes and the floe response to the incident wave. This difficulty suggests that a multisensor approach will be necessary to measure the wave field in a variety of sizes and shapes of sea ice.

Acknowledgments. The authors are grateful to Aleksey Marchenko for his help with the field work in Tempelfjorden and during the *Lance* cruise. We also thank Brian Ward, Kai Christensen, Trygve Halsne, Erika Lindström, and Olav Gunderson for their help during the Tempelfjorden study, and Benjamin Hergoualc'h for his work deploying the sensors during the *Lance* study. Funding for the experiment was provided by the Research Council of Norway under the PETROMAKS2 scheme (Grant 233901). The data are available from the corresponding author upon request.

APPENDIX

Cross-Wave Coherence

In addition to the along-wave propagation, the propagation in the cross-wave direction is also investigated. Figure A1 shows that the acceleration and the cross-wave slope follow each other reasonably well for all three cases, with the best agreement occurring for case c. The vertical acceleration is scaled by 0.3 for visualization purposes.

In the same manner for the along-wave propagation, the coherence and phase difference is calculated for the vertical and horizontal motion in the cross-wave direction and is shown in Figure A2. The coherence is much smaller than for the along-wave motion with only one case showing coherence at the 99.9% confidence interval. This is in contrast to Eqs. (18) and (19), which suggests that physical motions and/or noise are present that are at least similar in magnitude to the aliased gravity vector due to the cross-wave slope.

REFERENCES

- Amos, D., and L. Koopmans, 1963: *Tables of the Distribution of the Coefficient of Coherence for Stationary Bivariate Gaussian Processes*. Sandia Corporation Monogr., No. SCR-483, Sandia Corporation, 328 pp.
- Ardhuin, F., P. Sutherland, M. Doble, and P. Wadhams, 2016: Ocean waves across the Arctic: Attenuation due to dissipation dominates over scattering for periods longer than 19 s. *Geophys. Res. Lett.*, **43**, 5775–5783, doi:10.1002/2016GL068204.
- Bender, L. C., III, N. L. Guinasso Jr., J. N. Walpert, and S. D. Howden, 2010: A comparison of methods for determining significant wave heights—Applied to a 3-m discus buoy during Hurricane Katrina. *J. Atmos. Oceanic Technol.*, **27**, 1012–1028, doi:10.1175/2010JTECH0724.1.
- Benoit, M., 1992: Practical comparative performance survey of methods used for estimating directional wave spectra from heave-pitch-roll data. *Coastal Engineering 1992: Proceedings of the Twenty-Third International Conference*, B. L. Edge, Ed., Vol. 1, American Society of Civil Engineers, 62–75, doi:10.1061/9780872629332.005.
- Doble, M. J., and P. Wadhams, 2006: Dynamical contrasts between pancake and pack ice, investigated with a drifting buoy array. *J. Geophys. Res.*, **111**, C11S24, doi:10.1029/2005JC003320.
- Earle, M. D., 1996: Nondirectional and directional wave data analysis procedures. NDBC Tech. Doc. 96-01, 37 pp.
- Fox, C., and T. G. Haskell, 2001: Ocean wave speed in the Antarctic marginal ice zone. *Ann. Glaciol.*, **33**, 350–354, doi:10.3189/172756401781818941.
- , —, and H. Chung, 2001: Dynamic, in situ measurement of sea-ice characteristic length. *Ann. Glaciol.*, **33**, 339–344, doi:10.3189/172756401781818086.
- Gonella, J., 1972: A rotary-component method for analysing meteorological and oceanographic vector time series. *Deep-Sea Res. Oceanogr. Abstr.*, **19**, 833–846, doi:10.1016/0011-7471(72)90002-2.
- Kohout, A. L., B. Penrose, S. Penrose, and M. J. M. Williams, 2015: A device for measuring wave-induced motion of ice floes in the Antarctic marginal ice zone. *Ann. Glaciol.*, **56**, 415–424, doi:10.3189/2015AoG69A600.
- Kuijk, A., G. P. Van Vledder, and L. Holthuijsen, 1988: A method for the routine analysis of pitch-and-roll buoy wave data. *J. Phys. Oceanogr.*, **18**, 1020–1034, doi:10.1175/1520-0485(1988)018<1020:AMFTRA>2.0.CO;2.
- Lawson, L. M., and R. B. Long, 1983: Multimodal properties of the surface-wave field observed with pitch-roll buoys during GATE. *J. Phys. Oceanogr.*, **13**, 474–486, doi:10.1175/1520-0485(1983)013<0474:MPOTSW>2.0.CO;2.
- Liu, A. K., and E. Mollo-Christensen, 1988: Wave propagation in a solid ice pack. *J. Phys. Oceanogr.*, **18**, 1702–1712, doi:10.1175/1520-0485(1988)018<1702:WPIASI>2.0.CO;2.
- Long, R. B., and K. Hasselmann, 1979: A variational technique for extracting directional spectra from multi-component wave data. *J. Phys. Oceanogr.*, **9**, 373–381, doi:10.1175/1520-0485(1979)009<0373:AVTFED>2.0.CO;2.
- Longuet-Higgins, M. S., D. E. Cartwright, and N. D. Smith, 1963: Observations of the directional spectrum of sea waves using the motions of a floating buoy. *Ocean Wave Spectra: Proceedings of a Conference*, Prentice-Hall, 111–136.
- Marchenko, A., 1999: The floating behaviour of a small body acted upon by a surface wave. *J. Appl. Math. Mech.*, **63**, 471–478, doi:10.1016/S0021-8928(99)00059-3.
- , E. Morozov, and S. Muzylev, 2013: Measurements of sea-ice flexural stiffness by pressure characteristics of flexural-gravity waves. *Ann. Glaciol.*, **54**, 51–60, doi:10.3189/2013AoG64A075.
- Masson, D., and P. LeBlond, 1989: Spectral evolution of wind-generated surface gravity waves in a dispersed ice field. *J. Fluid Mech.*, **202**, 43–81, doi:10.1017/S0022112089001096.
- Meylan, M., and V. A. Squire, 1994: The response of ice floes to ocean waves. *J. Geophys. Res.*, **99**, 891–891, doi:10.1029/93JC02695.
- Montiel, F., V. Squire, and L. Bennetts, 2016: Attenuation and directional spreading of ocean wave spectra in the marginal ice zone. *J. Fluid Mech.*, **790**, 492–522, doi:10.1017/jfm.2016.21.
- Rabault, J., G. Sutherland, B. Ward, K. H. Christensen, T. Halsne, and A. Jensen, 2016: Measurements of waves in landfast ice using inertial motion units. *IEEE Trans. Geosci. Remote Sens.*, **54**, 6399–6408, doi:10.1109/TGRS.2016.2584182.
- , —, O. Gundersen, and A. Jensen, 2017: Measurements of wave damping by a grease ice slick in Svalbard using off-the-shelf sensors and open-source electronics. *J. Glaciol.*, **63**, 372–381, doi:10.1017/jog.2017.1.
- Squire, V. A., 2007: Of ocean waves and sea-ice revisited. *Cold Reg. Sci. Technol.*, **49**, 110–133, doi:10.1016/j.coldregions.2007.04.007.
- , and F. Montiel, 2016: Evolution of directional wave spectra in the marginal ice zone: A new model tested with legacy data. *J. Phys. Oceanogr.*, **46**, 3121–3137, doi:10.1175/JPO-D-16-0118.1.
- , J. P. Dugan, P. Wadhams, P. J. Rottier, and A. K. Liu, 1995: Of ocean waves and sea ice. *Annu. Rev. Fluid Mech.*, **27**, 115–168, doi:10.1146/annurev.fl.27.010195.000555.
- Sutherland, G., and J. Rabault, 2016: Observations of wave dispersion and attenuation in landfast ice. *J. Geophys. Res. Oceans*, **121**, 1984–1997, doi:10.1002/2015JC011446.
- Tucker, M. J., and E. G. Pitt, Eds., 2001: *Waves in Ocean Engineering*. Vol. 5. Elsevier, 550 pp.
- VectorNav, 2014: VN-100 user manual. Version 2.05, VectorNav Technologies, 128 pp.
- Vindegg, C. M., 2014: Stress measurements in landfast sea ice in Van Mijenfjorden, Svalbard: A survey of internal stress in landfast sea ice winter 2014. Ph.D. thesis, Norwegian University of Science and Technology, 73 pp.
- Wadhams, P., V. A. Squire, J. A. Ewing, and R. W. Pascal, 1986: The effect of the marginal ice zone on the directional wave spectrum of the ocean. *J. Phys. Oceanogr.*, **16**, 358–376, doi:10.1175/1520-0485(1986)016<0358:TEOTMI>2.0.CO;2.
- , —, D. J. Goodman, A. M. Cowan, and S. C. Moore, 1988: The attenuation rates of ocean waves in the marginal ice zone. *J. Geophys. Res.*, **93**, 6799–6818, doi:10.1029/JC093iC06p06799.
- Yiew, L., L. Bennetts, M. Meylan, B. French, and G. Thomas, 2016: Hydrodynamic responses of a thin floating disk to regular waves. *Ocean Modell.*, **97**, 52–64, doi:10.1016/j.ocemod.2015.11.008.
- Young, I., 1994: On the measurement of directional wave spectra. *Appl. Ocean Res.*, **16**, 283–294, doi:10.1016/0141-1187(94)90017-5.

2.4 Publication 4: Field observations and preliminary investigations of a wave event in solid drift ice in the Barents Sea

Marchenko, A., Rabault, J., Sutherland, G., Collins, C. O. I., Wadhams, P., and Chumakov, M. (2017), "Field observations and preliminary investigations of a wave event in solid drift ice in the Barents Sea", In *24th International Conference on Port and Ocean Engineering under Arctic Conditions*.

Field observations and preliminary investigations of a wave event in solid drift ice in the Barents Sea

Aleksey Marchenko¹, Jean Rabault², Graigory Sutherland², Clarence O. Collins III³,
Peter Wadhams⁴, Mikhail Chumakov⁵

¹The University Centre in Svalbard, Longyearbyen, Norway

²University of Oslo, Oslo, Norway

³Naval Research Laboratory, Stennis Space Center, Hancock County, Mississippi, USA

⁴Univetsity of Cambridge, Cambridge, UK

⁵Gazprom VNIIGAZ LLC, Moscow, Russia

ABSTRACT

Waves propagating below drift ice were observed in the North-West Barents Sea. In-situ measurements of ice and water characteristics were performed with the equipment deployed on the ice and in the water below the ice during 16 hours from 16:00, May 1, to 08:00, May 2, 2016. Peak frequencies of the observed waves were around 0.35 rad/s, 0.5 rad/s, 0.6 rad/s and 0.8 rad/s. It is found that the eddy viscosity in the boundary layer below the ice has a mean value of 140 cm²/s with significant variations correlated with the floe acceleration. Spectral properties of the observed waves are compared with the results of the WaveWatch III model. The origin of the observed waves is discussed in the paper.

KEY WORDS: waves, ice, turbulence, drift

INTRODUCTION

Propagation of wind waves and swell in ice covered regions can influence the break up of drift ice into small floes in a span of a few hours over relatively large areas. At the same time, drift ice influences damping of surface waves and prevents their propagation over long distances in ice covered regions. In regions of offshore activities, broken ice and icebergs accelerated by waves create risks to human activities. Investigation of wave interaction with ice is of interest for the development of human activity in the Barents Sea. There are regions where the water is consistently covered by solid drift ice in the winter time and other regions which are exposed to stronger wave action with rare occurrences of drift ice. Collins et al (2015) described details of ice break up in the Barents Sea due to the penetration of storm waves from open waters.

An analysis of some previous in-situ measurements of wave characteristics in ice covered regions of the Barents Sea is presented by Marchenko et al, 2015. Measurements were performed with an Acoustic Doppler Velocimeter (ADV, SonTek 5MHz Ocean Probe) deployed on the drift ice in a downward looking position and a Directional Waverider buoy deployed on top of the ice. Typical periods of waves observed below the drift ice were 10-12 s. The results of ADV measurements gave the possibility to calculate the eddy viscosity in the under-ice boundary layer. According to Liu and Mollo-Christensen (1988) the eddy viscosity influences wave damping. Field measurements have shown great variability of the eddy viscosity from very small values of about $0.002 \text{ cm}^2/\text{s}$ to $100 \text{ cm}^2/\text{s}$ (Marchenko et al, 2015). The high values of the eddy viscosity were found from the analysis of field data collected near Edgeøya. The increase of the eddy viscosity is explained by the influence of non-stationary ice drift on the surface water layer. Representative damping distance for a swell with period of ten seconds is 10-20 km when the eddy viscosity is about $100 \text{ cm}^2/\text{s}$. Wind waves with periods of 5-6 s dampen over shorter distance and, therefore, were never observed in solid ice.

Previously, Marchenko et al (2013) introduced a method for wave measurement from the ice with two pressure recorders SBE-39 mounted on the same wire at different depths. The method was used to register waves propagating from the front of Tuna glacier due to calving events. Rabault et al (2016) constructed instruments based on Inertial Motion Units (IMUs) and used them for the registration of surface waves penetrating below the ice from the open water in Templefjorden in Spitsbergen. The IMUs were configured to output acceleration and angular rate at 10Hz. In May 2016 all sensors previously cited, including the ADV, SBE-39 and 10 IMUs were deployed on the drift ice near Edgeøya and registered wave characteristics synchronously during 16 hours. In the present paper we described and analyze the results of those field measurements, and compare the output from the different processing methods.

LOCATION AND ORGANIZATION OF THE FIELDWORK

Fieldwork was performed on the drift ice near Edgeøya in the North-West Barents Sea (Fig. 1a). The geographical coordinates are 77.76°N , 25.5°E . Sea depth in the region was measured around 160 m. RV Lance was moored to a floe of thickness around 30 cm and diameter around 2 km (Fig. 1b). The floe mass is estimated between $7 \cdot 10^5$ tons and $8 \cdot 10^5$ tons. The mass of the fully loaded Lance is $M_L=2370$ tons, and her length and breadth are around $L_L=60\text{m}$ and $w_L=12\text{ m}$. Therefore the influence of the Lance on the floe dynamics is small. The frequency of natural oscillations of the Lance is estimated from the formula $\omega_L^2=\rho_w g S_L/M_L$, where ρ_w is the water density, g is the gravity acceleration, and $S_L=w_L L_L$. We find a natural frequency of $\omega_L \approx 1.7 \text{ rad/s}$, i.e. a period $T_L \approx 3.5 \text{ sec}$. This is outside of the range of wave frequencies, and therefore cannot be mistaken for incoming water waves.

The equipment was deployed on the floe in the afternoon of May 01, 2016, and wave measurements started from 16:00, May 01 (here and further UTC is used), and extended until 09:00, May 02. The equipment consists of the pressure and temperature recorders SBE 39, Acoustic Doppler Velocimeter SonTek Ocean Probe 5 MHz (ADV), Ice tracker Oceanetic Measurement (model 703 equipped with anemometer) and Inertial Motion Units (IMUs) from Vectornav (VN100). SBE 39 were fixed on a steel wire on the depths 3.6 m and 11.4 m, and the wire was mounted on the ice (Fig. 2a). The ADV probe is equipped with tiltmeter and

compass. Magnetic inclination is about 15° in the region and is taken into account during data processing. The ADV was mounted on a vertical wooden pole fixed on the ice with a tripod (Fig. 2a). Velocity measurements were performed at a depth of 80 cm below the ice. The depth is measured by the ADV pressure sensor. SBEs were deployed around 16:00, May 01, and recovered around 09:00, May 02. The ADV sensor was deployed on 19:00, May 01, and around 04:30, May 02, it was disconnected from the electric power source on the Lance board because of the floe motion relatively the ship. The ice tracker was deployed on the floe around 11:00 and sent data via Iridium during one month. The positions of the 10 IMUs deployed are presented in Fig. 2b. One IMU was deployed alone, while all other IMUs were grouped into arrays of three sensors.

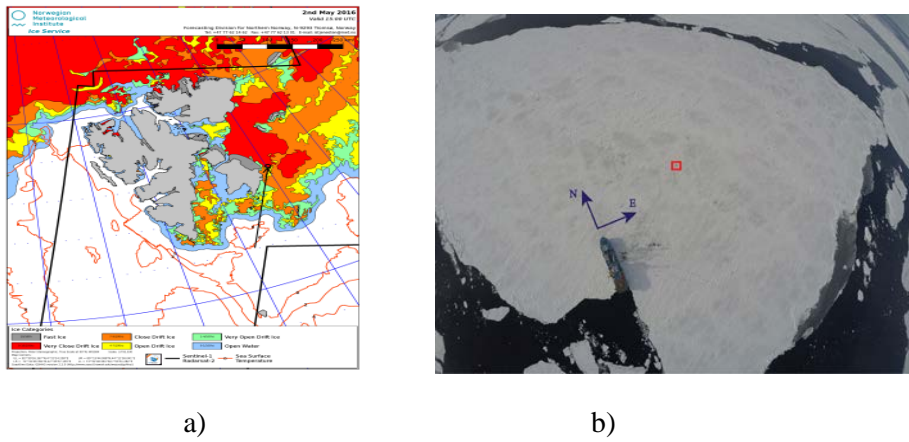


Figure 1. (a) Location of the field works near Edgeøya on May 1-2, 2016, is shown on the ice map by black circle and arrow. (b) View of RV Lance from unmanned helicopter. Red square shows location of ADV and SBE

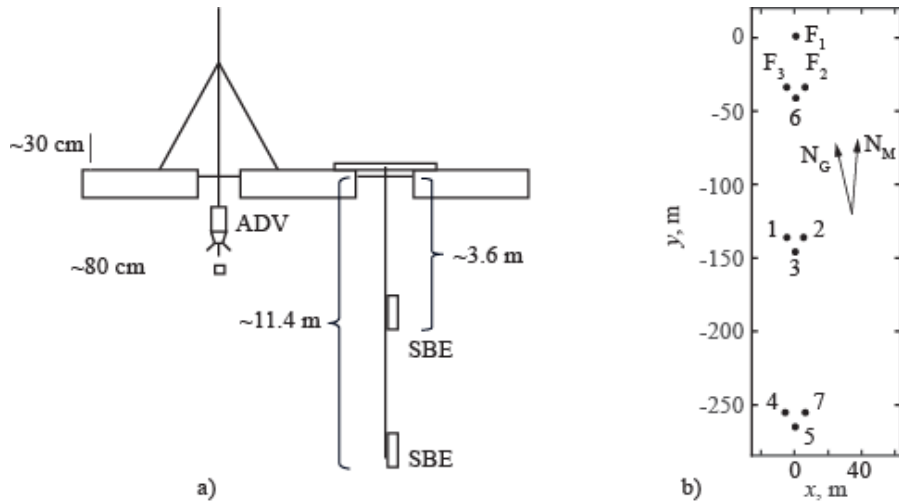


Figure 2. (a) Schematic of the deployment of ADV and SBE sensors. (b) Positions of the IMUs on the ice floe. N_M and N_G indicate the position of the Magnetic and Geographic North, respectively.

User setup for the ADV measurements is given in Table 1. SBE sensors provided continue record with sampling frequency 2 Hz. Ice tracker provided data on GPS location of the tracker, its yaw angle and local wind velocity with sampling period of 10 min. The trajectory and the drift velocity of the ice tracker are shown in Fig.. Wind velocity (Fig. 3a) didn't change significantly 16:00 UTC, May 01, to 04:00 UTC, May 02. The shape of the floe trajectory (Fig.3a) and the evolution with time of the flow velocity are explained by the influence of sea current modulated by semidiurnal tide. Evolution of the floe acceleration and yaw angle shown in Fig.4 are explained by the floe interaction with surrounding ice.

Table 1. User setups of ADV.

Sensor	Sampling frequency, Hz	Burst Interval, s	Samples per burst	Number of bursts	Depth, cm
ADV	10	360	2400	94	80

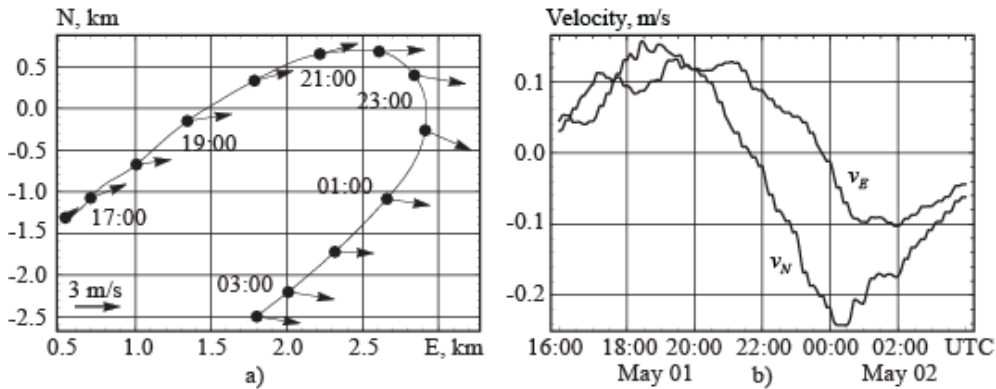


Figure 3. Trajectory (a) and drift velocity components versus the time (b) of the ice tracker deployed on the ice floe. Vectors of the wind velocity measured along the drift trajectory are shown by arrows (a).

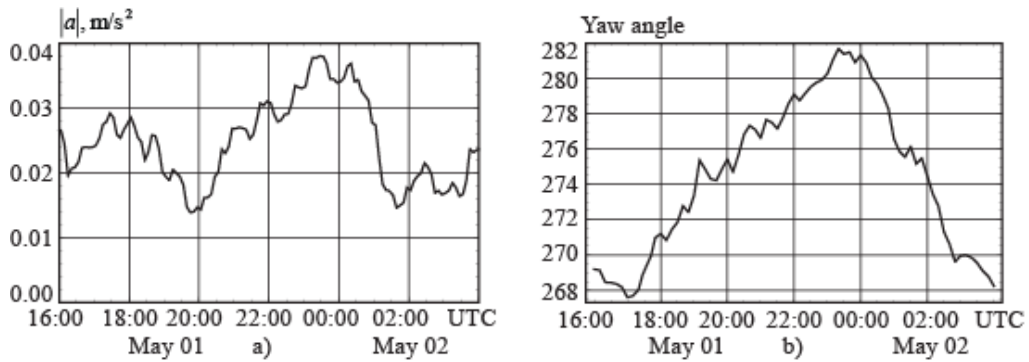


Figure 4. Absolute value of the acceleration (a) and yaw angle (b) of ice tracker deployed on the drift floe versus time.

ANALYSIS OF SBE DATA

Records of the water pressure measured by both SBE39s are shown in Fig. 5. The quality of the data recorded at 3.6 m depth before 21:00 is not sufficient to distinguish wave induced oscillations of the water pressure, but after 21:00 the oscillations are well visible (Fig. 5a). The oscillations are well visible in the pressure data recorded at 11.4 m depth from 16:00. Spectral analysis was performed with pressure fluctuations δp calculated as a difference between the pressure averaged over each consequent 5 min interval and actual pressure measured in this interval. Spectrograms (Fig. 6a) and spectrums (Fig. 7) constructed in Mathematica software show that wave spectrum has four local maxima at frequencies around 0.35 rad/s, 0.5 rad/s, 0.6 rad/s and 0.8 rad/s before 23:00, May 01, and there are only two local maxima at frequencies around 0.35 rad/s and 0.6 rad/s after 00:00, May 02. The frequency of waves with maximal energy was 0.8 rad/s before 23:00, May 01, and 0.6 rad/s after 00:00, May 02. Spectrums of the pressure fluctuations recorded at 3.6 m depth are very similar to shown in Fig.7.

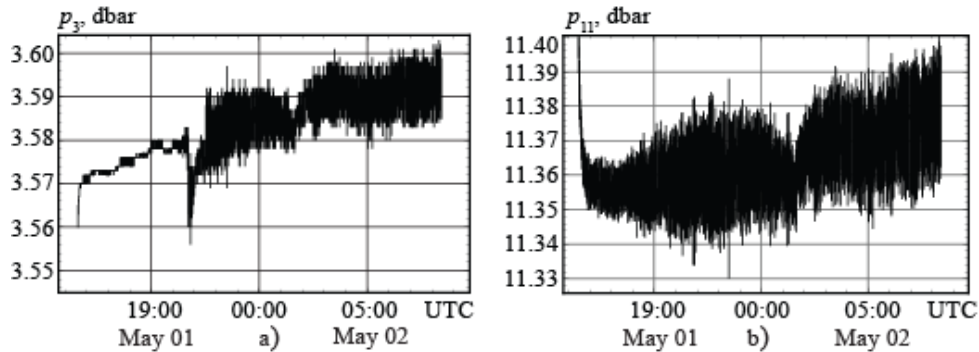


Figure 5. Records of the water pressure measured by recorders SBE39 deployed at 3.6 m (a) and 11.4 m (b) depths.

It was shown (Marchenko et al, 2013) that the ratio of wave induced pressure amplitudes measured at depths $z=z_1$ and $z=z_2$ is equal to:

$$\gamma \equiv \frac{P_{1,dyn}}{P_{2,dyn}} = \frac{\omega^2 \cosh[k(z_1 + H)] - gk \sinh[kH]}{\omega^2 \cosh[k(z_2 + H)] - gk \sinh[kH]}. \quad (1)$$

Eqn. (1) is used for the calculation of the wave number k when the wave frequency is known. We consider the Fourier transforms $\delta p_{3,f}(\omega)$ and $\delta p_{11,f}(\omega)$ of the pressure fluctuations $\delta p_3(t)$ and $\delta p_{11}(t)$ recorded at depths 3.6 m and 11.4 m. It is assumed that the ratio γ is equal to the ratio $|\delta p_{3,f}|/|\delta p_{11,f}|$, where the values of $|\delta p_{3,f}|$ and $|\delta p_{11,f}|$ are taken in the points of their local maxima shown in Fig. 6 by grey and black circles. The values of $|\delta p_{3,f}|$ and $|\delta p_{11,f}|$ in their local maxima are given in Table 2. Black dots in Fig. 8a have coordinates (k, ω) , where the values of ω are taken from Table 2, and the values of k are calculated from Eqn. (1) with the values of ω and γ calculated using Table 2. Solid line in Fig. 8a shows the dispersion relation of gravity waves propagating in the water with free surface and described by the

formula $\omega^2 = gk \cdot \tanh(kH)$ with $H=160$ m. One can see that experimental points sit on the dispersion curve. It means that the influence of ice on dispersion properties of observed waves is very small.

The last conclusion follows from the dispersion equation of flexural-gravity waves $\omega^2 = gk \cdot \tanh(kH)(1+Dk^4)$, when $Dk^4 \ll 1$. Here $D \approx Eh^3/(12\rho_w g)$, where E is the effective elastic modulus of the ice and h is the ice thickness. In-situ tests of flexural strength of floating cantilever beams performed on the drift ice on May 01 shown that $E=1.2\text{-}1.9$ GPa. Assuming $h=0.3$ m we find that $Dk^4 < 0.01$ when $k=0.07$, i.e. the influence of ice elasticity on the waves with registered frequencies is expected to be very small, in good agreement with observations.

Wave amplitude is calculated using water pressure records at depth z below the ice and the formulae:

$$\delta p_{z,f}(\omega) = \rho_w g \eta_f(\omega) P(k, z), \quad P(k, z) = \frac{\cosh[k(z+H)]}{\cosh[kH]} - 1, \quad (2)$$

where $\delta p_{z,f}$ and η_f are the Fourier images of the water pressure fluctuations $\delta p_z(t)$ at the depth z and water surface elevation $\eta(t)$ caused by waves. We used records of the water pressure at 11 m depth. Values of $\delta p_{z,f}$ were calculated using the discrete Fourier transform in Mathematica. Then the inverse Fourier transform was used to calculate water surface elevation as a function of the time separately. The procedure was realized independently for each hour of the record. Significant wave height (SWH) is calculated using the formula:

$$SWH = 4 \cdot \text{StandardDeviation}[\eta]. \quad (3)$$

Mean value of SWH was found around 10 cm.

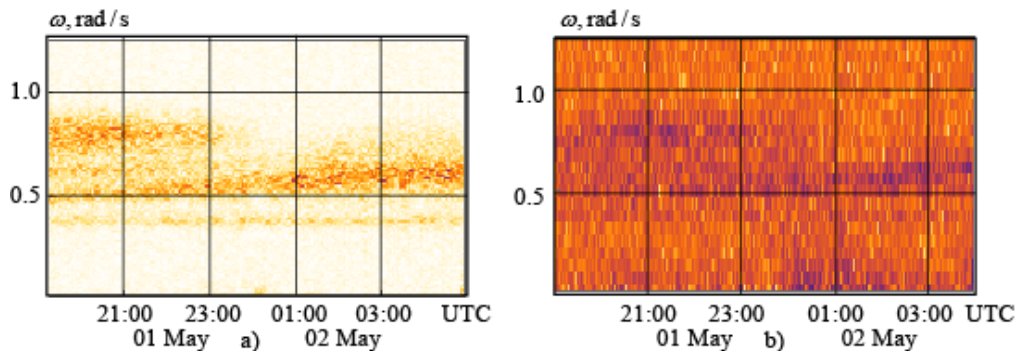


Figure 6. Spectrogram of pressure fluctuations reconstructed with SBE data recorded at 11.4 m depth (a). Spectrogram of the fluctuations of the North component of water velocity recorded by ADV (b).

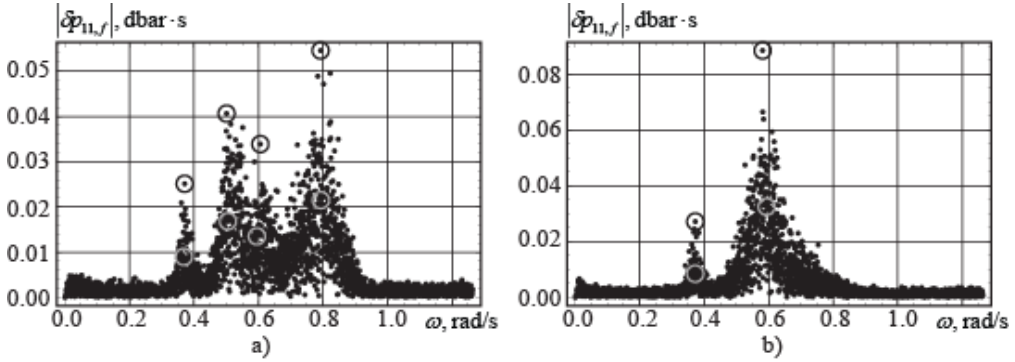


Figure 7. Spectra of water pressure fluctuations recorded at 11.4 m depth from 19:00 to 23:00, May 01, (a) and from 23:00, May 01, to 03:00, May 02, (b). Black and gray circles show spectral maxima of pressure fluctuations records at 11.4 m and 3.6 m depths.

Table 2. Local maxima of spectrums $|\delta p_{3,f}|$ and $|\delta p_{11,f}|$, dbar·s.

	19:00 to 23:00, May 01				23:00, May 01, to 03:00, May 02	
ω , rad/s	0.35	0.5	0.6	0.8	0.35	0.6
3.6 m	0.009	0.017	0.013	0.021	0.009	0.032
11.4 m	0.026	0.04	0.034	0.054	0.025	0.09

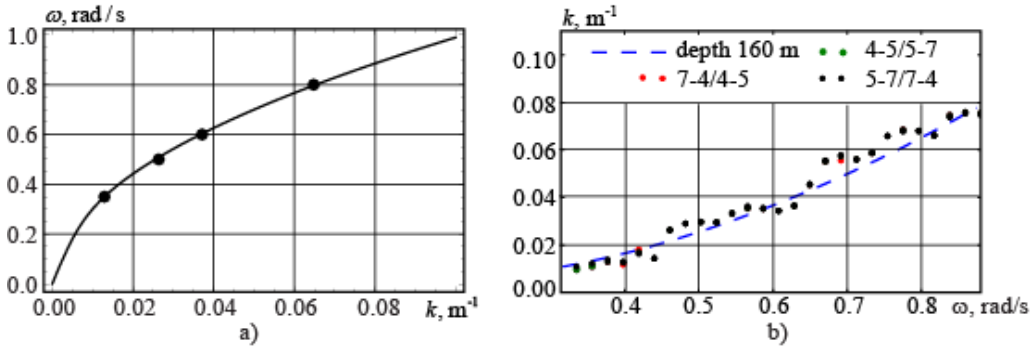


Figure 8. Dispersion relation of surface gravity waves in the water of 160 m depth. Black dots are constructed using SBE records at 3.6 m and 11.4 m depths (a). Dispersion relation obtained from the analysis of the cross correlation between IMU signals 4, 5 and 7 using Eqn. (11), at 20:00 UTC on 01/05/2016 (b).

ANALYSIS OF ADV DATA

Records of the East (v_E) and North (v_N) velocity components at 80 cm depth below the ice were used for the calculation of the eddy viscosity and the analysis of spectrums and directions of wave propagation. The velocity fluctuations in the East (δv_E) and North (δv_N)

directions were calculated for each burst of the ADV record as follows:

$$\delta v_E = v_E - \langle v_E \rangle, \quad \delta v_N = v_N - \langle v_N \rangle, \quad (4)$$

where $\langle v_E \rangle$ and $\langle v_N \rangle$ are the mean values of the East and North velocities averaged over the burst. All fluctuations were grouped in one file and used for the construction of spectrogram. The spectrogram of the fluctuations of the North velocity component is shown in Fig. 6b. It looks similar to the spectrogram constructed with the SBE data. Spectrums of δv_N are shown in Fig. 9. Spectral maxima are well visible in the spectrums of δv_N and are absent in the spectrum of δv_E from 19:00 to 23:00, May 01. The δv_N spectrum looks very similar to the spectrum shown in Fig. 7a. Fig. 9b shows spectral maxima at the frequency of 0.6 rad/s in the spectrum δv_N . There is spectral maxima in the spectrum of δv_E at the same frequency. Spectral maxima at the frequency of 0.35 rad/s appears only in the spectrum of δv_N . The velocity directions should be corrected by clockwise shift on 15° because of the magnetic inclination.

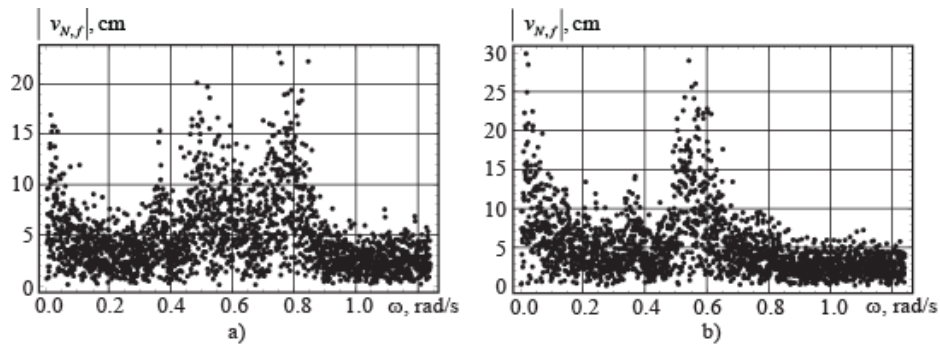


Figure 9. Spectrums of fluctuations of the North velocity component recorded from 19:00 to 23:00, May 01, (a) and from 23:00, May 01, to 03:00, May 02, (c).

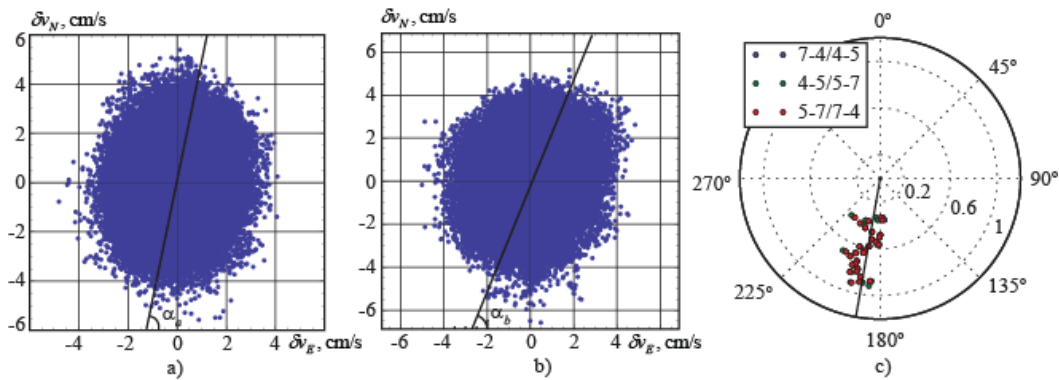


Figure 10. Hodograph of the velocity fluctuations recorded from 19:00 to 23:00, May 01, (a) and from 23:00, May 01, to 03:00, May 02, (b). (c): direction of propagation of the waves obtained from the analysis of the cross correlation between IMU signals 4, 5 and 7 using Eqn. (11), at 20:00 UTC on 01/05/2016, concentric circles indicate wave frequency rad/s). The black line indicates the direction of azimuth 190 degrees.

Each point in Fig. 10a,b corresponds to the vector of the velocity fluctuations with corrected direction. The sampling frequency is 10 Hz. From Fig. 10a it follows that dominant direction of wave propagation from 19:00 to 23:00, May 01, was from the South-West with azimuth angle $\alpha_a \approx 189.6^\circ$. Later from 23:00, May 01, to 03:00, May 02, the azimuth angle of wave propagation increased to $\alpha_b \approx 199.8^\circ$ (Fig. 10b).

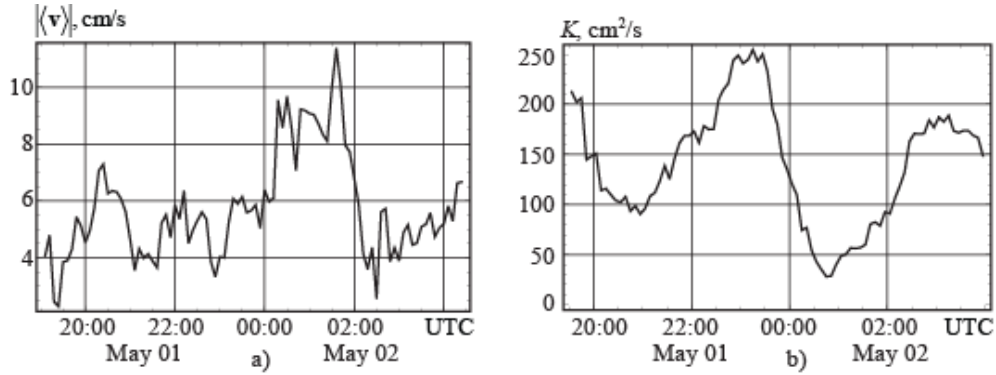


Figure 11. The mean horizontal water velocity relatively the ice (a) and the eddy viscosity (b) versus the time.

Fig. 11a shows the mean horizontal velocity of the water below the ice measured with the ADV versus the time. Fig. 11b shows the eddy viscosity versus the time. The eddy viscosity is calculated with the formula:

$$\tau = -\rho_w K \frac{\partial \langle v_h \rangle}{\partial z}, \quad (5)$$

where τ is the turbulent shear stress applied to the ice at the ice-water interface, ρ_w is the water density, $\langle v_h \rangle$ is the mean horizontal velocity of the water relative to the ice, z is the vertical coordinate, and K is the eddy viscosity.

The turbulent shear stresses applied to the ice bottom in the East and North directions are calculated with the formula of Reynolds stresses:

$$\tau_E = \rho_w \langle \delta v_E \delta w \rangle, \quad \tau_N = \rho_w \langle \delta v_N \delta w \rangle, \quad (6)$$

where δw is the fluctuation of the vertical velocity, and symbol $\langle \dots \rangle$ means the averaging over the burst. The turbulent shear stress τ in Eqn. (4) is calculated from the formula:

$$\tau = \sqrt{\tau_E^2 + \tau_N^2}. \quad (7)$$

The vertical gradient of the mean horizontal velocity of the water relatively the ice is approximated as $\|\langle v_h \rangle\|_z \approx -\langle v_h \rangle / h_{ADV}$, where $h_{ADV} = 80$ cm. The mean horizontal velocity is calculated from the formula:

$$\langle v_h \rangle = \sqrt{\langle v_E \rangle^2 + \langle v_N \rangle^2}. \quad (8)$$

From Fig. 10 it follows that K reaches a local maximum in time when $\langle v_h \rangle$ is minimal, and when the floe acceleration shown in Fig. 3a. The mean value of the eddy viscosity over is found to be $140\text{cm}^2/\text{s}$.

ANALYSIS OF IMU DATA

The signals recorded by the IMUs are of good quality, as confirmed by the example of raw data shown in Fig. 12. The PSD of the wave elevation is computed from the PSD of the wave vertical acceleration following the formula: $PSD[\eta] = \omega^{-4} PSD[\eta_{tt}]$, where η is the wave elevation. Excellent agreement is found between the shape of the PSD reported in Fig. 7a and the one reported in Fig. 12 (right), which validates both methods. Significant wave height can be obtained from the zeroth order moment of the PSD, and the results are very similar to what is obtained from Eqn. (3), with a maximum value of around 12 cm.

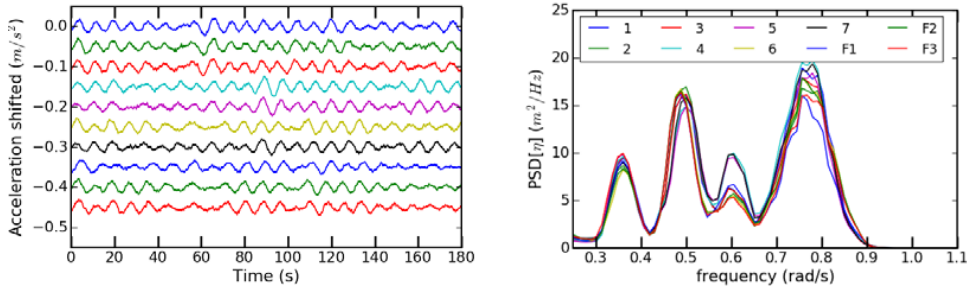


Figure 12. Left: sample of the raw signal for vertical acceleration recorded by all 10 IMUs starting at UTC time 20:00:00.000 on 01/05/2016 (vertical offsets are used for ease of visualization). Right: PSD of wave elevation computed for the 10 IMUs at the same time as presented in Figure 7 (a), using Welch method on 30 minutes intervals with 75% overlap.

The signals obtained by each set of 3 sensors grouped together can be used to perform a 2D cross-correlation analysis, extending what was presented by Sutherland and Rabault (2016). The normalized cross-spectral density is computed between adjacent sensors as:

$$C_{xy} = \frac{|S_{xy}|^2}{S_{xx}S_{yy}}, \text{ with } S_{xy}(f) = \frac{1}{2\pi} \sum_{n=-N/2}^{n=N/2} R_{yx}(n) e^{-j2\pi fn}, \quad (9)$$

where $R_{xy}(n)$ is the cross-correlation between the discrete signals $x(n)$ and $y(n)$. The phase shift of the waves between two adjacent sensors is then computed at all frequencies for which the coherence is significant with a probability higher or equal to 95%, following the formula:

$$\phi_{xy}(f) = \arctan 2 \left(\frac{\text{Im}[S_{yx}(f)]}{\text{Re}[S_{yx}(f)]} \right). \quad (10)$$

Typical outputs from this method are presented in Fig. 13.

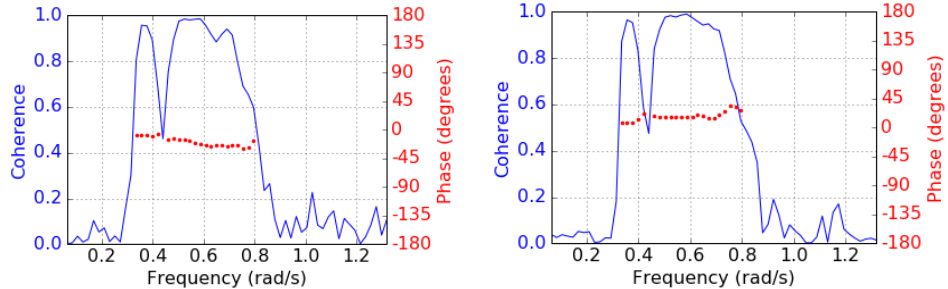


Figure 13: coherence and phase shift of the wave acceleration recorded between sensors F2 and F3 (left) and F3 and 6 (right). Coherence is computed based on a 45 minute interval, with 75 percent overlap between segments.

The phase shift between adjacent sensors is related to the incoming waves through the relation: $\phi_{ij}(f) = \vec{k}(f) \cdot \vec{x}_{ij}$ (Eqn. 11), where $\vec{k}(f)$ is the incoming wave vector at frequency f and \vec{x}_{ij} is the vector from IMU i to IMU j. Therefore, the two dimensional wave vector can be obtained at each frequency using the phase shift from two sides of a triangle of sensors and elementary trigonometry. This gives access to both the direction of the incoming waves and the dispersion relation. An example of the results of such analysis is presented in Fig. 8b and Fig. 10c. Similar to what is presented in Fig. 8a,b, the waves are found to follow the deep water dispersion relation and the effect of the ice is negligible. The direction of propagation of the waves is also in very good agreement with the results presented in Fig. 10a.

COMPARISON WITH NUMERICAL SIMULATIONS

Wave frequency and wave direction of propagation were obtained from the web (<https://earth.nullschool.net>), where the results of modeling with WaveWatch III are provided. Fig. 14 shows that there are two wave systems coming to Spitsbergen from South-West and from South-East. The white line in Fig. 14 marks the boundary between them. Waves coming from the South-West have periods around 10 sec, and waves coming from the South-East have periods around 6.3 sec near Spitsbergen. According to WaveWatch III, the dominant wave period and direction of propagation at the point (76.93 N, 21.60 E) is shown in Fig. 14 by a white circle were 8.4 s and 210° on 22:00, May 01, and 10.1 s and 205° on 02:00, May 2. Frequencies of waves in the region extended to the East from the marked location are around 5-6 sec. Spectra in Fig. 7 show the dominant wave frequency to be 0.8 rad/s (wave period 7.8 sec) before 23:00, May 01, and 0.6 rad/s (wave period 10.4 s) after 23:00, May 01. Thus the waves observed propagate from the South-West along the shore of Edgeøya. The ice map in Fig. 1a shows green and yellow regions of very open drift ice which extended along Edgeøya. The waves arrive at the observation site following this route.

CONCLUSIONS

In-situ records of water and ice characteristics are performed on the drift floe in the North-

West Barents Sea during wave propagation event of 16 hours duration. The ice floe of 30 cm thickness was cyclically bended by waves with an amplitude of several centimeters and was not broken. Spectral analysis has shown the existence of local spectral maxima at the frequencies 0.35 rad/s, 0.5 rad/s, 0.6 rad/s and 0.8 rad/s. Dominant waves with frequencies 0.6 rad/s and 0.8 rad/s propagated from South-West along the Edgeøya shoreline. Several measurement methods are presented and validated against each other, including direct measurement of the dispersion relation and of the direction of propagation of waves.

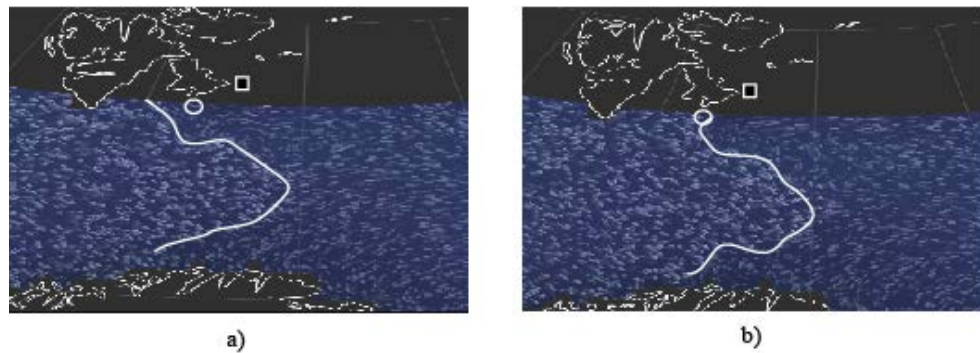


Figure 14. Results from simulations performed by WaveWatch III. Direction of wave propagation are indicated at 22:00, May 01, (a), and 02:00, May 02 (b).

ACKNOWLEDGEMENTS

The authors wish to acknowledge the support of the Research Council of Norway through the SFI SAMCoT, Petromaks2 project Experiments on waves in oil and ice, and NORRUS project Field studies and modelling of sea state, drift ice, ice actions and methods of icebergs management on the Arctic shelf. The help of Masters Student Benjamin Hergoualch in deploying the IMUs is gratefully acknowledged.

REFERENCES

1. Collins, C.O., Rogers, W.A., Marchenko, A., Babanin, A.V., 2015. In situ measurements of an energetic wave event in the Arctic marginal ice zone. *Geophys. Res. Letters*, 42, 6, 1863-1870.
2. Liu, A. K. and E. Mollo-Christensen, 1988. Wave propagation in a solid ice pack, *J. Phys. Oceanogr.*, 18(11), 1702-1712.
3. Marchenko, A.V., Morozov, E.G., Muzylev, S.V., 2013. Measurements of sea-ice flexural stiffness by pressure characteristics of flexural-gravity waves. *Annals of Glaciology*, 54(64), 51-60.
4. Marchenko, A.V., Gorbatsky, V.V., Turnbull, I.D., 2015. Characteristics of under-ice ocean currents measured during wave propagation events in the Barents Sea. POAC15-00171, Trondheim, Norway.
5. Rabault, J., Sutherland, G., Ward, B., Christensen, K.H., Halsne, T., Jensen, A., 2016. Measurements of Waves in Landfast Ice using Inertial Motion Units. *IEEE Transactions on Geoscience and Remote Sensing*, 54(11), 6399-6408.
6. Sutherland, G., Rabault, J., 2016. Observation of wave dispersion and attenuation in land fast ice. *Journal of Geophysical Research, Oceans*, 121, 3, 1984-1997.

2.5 Publication 5: PTV investigation of the mean drift currents under water waves

Rabault, J., Halsne, T., Sutherland, G., and Jensen, A. (2016), "PTV investigation of the mean drift currents under water waves", In *Proceedings of the 18th Int. Lisb. Symp.*

PTV investigation of the mean drift currents under water waves

J. Rabault^{1,*}, T. Halsne¹, G. Sutherland¹, A. Jensen¹

1: Department of Mathematics, University of Oslo, Norway

* Correspondent author: jeanra@math.uio.no

Keywords: PTV processing, Water waves, Mean flow profiles

ABSTRACT

The mean drift induced by water waves generated in a wave tank is investigated using Particle Tracking Velocimetry (PTV). Two situations are investigated, one with a clean free water surface and the other one with a thin latex cover (thickness 0.25 mm) that modifies the boundary condition at the water surface. We observe the onset of a recirculation flow under the waves as soon as the wave front goes past the measurement position. The presence of a cover distorts the mean drift, as predicted analytically in [1].

1. Introduction

The damping effect of a thin oil cover on water waves has been known since the ancient Greeks and interested scientists such as Benjamin Franklin, Osborne Reynolds and Horace Lamb [2]. The details of the damping mechanism and induced currents generated remain, still today, a subject of research. The effect of a cover on surface waves propagation, damping and mean currents has been studied for over five decades theoretically, in the laboratory and in the field [1, 3, 4, 5]. Understanding the interaction between surface waves and oil slicks or sea ice covers is a topic of interest for a variety of purposes such as formulation of ocean models for climate, weather and sea state prediction [6], and the analysis of pollution dispersion in the Arctic environment [7]. Unfortunately our knowledge of the underlying phenomena is still partial as pointed out by the difficulties encountered when trying, for example, to model climate and ice extent evolution [8]. In addition, measuring the effect of a cover on induced currents is made challenging, even in the laboratory, by the difficulty of observing mean flows under surface gravity waves [9].

In the present paper we report Particle Tracking Velocimetry (PTV) investigation of the mean drift induced by water waves generated in a wave tank with and without cover. We observe a recirculation effect corresponding to a zero integrated mass flow over the water column as soon as the wave front goes past the measurement position. The presence of a cover distorts the mean drift, which corresponds to the theory presented in [1].

2. Mean drift under water waves

It has been known since the work of Stokes [10, 11] that the potential flow solution for water waves results in a net forward motion of the fluid particles. This effect, called for Stokes drift, arises from the fact that the orbits of the fluid particles are not closed at the order $O(\epsilon^2)$ where $\epsilon = ak$ is the wave steepness, a the wave amplitude and k the wave number. The resulting net forward motion is:

$$u_s(z) = \omega a^2 k e^{2kz} \quad (1)$$

with ω the wave angular frequency, and z the depth in the water column. However, observing the Stokes drift has proven challenging, even in controlled wave tank experiments [9]. A first reason explaining the difficulty of observing the Stokes drift lies in the residual motions present in any experiment, that arise from recirculation flows generated by previous experiments and particle seeding. Moreover, Eqn. (1) describes the steady state solution corresponding to waves propagating in infinitely deep water, in an infinitely long wave tank, with a perfectly clean water surface, which does not correspond to any realistic configuration. Finally, a recirculation flow is generated as soon as the wave front passed the observation position [9]. There is, to the authors' knowledge, no theory describing the transient velocity field under a wave front.

Similarly to experiments previously reported in the literature [9], bad agreement was initially found by the authors between the Stokes drift and the observed mean drift without a cover. Therefore, an ad hoc modified Stokes drift is introduced, that yields better agreement with our experimental data. The corresponding modified Stokes drift is obtained by adding a parabolic velocity profile, that goes to zero at the water surface and wave tank bottom, which velocity magnitude allows to recover a zero mass flow condition. The obtained modified Stokes drift is defined as:

$$u_{sm}(z) = u_s(z) + 6Qz/h^2 + 6Qz^2/h^3 \quad (2)$$

with h the water depth, and $Q = \int_{-h}^0 u_s(z) dz$ the integrated mass flow associated with the Stokes drift.

In the presence of a cover enforcing no slip boundary condition for the wave Eulerian velocity at the water surface, vorticity diffuses from the water surface into the lower parts of the fluid which creates an additional source of mean flow motion. The resulting mean flow motion depends in a complex fashion on wave frequency and on a nondimensional elasticity parameter, E , as defined in [1]. Mean profiles corresponding to the steady solution in a wave tank obtained

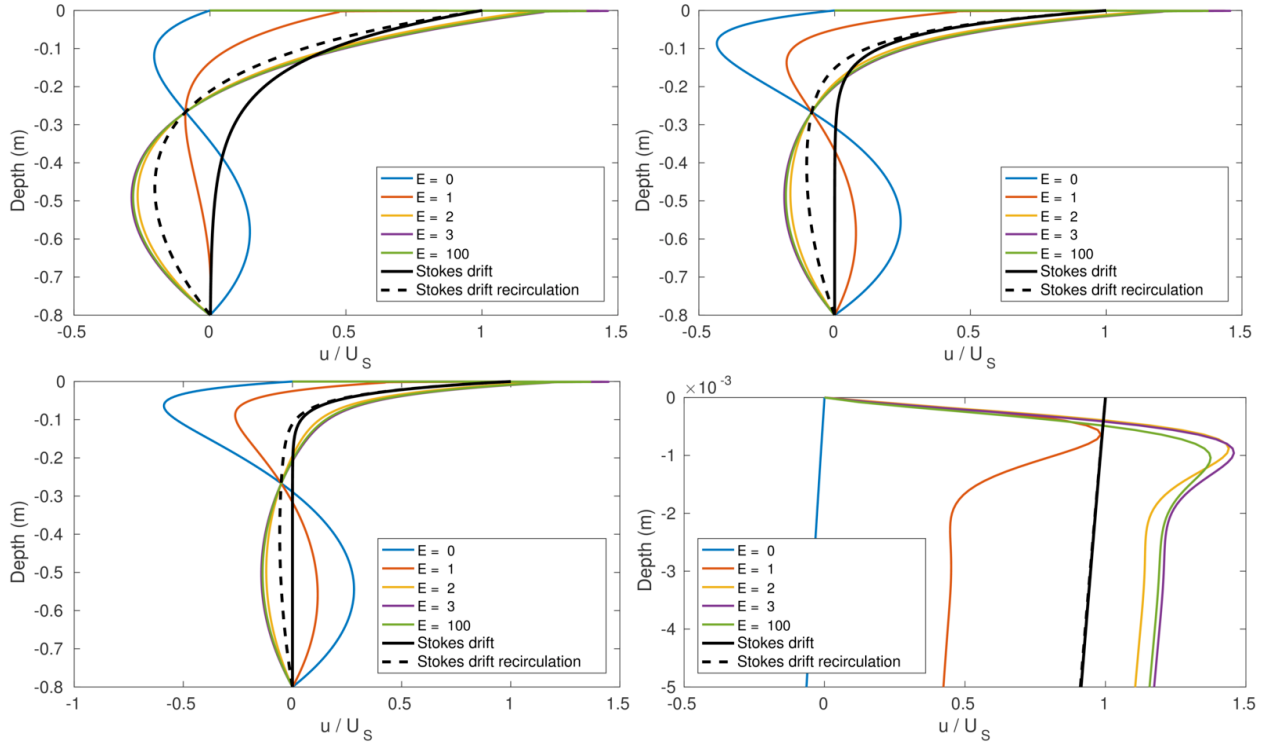


Fig. 1 Mean flow motion, normalized by the maximum Stokes drift at each frequency, for frequencies 1.00, 1.50 and 2.00 Hz (left to right, top to bottom) and different values of the elasticity parameter, as obtained from Eqn. (56) of [1]. Bottom right: zoom on the boundary layer obtained near the surface cover in the 1.50 Hz case. The Stokes drift and Stokes drift recirculation profiles are obtained from Eqn. (1) and Eqn. (2), respectively.

with Eqn. (56) of [1] are presented in Fig 1. In all the following, figures are presented using the convention that waves propagate from left to right. The latex cover used in our experiments is thick enough that it appears inextensible compared to the waves surface shear stress, therefore corresponding to a value of $E=\infty$. In practice, a value of $E=100$ is enough to get the right profile shape.

3. Experimental setup

The wave tank of the Hydrodynamics Laboratory at the University of Oslo is used to investigate the effect of a cover on water waves. The wave tank is 24.6 m long, 0.5 m wide and the water depth is 0.7 m [12]. The wave generator consists of a vertical plate driven by a computer controlled hydraulic piston. At the far end of the tank, an absorbing beach reduces the amplitude of reflected waves to less than 3 % of the incoming amplitude for frequencies higher than 1.5 Hz. The motion of the wave maker during the measurements is chosen to be sinusoidal with constant amplitude in order to generate harmonic waves, and a brief transient amplitude following a tanh law is used at the beginning of the run to establish the waves.

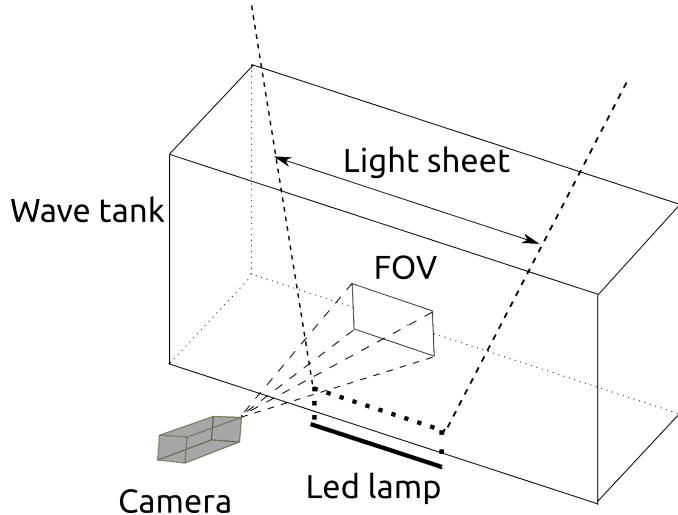


Fig. 2 PTV setup. FOV indicates the approximate position of the field of view.

The experimental setup used for acquiring the flow pictures is presented in Fig. 2. The measurements are performed in a vertical plane parallel to the axis of the wave tank. A LED array is used to illuminate the measurement plane from under. A Falcon 2 4M camera is used to take pictures of the flow, which is seeded with spherical Polyamid Seeding Particles of diameter 50 μm .

The pictures used for performing PTV are taken at 75 to 80 frames per second, and the number of pictures taken corresponds to a 30 seconds duration time interval. Each time a new experiment is to be performed, a first set of pictures is taken before the paddle has been started. This is done to measure the residual motion present in the wave tank before any waves have been produced. Following this, two sets of pictures are taken which start 30 and 210 seconds after the paddle start, respectively.

Residual motion present in the wave tank is a challenge when performing mean flow measurements. After each measurement, grids were introduced in the wave tank and left overnight to damp the recirculation motion generated by the waves. We waited at least 2 hours between seeding and the measurements, so that small scale motion generated by the seeding could be reduced. However, since the recirculation motion has a large spatial scale it is very little damped, and even taking those precautions recirculation motion of typical magnitude 1 to 2mm/s were found at the beginning of each measurement. As a consequence, the maximum Stokes drift magnitude must be at least one order of magnitude above this level in order to be able to observe meaningful mean flow profiles. This imposes us to perform experiments for relatively steep waves, at relatively low frequency. In practice we performed measurements at

1.50 Hz with a steepness $\varepsilon=0.19$, which corresponds to a maximum Stokes drift of 0.038m/s. Lower frequencies cannot be used since significant reflections would then take place at the damping beach. This means that we are out of the strict validity domain of the linear theories with which we compare our results.

4. Processing method and results

While Particle Image Velocimetry (PIV) is the method of choice for obtaining Eulerian velocity fields, PIV is not well adapted to obtaining Lagrangian quantities. Indeed, obtaining Lagrangian information from an Eulerian field requires numerical integration over time, which introduces noise. By contrast, PTV allows tracking the motion of a particle between several pictures and is therefore well suited to computing Lagrangian mean drift velocity profiles.

Digiflow is used to perform PTV on the images obtained, both before and after paddle start. An example of residual mean velocity profile, that was present before any waves were generated on that day, is shown in Fig. 3. Data is grouped in 20 bins covering the whole field of view depth range and the Chauvenet criterion [13] is used to discard outliers in each bin. The mean velocity profile is then computed, and will be subtracted to the measurements performed after the paddle is started.

The PTV tracks obtained when waves are present are processed to extract the mean drift velocity of each particle. The aim is to extract the mean drift velocity of the particles but to ignore their oscillatory orbital motion. For this, each particle track is reduced to the maximum integer number of periods during which the corresponding particle is followed. The difference between the initial and final positions of the reduced track is then used to compute the mean horizontal drift velocity of the particle. The value of the depth used for each particle corresponds to the mean depth over the whole track. Finally, the mean velocity profile obtained before the paddle was started is subtracted from the data to reduce the impact of recirculation effects on the profiles.

Results with and without cover are presented in Fig. 4. It is difficult to track any particles close to the water surface. The reason for this is that the corresponding area tends to get depleted of particles, and that the flow orbital motion gets too big in this area for the tracking algorithm to work properly. In the case without a cover (two top figures), the PTV data follows the modified Stokes drift Eqn. (2). Best agreement with this modified Stokes drift profile is found when the recirculation profile present before the paddle start is subtracted from the data. In the case with a

cover (two bottom figures), the PTV data agrees best with the solution derived in [1]. Similarly to the case without a cover, it is necessary to take away the initial recirculation profile to get good

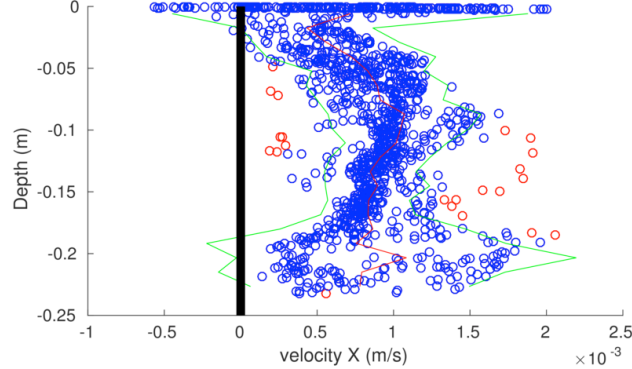


Fig. 3 Illustration of the use of the Chauvenet criterion on typical PTV data, before the paddle has been started. Coherent residual motion is clearly visible. Blue dots: drift of a valid PTV particle. Red dots: PTV particles discarded by the Chauvenet criterion. Red line: mean drift profile. Green lines: 2σ confidence intervals of the mean drift profile.

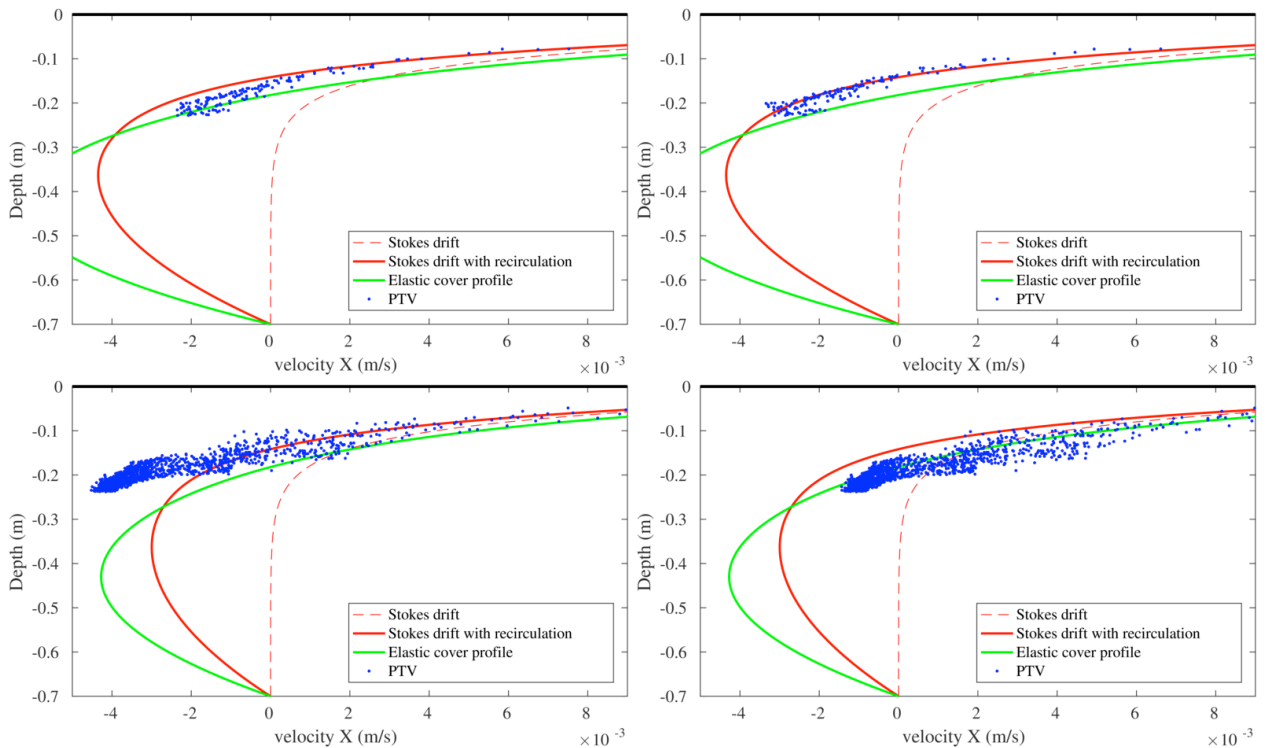


Fig. 4 Comparison of the PTV profiles obtained for waves of frequency 1.5 Hz and steepness $\epsilon = 0.19$ without (top) and with (bottom) thin latex cover. Left: PTV data without correction for the residual mean velocity profile present before the paddle is turned on. Right: PTV data taking into account correction for the residual mean velocity profile present before the paddle is turned on. The Stokes drift with recirculation corresponds to Eqn. (2). The elastic cover profile corresponds to the solution Eqn. (56) of [1], for an infinite elasticity parameter value.

agreement with the analytical model. The effect of the cover consists of increasing the mean drift velocity in the direction of wave propagation near the water surface. This can be seen as a

consequence of the diffusion of the vorticity created by the no slip boundary condition at the water surface.

5. Conclusion

Mean drift velocity profiles under water waves are investigated using Particle Tracking Velocimetry (PTV). Mean drift velocity profiles are sensitive to residual motions initially present in the wave tank. Unfortunately, it proves difficult to reduce the residual motion below typically a few mm/s, even using grids to damp flow motion and waiting 20 hours between two experiment runs. Possible sources of residual velocity are the large scale recirculation motion induced by previous wave experiments, and smaller scale motions coming from particle seeding. To minimize the magnitude of such flow recirculation compared to the effects we want to observe, steep waves at relatively low frequency are generated to obtain high values of the maximum Stokes drift.

We find poor agreement between experimental mean drift velocity profiles without cover and the theoretical Stokes drift for an infinitely long wave train on infinitely deep water, as it had been previously reported in the literature. While the scaling of the observed mean drift velocity is in good agreement with theory, we observe strong recirculation effects as soon as the wave front goes pass the measurement position. To take this effect into account we introduce an ad hoc modified Stokes drift profile, which is obtained by the addition of a parabolic velocity profile to the Stokes drift profile so that the integrated mean mass flow over the whole water column is zero. While we have no solid theoretical ground for introducing this modified profile, good agreement is found with our PTV data in the case without cover. This modified profile may be specific of the high steepness waves that are generated, and it would be interesting to perform PTV investigation along the whole water column depth to get an experimental measurement of the whole profile, i.e. not limited only to an area in the upper part of the water column.

In the presence of an inextensible cover on the water surface, slight modifications of the mean drift velocity profiles are observed which are in good agreement with corresponding theory. In particular the mean drift velocity is increased close to the surface cover, which can be explained by the diffusion of vorticity generated by the no slip boundary condition.

References

- [1] K.H. Christensen. Transient and steady drift currents in waves damped by surfactants. *Physics of Fluids*, 17(4), 2005.
- [2] S.H. Lamb. *Hydrodynamics*. Cambridge University Press, 1932.
- [3] V.A. Squire. Of ocean waves and sea-ice revisited. *Cold Regions Science and Technology*, 49(2):110 – 133, 2007.
- [4] L.A. Gushchin and S.A. Ermakov. Laboratory study of surfactant redistribution in the flow field induced by surface waves. *Izvestiia-Russian Academy Of Sciences Atmospheric And Oceanic Physics C/C Of Izvestiia-Rossiiskaia Akademii Nauk Fizika Atmosfery I Okeana*, 40(2):244–249, 2004.
- [5] A.W.K. Law. Wave-induced surface drift of an inextensible thin film. *Ocean engineering*, 26(11):1145–1168, 1999.
- [6] K.H. Christensen and G. Broström. Waves in sea ice. Technical report, Norwegian Meteorological Institute, 2008.
- [7] S.L. Pfirman, H. Eicken, D. Bauch, and W.F. Weeks. The potential transport of pollutants by arctic sea ice. *Science of The Total Environment*, 159(2–3):129 – 146, 1995.
- [8] J. Turner, T.J. Bracegirdle, T. Phillips, G.J. Marshall, and J. Scott Hosking. An initial assessment of antarctic sea ice extent in the cmip5 models. *Journal of Climate*, 26:1473–1484, 2013.
- [9] S.G. Monismith, E.A. Cowen, H.M. Nepf, J. Magnaudet, and L. Thais. Laboratory observations of mean flows under surface gravity waves. *Journal of Fluid Mechanics*, 573:131–147, 2 2007.
- [10] G.G. Stokes. On the theory of oscillatory waves. In *Mathematical and Physical Papers vol.1, volume 1*, pages 197–229. Cambridge University Press, 2009. Cambridge Books Online.
- [11] A.D.D. Craik. George Gabriel stokes on water wave theory. *Annual Review of Fluid Mechanics*, 37(1):23–42, 2005.
- [12] A. Jensen, G.K. Pedersen, and D.J. Wood. An experimental study of wave run-up at a steep beach. *Journal of Fluid Mechanics*, 486:161–188, 6 2003.
- [13] J.R. Taylor. *An introduction to error analysis*. University Science Books, 1982.

2.6 Publication 6: The attenuation of monochromatic surface waves due to the presence of an inextensible cover

Sutherland, G., Halsne, T., Rabault, J., and Jensen, A. (2017), "The attenuation of monochromatic surface waves due to the presence of an inextensible cover", *Wave Motion*, 68:88 – 96.



The attenuation of monochromatic surface waves due to the presence of an inextensible cover



Graig Sutherland*, Trygve Halsne, Jean Rabault, Atle Jensen

Department of Mathematics, University of Oslo, Postboks 1053 Blindern, 0316, Oslo, Norway

HIGHLIGHTS

- Direct observations of wave attenuation under an inextensible surface cover.
- Observations consistent with viscous attenuation for frequencies 1 to 2 Hz.
- Attenuation is due to no-slip boundary condition and independent of cover type.

ARTICLE INFO

Article history:

Received 9 May 2016

Received in revised form 4 August 2016

Accepted 4 September 2016

Available online 21 September 2016

Keywords:

Surface gravity waves

Wave attenuation

Surface covers

Viscosity

ABSTRACT

The attenuation of surface gravity waves is an important process associated with air-sea and wave-current interactions. Here we investigate experimentally the attenuation of monochromatic surface gravity waves due to the presence of various surface covers. The surface covers are fixed in space such that they do not advect with the wave motion and are selected such that the bending modulus is negligible for the wave frequencies used in the experiment in order to minimize any flexural effects. Wave attenuation rates are found to be independent of wave steepness and the type of cover used over the tested parameter range. Results are consistent with the theoretical attenuation rate for an inextensible surface cover.

© 2016 Elsevier B.V. All rights reserved.

1. Introduction

Knowledge of the effect of modifying the water surface on attenuating surface waves goes back to antiquity [1]. This changing of the surface rheology can arise from the presence of oil [2], ice [3], or from certain atmospheric and meteorological conditions [4]. Wave attenuation is frequency dependent [5,6], which generally increases with increasing frequency, although this can depend on the nature of the surface cover [2,7]. Wave attenuation is an important component of many physical processes such as those associated with air-sea interactions [8], wave-current interactions [9], surface drift [10], and stabilizing wave modulation [11] to name a few.

In the absence of a surface film, wave attenuation is primarily due to the straining motion of the irrotational component of the wave motion (see [5,6]) and theoretical values have been verified in laboratory experiments in cases where the surface was meticulously cleaned, see [12,13]. In the presence of a surface film, a viscous boundary layer develops which acts to increase the attenuation of surface waves (see [5,6]). If this surface film is elastic then the wave attenuation becomes much more complicated as some of the wave energy can also go into longitudinal waves, also known as Marangoni or dilatational waves [2,14].

* Corresponding author.

E-mail address: graigors@math.uio.no (G. Sutherland).

The inextensible model of [5] has been applied to wave attenuation in ice and requires viscosity values several orders of magnitude greater than the molecular value to match observed attenuation rates [3,15–17]. In ice there are many processes which also attenuate energy such as scattering from ice floes [18] and ice creep [19], which might contribute. These observations are limited to oceanic conditions and often the argument is made that the boundary layer is turbulent, predominantly due to the ridges and keels present under the ice, and hence the larger eddy viscosity is justified on these grounds (see [3]).

While laboratory experiments of wave attenuation involving clean water (see [12] and references therein) and water in the presence of surfactants (see [2]) have been performed, there has been little attention paid to investigating inextensible surface covers. More recently, it has been shown by [13] that observations of the attenuation of ocean swell by [20,21] are consistent with the theoretical attenuation rate of an inextensible surface cover. However, the physics as to why swell attenuation is best modelled by an inextensible surface cover is not clear.

The main objective of this study is to investigate the attenuation of monochromatic surface waves due to the presence of an inextensible surface cover. The paper is outlined as follows: a brief review of the theoretical background for wave attenuation is described in Section 2. A description of the experimental setup is presented in Section 3. Section 4 presents the results of the experiment followed by a summary and discussion in Section 5.

2. Theoretical background

2.1. Linear wave attenuation

Wave amplitudes have been observed to attenuate exponentially, i.e.

$$\frac{\partial a}{\partial x} = -\alpha a \quad (1)$$

where a is the wave amplitude, x is the distance along the wave flume, and α is the total wave attenuation. Linear wave attenuation arises from viscous dissipation within the fluid [5,6] as well as boundary effects from the bottom and sidewalls of a wave flume [22], viscous effects from the air above the interface [23] and the presence of surfactants on the water surface [10,12,13].

In the absence of a boundary layer, whether it be at the surface or due to the finite dimensions of a wave flume, the temporal wave attenuation rate, as given by [5], is

$$\frac{\partial a}{\partial t} = -2\nu k^2 a, \quad (2)$$

where t is time, ν is the kinematic viscosity, and k is the wave number. It is often difficult to clean the surface sufficiently such that there are no particles or natural surfactants present, and thus the clean water attenuation rates are difficult to obtain in wave flumes, see [13].

In the presence of a surface film, the wave attenuation is greater than (2) as the film acts to enhance vorticity in the boundary layer created by the film. In the inextensible limit the boundary condition is assumed to be no-slip and the wave attenuation, as given by [5], is

$$\frac{\partial a}{\partial t} = -\frac{1}{2}\nu\gamma ka, \quad (3)$$

where $\gamma = \sqrt{\omega/2\nu}$ is the inverse boundary layer thickness [5].

The temporal attenuation rate in (2) and (3) can be related to the spatial attenuation rate by using the relation of Gaster [24], i.e.

$$\frac{\beta}{\alpha} = c_g \quad (4)$$

where β is the temporal attenuation rate, as shown in (2) and (3), α is the spatial attenuation rate, and $c_g = \partial\omega/\partial k$ is the group velocity. Using (4) with (2) and (3) gives the spatial attenuation rates for clean water,

$$\alpha_{cl} = 2\nu k^2/c_g, \quad (5)$$

and

$$\alpha_{in} = \frac{1}{2}\nu\gamma k/c_g \quad (6)$$

for the inextensible surface cover.

In general, the ratio (k/γ) , which is the ratio of the boundary layer thickness to the wavelength, is small with $k/\gamma = 2 \times 10^{-3}$ for a 1 Hz deep water wave and $k/\gamma = 2 \times 10^{-2}$ for a 5 Hz deep water wave. It can easily be shown that $\alpha_{cl}/k = \mathcal{O}(k/\gamma)^2$ while $\alpha_{in}/k = \mathcal{O}(k/\gamma)$, and since $k/\gamma \ll 1$, is consistent with $\alpha_{cl} \ll \alpha_{in}$.

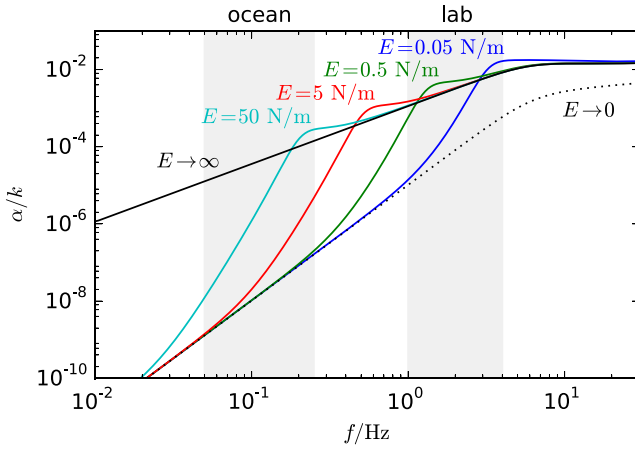


Fig. 1. Attenuation rate normalized by the wave number k as a function of frequency. The grey shaded region on the left shows a typical spectral range for ocean waves of 0.05–0.25 Hz and the region on the right shows a typical range for laboratory waves of 1–4 Hz. The inextensible ($E \rightarrow \infty$) and clean ($E \rightarrow 0$) limits are shown along with the attenuation rate for different film elasticity.

For insoluble surface covers of finite elasticity and negligible thickness (e.g. a monomolecular surface film) the attenuation rate is given by [10],

$$\alpha_e = \Gamma \alpha_{in} \quad (7)$$

where Γ is defined as

$$\Gamma = \left[\frac{2\epsilon^2}{F} + \frac{k}{\gamma} \frac{4(1-\epsilon)}{F} \right] \quad (8)$$

and ϵ is the non-dimensional elasticity

$$\epsilon = \frac{Ek^2\gamma}{\rho\omega^2}, \quad (9)$$

E is the film elasticity, ρ is the fluid density and $F = 1 - 2\epsilon + 2\epsilon^2$. The theoretical attenuation rate for an elastic surface cover is shown in Fig. 1. The inextensible limit, i.e. as $E \rightarrow \infty$ and $\alpha_e \rightarrow \alpha_{in}$, and the clean water limit, i.e. $E \rightarrow 0$ and $\alpha_e \rightarrow \alpha_{cl}$, are shown. The elastic attenuation rate has a peak value of twice the inextensible limit when $\epsilon = 1$. The frequency at which the maximum attenuation occurs is due to a “resonant” type interaction where the dispersion curves of the transverse surface waves and the longitudinal waves intersect [2]. This increased attenuation is attributed to a more efficient energy transfer from the transverse waves to the longitudinal waves. Setting $\epsilon = 1$ in (9) gives the peak attenuation frequency to be

$$\omega_{res} = \left(\frac{2\nu\rho^2g^4}{E^2} \right)^{\frac{1}{5}}. \quad (10)$$

The resonance frequency derived by [2, their equation 6] differs by a factor of $\rho^{1/5}$ from (10), which can be reasoned from dimensional grounds to be a typo in their manuscript.

The difference in deriving (5)–(7) lies in the boundary conditions for the tangential stress τ . Assuming a Hookean tangential stress [10], the stress is written as

$$\tau = E\Delta x, \quad (11)$$

where Δx is the surface strain. In the absence of surface contamination $E = 0$ and $\tau = 0$. In the inextensible limit $E \rightarrow \infty$, which implies $\Delta x \rightarrow 0$ in order for τ to be finite. This limit implies that the no-slip condition applies. However, as shown by [25], this is only true in a linear sense and does not apply if nonlinear terms are included.

An additional attenuation process is expected due to the viscous drag of the air above waves. The attenuation of the two fluid system, i.e. air and water, was shown by [23] to be

$$\alpha_{2fl} = \alpha_{cl} + \sqrt{2} \frac{\rho_a}{\rho} \left(v_{ak}^2 \right)^{1/2} (gk)^{1/4} / c_g \quad (12)$$

where ρ_a and v_a are the density and kinematic viscosity of the air. The dynamic boundary condition for the two fluid system is continuity in both the tangential and normal stresses at the interface. As shown earlier for deepwater gravity waves, $\alpha_{cl}/k = \mathcal{O}(k/\gamma)^2$, while the second term in (12) associated with the air drag can be shown to be $\alpha_{air}/k \propto (\rho_a/\rho)\sqrt{v_a/v(k/\gamma)}$ where α_{air} represents the second term in (12). So while the attenuation due to the air viscosity is $\mathcal{O}(k/\gamma)$, identical to

Table 1

Experimental parameters. Thin refers to the thin latex, thick is the thick latex, and poly is the polypropylene cover.

Cover	f/Hz	λ/m	$a_0 k$	$\alpha/k \times 10^{-3}$
Thin	1.00	1.55	0.04	2.11 ± 1.04
	1.50	0.70	0.07	3.41 ± 0.26
	1.75	0.51	0.09	3.12 ± 1.36
	2.20	0.32	0.10	5.48 ± 0.54
	2.40	0.27	0.12	6.36 ± 0.68
Thick	1.00	1.55	0.04	2.52 ± 0.82
	2.00	0.39	0.09	5.61 ± 1.20
	2.20	0.32	0.14	6.45 ± 1.64
	2.40	0.27	0.11	9.31 ± 5.44
Poly	1.50	0.70	0.07	3.16 ± 0.24
	2.00	0.39	0.09	4.81 ± 0.14
	2.20	0.32	0.09	5.61 ± 1.20
	2.40	0.27	0.12	8.24 ± 1.82

boundary layer attenuation, $\rho_a \ll \rho$ by three orders of magnitude and will severely limit the effectiveness of the air viscosity to attenuate the waves. Since k/γ is also between 10^{-3} and 10^{-2} the air-side dissipation is expected to be of the same order of magnitude as the water-side.

For laboratory experiments, the finite dimensions of the wave flume will contribute additional wave attenuation [22] with an attenuation rate of

$$\alpha_{sb} = \nu\gamma k \left(\frac{1}{\sinh 2kH} + \frac{1}{kB} \right) / c_g, \quad (13)$$

where H is the water depth and B is the width of the wave flume. This attenuation is due to the boundary layer dissipation and is $\mathcal{O}(k/\gamma)$ and can be assumed to be negligible for large kH for bottom dissipation and for large kB for sidewall attenuation.

2.2. Linear dispersion relation

The dispersion relation for the surface transverse wave under a cover of finite thickness h is

$$\omega^2 = gk \tanh kH \left(1 + \frac{T}{\rho g} k^2 + \frac{D}{\rho g} k^4 \right) \quad (14)$$

where H is the water depth ($H \rightarrow \infty$ in Fig. 1), T is the surface tension, and D is the bending modulus defined as $D \equiv Yh^3/12(1 - \mu^2)$ where Y is the Young's modulus and μ is the Poisson ratio. The surface tension term is negligible when $Tk^2/(\rho g) \ll 1$, which occurs for wavelengths $\lambda \gg 2\pi\sqrt{T/(\rho g)} = 2 \text{ cm}$. The bending term can be omitted for wavelengths $\lambda \gg 2\pi\sqrt[4]{D/(\rho g)}$, which for our maximum bending modulus $D \approx 2 \times 10^{-5} \text{ N/m}$ (associated with the thick latex cover with $Y = 1.5 \text{ MPa}$, $\mu = 0.5$ and $h = 0.5 \text{ mm}$) gives $\lambda \gg 4 \text{ cm}$. In addition, changes to the dispersion relation (14) due to the attenuation associated with the surface boundary layer are of order (k/γ) and are negligible for the frequencies used in this experiment [10].

3. Experimental setup

Experiments were conducted in the 24.6 m long and 0.5 m wide wave flume located in the Hydrodynamics Laboratory at the University of Oslo. The wave flume was filled with freshwater to a depth of 0.6 m. Waves were generated with a hydraulic-driven piston. An absorbing beach is located at the opposite end of the wave flume to the wave generator in order to minimize the reflection of wave energy. The reflection coefficient of the absorbing beach was calculated using the WaveAr software [26] to be less than 4%.

Three different surface covers were used in the experiments: a woven polypropylene cover with thickness of 0.3 mm, and two latex covers of thickness 0.25 and 0.5 mm. The latex covers were similar to the ones used by [27], while the woven polypropylene cover is typical to that used in gardens as a weed barrier. Each cover has a width of 0.5 m, which spanned the width of the wave flume, with a length of 17 m for the polypropylene and 15 m for the two latex covers. Each surface cover was fixed to the wave flume at 6.4 m from the wave paddle. The cover was fastened to a horizontal bar placed along the width of the flume and 10 cm above the still water line to prevent over wash of the waves as they encountered the cover. The covers were not fixed at the sidewalls of the wave flume.

For the wave damping experiments, monochromatic waves were used at frequencies between 1.5 and 2.4 Hz and a wave steepness ak between 0.05 and 0.15. Table 1 shows the experimental parameters used in this study. Wave elevation along the flume was measured using an array of ULS Advanced ultrasonic wave gauges manufactured by Ultralab. Each wave gauge has a resolution of 0.18 mm and sampled the surface elevation at 250 Hz. The array consisted of 3 wave gauges equally spaced

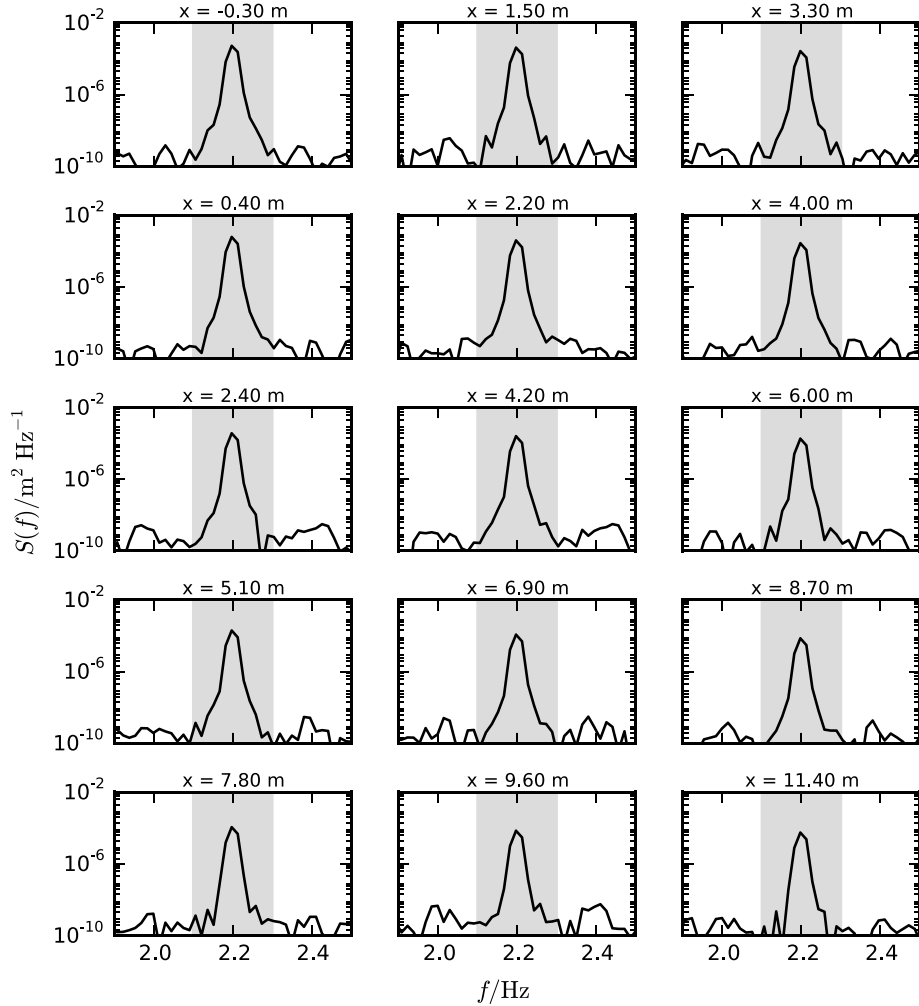


Fig. 2. Wave spectra calculated at 15 different locations for the 2.2 Hz wave with a steepness of $a_0 k = 0.10$ propagating under the thin latex cover. The grey shaded region denotes the spectral bandwidth used to obtain the amplitude.

1.8 m apart from each other. The array was traversed along the length of the wave flume at discrete time intervals to increase spatial coverage. Since the cover is fixed to the wave flume, there is no advection of the surface cover and the wave field can be assumed to be steady state after some initial set-up time, which we take a cautious value of 5 min. After the wave field has clearly achieved a steady state, the wave array is shifted every 3 min by 0.7, 2.7, 5.4, and 8.1 m relative to the leading edge of the surface cover. The first wave gauge is located at 0.3 m upstream of the cover, thus elevation measurements are obtained at $-0.3, 0.4, 1.5, 2.2, 2.4, 3.3, 4.0, 4.2, 5.1, 6.0, 6.9, 7.8, 8.7, 9.6$, and 11.4 m relative to the leading edge of the surface cover. To avoid the possible contamination of reflected waves at the leading edge of the cover only measurements downstream of this edge are used.

4. Results

The wave elevation along the wave flume is calculated using

$$a(x) = \sqrt{\int_{f_0-\Delta f}^{f_0+\Delta f} S(f) df} \quad (15)$$

where $S(f)$ is the wave spectrum, f_0 is the forcing frequency and Δf the bandwidth of the wave spectrum and is chosen to be $\Delta f = 0.1$ Hz. Our results are not sensitive to the choice of Δf as long as $\Delta f \ll f_0$ so not to include bounded waves. Wave spectra for various locations along the tank can be seen in Fig. 2 for the 2.2 Hz wave propagating under the thin latex cover. The peak of each wave spectrum is seven orders of magnitude greater than the noise floor outside the spectral bandwidth (shown by the shaded grey region).

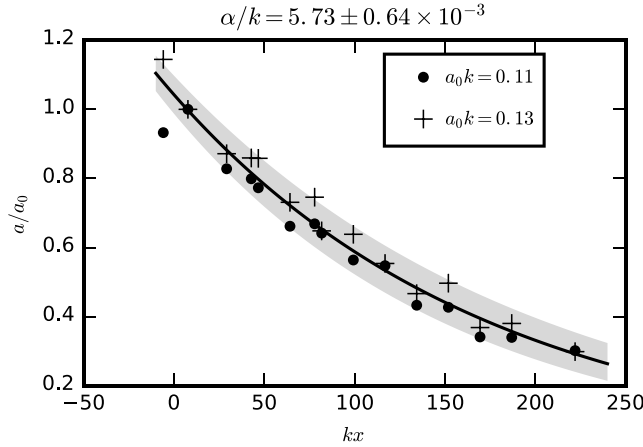


Fig. 3. Wave attenuation with the thin latex cover for a 2.20 Hz wave for two different wave steepness. The attenuation rate does not vary for the two different wave steepness. The grey shaded region shows two standard deviations of the least-squares fit.

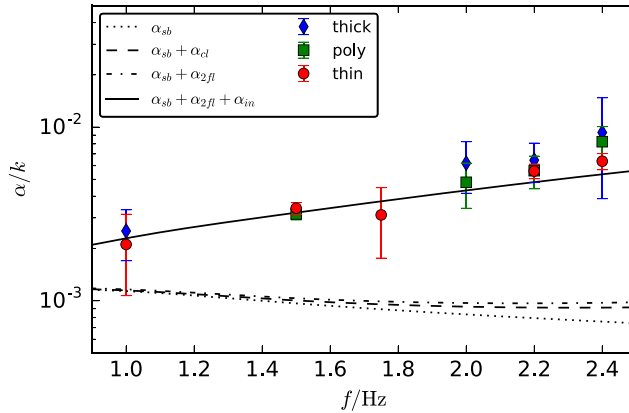


Fig. 4. Wave attenuation rate normalized by the wavenumber k as a function of frequency for each surface cover (thick = 0.5 mm latex, poly = 0.3 mm polypropylene, thin = 0.25 mm latex). The error bars show two standard deviations of the least-squares fit to the attenuation curve.

The wave amplitude, as a function of distance along the wave flume, is shown in Fig. 3 to attenuate exponentially. The wave amplitude is normalized by the amplitude measured before the surface cover, i.e. $a_0 = a(x = 0.4 \text{ m})$, and the distance is normalized by k calculated by (14). The wave attenuation rate is calculated using a least-squares fit of all the observed values and the error bars show two standard deviations of the best fit parameters. The exponential model for wave attenuation fits the observed values very well and is independent of the wave amplitude for the range of wave steepness used in the experiment.

The observed attenuation rates for all the frequencies and surface covers are shown in Fig. 4. These attenuation rates are compared with the theoretical attenuation rates for the clean and inextensible limits along with that for the sidewalls and bottom. For the theoretical attenuation rates, the kinematic viscosity is assumed to be $\nu = 1.1 \times 10^{-6} \text{ m}^2 \text{ s}^{-1}$ and the density is $\rho = 1.0 \times 10^3 \text{ kg m}^{-3}$. Results are generally consistent with the inextensible limit of Lamb [5]. The error relative to the inextensible limit for each frequency and surface cover is shown in Fig. 5.

5. Summary and discussion

Presented is a series of laboratory experiments using fixed surface covers to validate wave attenuation due to an inextensible cover. The surface cover had to be sufficiently flexible to follow the surface of the propagating waves. Latex, of which two different thicknesses were tested, as well as polypropylene was chosen as they both possessed the surface following condition yet have different elastic properties. For the frequencies used in this experiment, the choice of the surface cover had little effect on the attenuation rate. The stiffer covers, such as the thick latex and the polypropylene, had larger errors associated with the exponential fits, which is presumed to arise from these covers not following the surface as accurately as the thin latex.

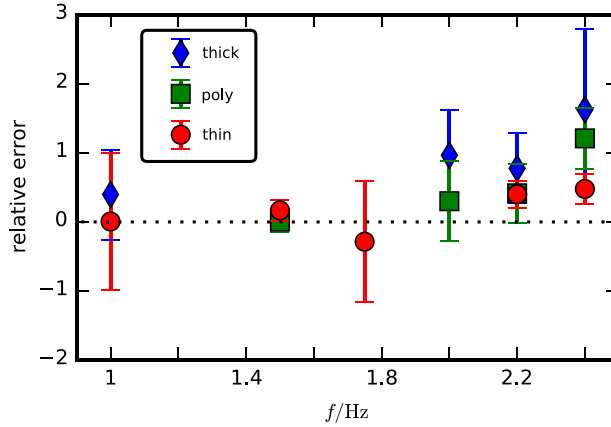


Fig. 5. Relative error of the observed attenuation rate with the theoretical value ($\alpha_{sb} + \alpha_{2fl} + \alpha_{in}$) as a function of frequency for the various surface covers. The error bars show two standard deviations of the least-squares fit to the attenuation curve.

For frequencies less than 2 Hz, observations of the attenuation rate were consistent with the inextensible limit of Lamb [5], within two standard deviations of the best fit parameters. However, for frequencies greater than 2 Hz, the attenuation rates exceed the inextensible limit by 20% to 90%. While the presence of longitudinal waves, due to the elasticity of the surface cover, can lead to a peak attenuation rate of twice the inextensible limit, which can be seen in Fig. 1, this seems unlikely as the different cover materials yield similar results. Henderson et al. [13] also observed wave attenuation rates of roughly twice the inextensible value of (3) using sheets of cling wrap for the surface cover, which they hypothesized were due to the presence of longitudinal waves. However, this maximum attenuation rate exists for a relatively narrow bandwidth (see [2]) and it is unclear whether this should be applied over the frequency range of 1–4 Hz used in their experiments [13].

The effect of the added mass of the surface cover on the wave attenuation is expected to be negligible as the relative density of polypropylene and latex to freshwater is 0.92 and 0.96 respectively. The cover will also affect the dispersion relation, but the deviation from (14) will be on the order of k/γ [10], which for our frequency range has a maximum value of 8×10^{-3} and can safely be ignored.

The elasticity of the surface cover has been ignored in our calculations, but there will exist a certain frequency range where it might be important. In order to estimate the film elasticity we need to linearize the bulk modulus of the sheet. Since the bulk modulus is defined as

$$Y = \frac{\tau/A}{\Delta x/x_0} \quad (16)$$

where A is the cross-sectional area, Δx is the extension and x_0 is the length, and we want something of the form (11), it is trivial to show that

$$E = \frac{AY}{x_0}. \quad (17)$$

Taking the Young modulus for the thin latex sheet to be $Y = 1.0 \times 10^6 \text{ N/m}^2$, and the dimensions of the sheet to be $b = 0.5 \text{ m}$, $l = 15 \text{ m}$ and $h = 0.25 \times 10^{-3} \text{ m}$ for the width, length, and thickness respectively, we can estimate E from (17) to be about 8 N/m .

Elastic effects on wave attenuation are tested by a least-squares fit of the observed attenuation rate to (7) and allowing E and ν to be free parameters. The best fit for each cover is shown in Fig. 6. In all cases, the best-fit value for E is greater than 100 N/m , which has a negligible difference on the attenuation curves over the frequency range used in this experiment. Fig. 7(a) shows ε as a function of f for different values of E and Fig. 7(b) shows the multiplier Γ in (7) as a function of ε . For frequencies used in the lab, $E > 5 \text{ N/m}$ leads to values of $\varepsilon > 10$ (Fig. 7(a)), which is in the inextensible limit (Fig. 7(b)). The best-fit values for ν are larger than the expected value of $\nu = 1.1 \times 10^{-6} \text{ m}^2 \text{ s}^{-1}$, but within two standard deviations (95% confidence) with the exception of the polypropylene cover which is three standard deviations larger.

Acknowledgements

Funding for the experiment was provided by the Norwegian Research Council under the PETROMAKS2 scheme [Grant Number 233901]. We thank Kai Christensen for the encouragement and many stimulating discussions with regard to the experiments.

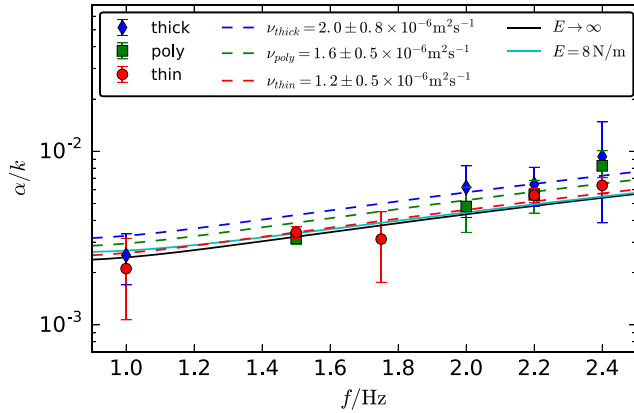


Fig. 6. Wave attenuation rate normalized by the wavenumber k as a function of frequency for each surface cover (thick = 0.5 mm latex, poly = 0.3 mm polypropylene, thin = 0.25 mm latex). The black line shows the theoretical value for $\nu = 1.1 \times 10^{-6} \text{ m}^2 \text{ s}^{-1}$. The film elasticity and viscosity are used as free parameters and fit to the observed attenuation rates. The error bars show two standard deviations of each individual attenuation rate.

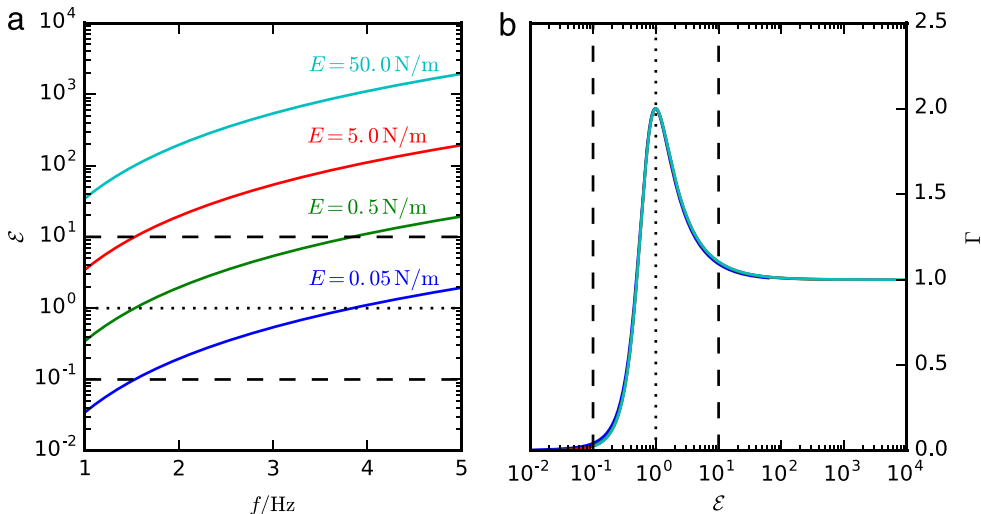


Fig. 7. (a) Non-dimensional elasticity ϵ as a function of frequency for different values for the film elasticity. Attenuation rates are twice the inextensible limit when $\epsilon = 1$, which is shown by the black dotted line. (b) The attenuation multiplication factor Γ for finite film elasticities as a function of ϵ showing the transition from the clean surface to an inextensible surface film. The black dotted line shows $\epsilon = 1$ and the dashed line shows $\epsilon = 10^{-1}$ and $\epsilon = 10$, which corresponds to the clean and inextensible limits respectively.

References

- [1] J. Scott, The historical development of theories of wave-calming using oil, *Hist. Technol.* 3 (1978) 163–186.
- [2] W. Alpers, H. Hühnerfuss, The damping of ocean waves by surface films: A new look at an old problem, *J. Geophys. Res.: Oceans* 94 (C5) (1989) 6251–6265.
- [3] J.E. Weber, Wave attenuation and wave drift in the marginal ice zone, *J. Phys. Oceanogr.* 17 (12) (1987) 2351–2361.
- [4] H. Hühnerfuss, W. Walter, G. Kruspe, On the variability of surface tension with mean wind speed, *J. Phys. Oceanogr.* 7 (4) (1977) 567–571.
- [5] H. Lamb, *Hydrodynamics*, sixth ed., Cambridge University Press, 1932.
- [6] O.M. Phillips, *The Dynamics of the Upper Ocean*, Cambridge University Press, 1977, p. 336.
- [7] J. Lucassen, Effect of surface-active material on the damping of gravity waves: A reappraisal, *J. Colloid Interface Sci.* 85 (1) (1982) 52–58.
- [8] B. Jähne, H. Haußecker, Air-water gas exchange, *Annu. Rev. Fluid Mech.* 30 (1) (1998) 443–468.
- [9] M.S. Longuet-Higgins, R. Stewart, Radiation stress and mass transport in gravity waves, with application to surf beats, *J. Fluid Mech.* 13 (04) (1962) 481–504.
- [10] K.H. Christensen, Transient and steady drift currents in waves damped by surfactants, *Phys. Fluids* 17 (4) (2005) 042102.
- [11] H. Segur, D. Henderson, J. Carter, J. Hammack, C.-M. Li, D. Pheiff, K. Socha, Stabilizing the Benjamin–Feir instability, *J. Fluid Mech.* 539 (2005) 229–271.
- [12] J.W. Miles, Surface-wave damping in closed basins, in: *Proceedings of the Royal Society of London A: Mathematical, Physical and Engineering Sciences*, Vol. 297, The Royal Society, 1967, pp. 459–475.
- [13] D. Henderson, G.K. Rajan, H. Segur, Dissipation of narrow-banded surface water waves, in: *Hamiltonian Partial Differential Equations and Applications*, Springer, 2015, pp. 163–183.
- [14] R. Dorrestein, General linearized theory of the effect of surface films on water ripples, *Nederl. Akad. Wetensch. B* 54 (1951) 250–272.
- [15] A.K. Liu, E. Mollo-Christensen, Wave propagation in a solid ice pack, *J. Phys. Oceanogr.* 18 (11) (1988) 1702–1712.
- [16] P. Wadhams, V.A. Squire, D.J. Goodman, A.M. Cowan, S.C. Moore, The attenuation rates of ocean waves in the marginal ice zone, *J. Geophys. Res.: Oceans* 93 (C6) (1988) 6799–6818.
- [17] F. Arduini, P. Sutherland, M. Doble, P. Wadhams, Ocean waves across the arctic: attenuation due to dissipation dominates over scattering for periods longer than 19 s, *Geophys. Res. Lett.* 43 (2016). <http://dx.doi.org/10.1002/2016GL068204>.

- [18] A.L. Kohout, M.H. Meylan, An elastic plate model for wave attenuation and ice floe breaking in the marginal ice zone, *J. Geophys. Res.* 113 (2008). <http://dx.doi.org/10.1029/2007JC004434>.
- [19] P. Wadhams, Attenuation of swell by sea ice, *J. Geophys. Res.* 78 (18) (1973) 3552–3563.
- [20] F.E. Snodgrass, G.W. Groves, K. Hasselmann, G. Miller, W. Munk, W. Powers, Propagation of ocean swell across the pacific, *Proc. R. Soc. Lond. Ser. A Math. Phys. Eng. Sci.* 259 (1103) (1966) 431–497.
- [21] F. Collard, F. Ardhuin, B. Chapron, Monitoring and analysis of ocean swell fields from space: New methods for routine observations, *J. Geophys. Res. Oceans* 114 (C7) (2009).
- [22] W. Van Dorn, Boundary dissipation of oscillatory waves, *J. Fluid Mech.* 24 (04) (1966) 769–779.
- [23] B. Dore, Some effects of the air-water interface on gravity waves, *Geophys. Astrophys. Fluid Dyn.* 10 (1) (1978) 215–230.
- [24] M. Gaster, A note on the relation between temporally-increasing and spatially-increasing disturbances in hydrodynamic stability, *J. Fluid Mech.* 14 (1962) 222–224.
- [25] D.M. Henderson, H. Segur, The role of dissipation in the evolution of ocean swell, *J. Geophys. Res.: Oceans* 118 (10) (2013) 5074–5091.
- [26] B.J. Landry, M.J. Hancock, C.C. Mei, M.H. García, WaveAR: A software tool for calculating parameters for water waves with incident and reflected components, *Comput. Geosci.* 46 (2012) 38–43.
- [27] L. Deike, J.-C. Bacri, E. Falcon, Nonlinear waves on the surface of a fluid covered by an elastic sheet, *J. Fluid Mech.* 733 (2013) 394–413.

2.7 Work 7: Experiments on wave propagation in grease ice: combined wave gauges and PIV measurements

Rabault, J., Sutherland, G., Jensen, A., Christensen, K. H., and Marchenko, A. (2018), "Experiments on wave propagation in grease ice: combined wave gauges and PIV measurements", *under review*